

## Copyright Undertaking

This thesis is protected by copyright, with all rights reserved.

**By reading and using the thesis, the reader understands and agrees to the following terms:**

1. The reader will abide by the rules and legal ordinances governing copyright regarding the use of the thesis.
2. The reader will use the thesis for the purpose of research or private study only and not for distribution or further reproduction or any other purpose.
3. The reader agrees to indemnify and hold the University harmless from and against any loss, damage, cost, liability or expenses arising from copyright infringement or unauthorized usage.

### IMPORTANT

If you have reasons to believe that any materials in this thesis are deemed not suitable to be distributed in this form, or a copyright owner having difficulty with the material being included in our database, please contact [lbsys@polyu.edu.hk](mailto:lbsys@polyu.edu.hk) providing details. The Library will look into your claim and consider taking remedial action upon receipt of the written requests.

**DESIGN AND FABRICATION OF LOW-LOSS  
PLASMONIC AND UPCONVERSION LASERS**

**SIU CHUN KIT**

**PhD**

**The Hong Kong Polytechnic University**

**2019**

**The Hong Kong Polytechnic University**

**Department of Applied Physics**

**Design and Fabrication of Low-loss Plasmonic and  
Upconversion Lasers**

**SIU Chun Kit**

A thesis submitted in partial fulfillment of the requirements  
for the degree of Doctor of Philosophy

**August 2018**



# Certificate of Originality

I hereby declare that this thesis is my own work and that, to the best of my knowledge and belief, it reproduces no material previously published or written, nor material that has been accepted for the award of any other degree or diploma, except where due acknowledgment has been made in the text.

\_\_\_\_\_

(Signature)

\_\_\_\_\_ SIU Chun Kit

(Name of candidate)



# Abstract

Theoretical analysis of plasmonic lasers is performed based on typical optical waveguide theory and laser physics. The study begins with the analysis of 1-dimensional planar waveguides, which has a highly symmetric structure with relatively simple mathematical derivation process from Maxwell equations. A two-layer planar waveguide is used to demonstrate the behavior of surface plasmon polariton propagating in a single metal-dielectric interface, in which light is confined within the sub-wavelength range along the transverse direction. Hence, this shows the significance of incorporating metal in laser designs to confine light within a small region. In addition, a three-layer planar waveguide (with two metal-dielectric interfaces) shows the interaction of surface plasmon between multiple adjacent metal-dielectric interfaces, resulting in a totally different behavior when compared to the two-layer system. It is noted that the degree of interaction highly depends on the distance between the two interfaces. Reflection Pole Method (RPM) is also used to analyze the optical behaviour of multi-layer planar waveguide structures. RPM is applied to study the longitudinal guided modes of common planar laser designs in recent researches. In particular, it is confirmed that by adding a thin dielectric protection layer between the gain medium and the metallic layer, the lasing threshold of Fabry-Pérot modes in nano-cavities can be effectively reduced due to the suppression of metallic absorption. Similar analysis also applies to the study of the whispering-gallery modes (WGMs) of radially-layered cylindrical waveguides.

The experimental part of this study involves the discussion of techniques in cavity excitation and spectral analysis, followed by design and fabrication of



upconversion lasers with micro- and nano-scale features. There are two major works discussed in this area. First, single-crystalline microplates of the semiconductive perovskite  $\text{CsPbCl}_3$  are fabricated. The microplate laser cavities, which have square shape of side lengths ranging from 2 to 10  $\mu\text{m}$ , support single- or multi-mode WGM lasing emission with quality factor  $Q \sim 1400$  at peak wavelength of about 425 nm. The low lasing threshold of the cavities enables lasing emission through excitation via 2-photon absorption (2PA) with 800 nm pump pulses, as well as 3-photon absorption (3PA) with 1280 nm pump pulses, at low temperature (83 K) and pressure ( $10^{-3}$  mbar). Second, plasmonic laser cavity is also designed using  $\text{Yb}^{3+}\text{-Er}^{3+}\text{-Tm}^{3+}$  tri-doped  $\beta\text{-NaYF}_4$  hexagonal microrods as the gain material. White light emission, which is contributed by emissions from the red (654 nm), green (540 nm) and blue (450 nm) regimes, can be obtained from the gain medium through 980-nm excitation at room temperature. The laser is constructed by placing the  $\text{NaYF}_4$  microrods with 4- $\mu\text{m}$  diameter onto an Ag-coated (50 nm) substrate, which alters the light distribution and enhances the emission intensity of WGM by more than 10 times due to plasmonic effect compared to a bare microrod without Ag coating. A micro-sized rod of the gain material ensures most of the light in the WGM is confined within it without a significant amount of metallic absorption in the Ag layer. This results in a much lower lasing threshold and compensates for the low quantum yield of the doped  $\text{NaYF}_4$  in order to achieve lasing, without requiring extremely high excitation power that often causes severe optical damage to the cavity.



# Acknowledgment

I would like to express my deepest gratitude to my supervisor Prof. YU Siu Fung for the continuous support during my Ph.D. study. With patience, enthusiasm and vast knowledge, his guidance provided tremendous help to my research work, as well as the writing of this thesis.

I thank my fellow schoolmates, as well as all of the teaching and non-teaching staff from the Department of Applied Physics, the Hong Kong Polytechnic University, for offering me much inspiration through stimulating discussions and the technical assistance on my research work. I would also like to thank them for the time we have spent together over the last four years. They have given me the strength to overcome the difficulty encountered in my journey towards this degree.

Last but not the least, I offer my special thanks to my family: my parents and my sister for their encouragement throughout my study. This work would not be possible without their precious support.



# Table of Contents

Certificate of Originality .....	ii
Abstract .....	iii
Acknowledgment .....	v
Table of Contents .....	vi
List of Figures .....	ix
List of Tables.....	xviii
1. Introduction.....	1
1.1. Overview of Optical Waveguides .....	1
1.2. Basic Formulation for Optical Mode Analysis .....	4
1.3. Surface Plasmon Excitation .....	8
1.4. Waveguide as Lasing Cavity.....	14
1.5. Upconversion Laser .....	18
1.6. Contribution of the Thesis.....	20
1.7. Conclusion .....	20
2. Theoretical Analysis of Cavity Modes.....	21
2.1. Two-layer Planar Slab Waveguide.....	21
2.2. Three-layer Planar Slab Waveguide.....	24





2.3.	Reflection Pole Method for Multi-layer Slab Waveguide .....	32
2.4.	Whispering-gallery Modes of Multi-layer Circular Waveguides .....	52
2.5.	Conclusion .....	66
3.	Experimental Study of Lasing Characteristics .....	67
3.1.	Spectral Analysis of Lasers .....	67
3.2.	Multiphoton Absorption and Z-scan Analysis .....	77
3.3.	Conclusion .....	82
4.	Multiphoton Excitation of Single-crystalline CsPbCl <sub>3</sub> Micro-cavities .....	83
4.1.	Background .....	83
4.2.	Synthesis and Characterization of CsPbCl <sub>3</sub> Microplates .....	85
4.3.	Nonlinear Absorption, PL, and ASE of Multiphoton-excited CsPbCl <sub>3</sub> Microplate Clusters .....	87
4.4.	Lasing Characteristics of Multiphoton-excited CsPbCl <sub>3</sub> Microplates .....	91
4.5.	Conclusion .....	97
5.	Influence of Plasmonic Effect on WGM lasing of NaYF <sub>4</sub> Hexagonal Microrods..	99
5.1.	Background .....	99
5.2.	Synthesis and Characterization of Yb <sup>3+</sup> -Er <sup>3+</sup> -Tm <sup>3+</sup> tri-doped $\beta$ -NaYF <sub>4</sub> Hexagonal Microrods .....	101
5.3.	Optical Measurement and Computer Simulation Method .....	104
5.4.	WGM Plasmonic Laser Design with $\beta$ -NaYF <sub>4</sub> Hexagonal Microrods .....	106



5.5. Effect of Excitation Polarization on the Emission Intensity of the Plasmonic Laser Design.....	108
5.6. Influence of Plasmonic Effect on the Emission Characteristics of the Plasmonic Microrod WGM Laser.....	111
5.7. Conclusion .....	115
Final Conclusion .....	117
Reference.....	119



# List of Figures

Figure 1.1	(a) Total internal reflection in a dielectric waveguide and (b) surface plasmon polariton in a metallic waveguide.....	2
Figure 1.2	Common waveguide shapes, including (a) planar slab, (b) cylindrical, (c) hexagonal and (d) triangular structures.....	3
Figure 1.3	Examples of waveguide structures fabricated for experimental study, including (a) layered frustum, (b) circular slabs and (c) hexagonal rod on planar slabs. .	3
Figure 1.4	2-layer semi-infinite planar slab waveguide.....	5
Figure 1.5	(a) $\epsilon_{rm}$ of a metal ( $\omega_p = 1.5 \times 10^{16}$ rad s <sup>-1</sup> ) at different values of $\omega$ according to the simple Drude model and (b) the corresponding dispersion relation of an interface formed by such a metal with a dielectric ( $\epsilon_{rd} = 1$ ). $k_d$ is the wavenumber in the dielectric. ....	11
Figure 1.6	(a) Schematic diagram of surface plasmon excitation at an air-metal interface using light coupled from a dielectric prism; (b) dispersion relation of the air-metal bound modes overlapped with the light lines of air and the dielectrics. ....	13
Figure 1.7	Principle of (a) three-level and (b) four-level laser. ....	15
Figure 1.8	(a) Simple Fabry-Pérot Laser Cavity and (b) its 2-D side-view schematic. ....	16
Figure 1.9	Principle of (a) downconversion and (b) 2-photon upconversion lasers. ....	19
Figure 2.1	(a) Dispersion relation of bound modes in an air-metal interface using the simple Drude model ( $\omega_p = 1.5 \times 10^{16}$ rad s <sup>-1</sup> ) and (b) the $ S_z $ distributions of bound modes at different frequencies. ....	22
Figure 2.2	Dispersion relation of an air-metal interface using a modified Drude model with electron collision damping.....	24



Figure 2.3	Three-layer planar slab waveguide.....	25
Figure 2.4	Dispersion relation of odd and even modes of IMI (air-gold-air) system with gold thicknesses $2a = 30$ nm and $2a = 60$ nm.....	28
Figure 2.5	Magnetic field ( $H_y$ ) distribution of the (a) odd mode and (b) even mode supported by the IMI (air-gold-air) system on the $xz$ -plane over a $2\ \mu\text{m} \times 2\ \mu\text{m}$ area, with gold thickness $2a = 30$ nm and wavelength $\lambda = 600$ nm (i.e. $\omega \approx 3.14 \times 10^{15}$ rad s <sup>-1</sup> ). The gold layer is assumed to be lossless, following the simple Drude model.....	29
Figure 2.6	Dispersion relation of odd and even modes of MIM (gold-air-gold) system with air gap thicknesses $2a = 30$ nm and $2a = 60$ nm. ....	30
Figure 2.7	Magnetic field ( $H_y$ ) distribution of the (a) odd mode and (b) even mode supported by the MIM (gold-air-gold) system on the $xz$ -plane over a $0.3\ \mu\text{m} \times 0.3\ \mu\text{m}$ area, with air gap thickness $2a = 60$ nm and wavelength $\lambda = 200$ nm (i.e. $\omega \approx 9.42 \times 10^{15}$ rad s <sup>-1</sup> ). The gold layer is assumed to be lossless, following the simple Drude model.....	31
Figure 2.8	$N$ -layer planar slab waveguide.....	33
Figure 2.9	Dispersion relation of 1-dimensional gold-air-gold (MIM) system with semi-infinite gold layers and air gap thickness $2a = 100$ nm. The black dashed lines indicate both odd and even mode (Mode 1 & 2) exists at wavelength $\lambda = 250$ nm, and only odd mode (Mode 3) exists at $\lambda = 600$ nm.....	37
Figure 2.10	Phase derivative of $t_{22}$ ( $d\phi/dn_r$ ) against real part index ( $n_r$ ) of the gold-air-gold system (air gap thickness $2a = 100$ nm) for (a) $\lambda = 250$ nm and (b) $\lambda = 600$ nm. The imaginary part index ( $n_i$ ) is set as zero. Simple Drude model is used to model the relative permittivity of gold, with $-0.0001$ as the fixed imaginary part. ....	38



- Figure 2.11 Magnetic field ( $H_y$ ) distribution of Mode 1 to 3 supported by the MIM (gold-air-gold) system on the  $xz$ -plane, with air gap thickness  $2a = 100$  nm. The dimension of each of the plots is  $1\ \mu\text{m} \times 1\ \mu\text{m}$ , and  $\text{Im}(\epsilon_{r1}) = \text{Im}(\epsilon_{r3}) = -0.0001$ . ..... 39
- Figure 2.12 (a) 3-D schematic of the GaN laser designed by Zhang et al. in Ref. [13], with a GaN triangular rod placed on a piece of  $\text{SiO}_2$ -coated Al. (b) shows the cross-section of the simplified semi-infinite planar waveguide structure (right) considered for theoretical analysis by RPM, compared to that of the original structure (left). The simulation result by Zhang et al. [13] on the original structure is shown in (c), and that by RPM on the simplified planar structure is shown in (d). The material refractive indices used in RPM are the same as those used in Ref. [13]. ..... 41
- Figure 2.13 (a) Oblique, (b) front and (c) top view of the proposed GaN laser for 2-D RPM analysis. .... 42
- Figure 2.14 Deduced modal  $|S_z|$  distribution of the planar plasmonic slot laser for  $t_{\text{GaN}} = 68$  nm,  $t_{\text{SiO}_2} = 8$  nm and  $t_{\text{Al}} = 40$  nm using (a) 2-D RPM and (b) finite-element method (COMSOL Multiphysics 5.0). ..... 43
- Figure 2.15 (a) Real part index  $n_{r,x2}$ , (b) imaginary part index  $n_{i,x2}$ , (c) confinement factor  $\Gamma$  and (d) effective threshold gain  $G_{\text{th}}$  of the GaN laser formed by square-based GaN rod ( $t_{\text{GaN}} = 68$  nm) on  $\text{SiO}_2$ -Al- $\text{SiO}_2$  planar structure for various Al thicknesses ( $t_{\text{Al}}$ ) when the thickness of  $\text{SiO}_2$  separation layer ( $t_{\text{SiO}_2}$ ) is fixed at 4, 8, 15 and 50 nm, calculated by 2-dimensional RPM. (e) and (f) respectively show the deduced modal magnitude distribution of the  $z$ -component of the Poynting vector  $|S_z|$  of the laser for  $t_{\text{Al}} = 5$  nm and  $t_{\text{Al}} = 40$  nm, when  $t_{\text{GaN}} = 68$  nm and  $t_{\text{SiO}_2} = 8$  nm. .... 45
- Figure 2.16 Explanation of the existence of local maxima in Figure 2.14c. .... 47
- Figure 2.17 (a) Real part index  $n_{r,x2}$ , (b) imaginary part index  $n_{i,x2}$ , (c) confinement factor  $\Gamma$  and (d) effective threshold gain  $G_{\text{th}}$  of the GaN laser formed by square-based



GaN rod ( $t_{\text{GaN}} = 68$ nm) on $\text{SiO}_2$ -Al- $\text{SiO}_2$ planar structure ( $t_{\text{Al}} = 40$ nm) for various $\text{SiO}_2$ thicknesses ( $t_{\text{SiO}_2}$ ), calculated by 2-dimensional RPM. (e) and (f) respectively show the deduced modal magnitude distribution of the $z$ -component of the Poynting vector $ S_z $ of the laser with and without an 8-nm $\text{SiO}_2$ separation layer. ....	49
Figure 2.18 (a) Real part index $n_{r,x2}$ , (b) imaginary part index $n_{i,x2}$ , (c) confinement factor $\Gamma$ and (d) effective threshold gain $G_{\text{th}}$ of the GaN laser formed by square-based GaN on $\text{SiO}_2$ -Al- $\text{SiO}_2$ planar structure ( $t_{\text{SiO}_2} = 8$ nm; $t_{\text{Al}} = 40$ nm) for various GaN side lengths ( $t_{\text{GaN}}$ ), calculated by 2-dimensional RPM. (e) and (f) respectively show the deduced modal magnitude distribution of the $z$ -component of the Poynting vector $ S_z $ of the laser when $t_{\text{GaN}} = 68$ nm and $t_{\text{GaN}} = 100$ nm. ....	51
Figure 2.19 3-D multi-layer cylindrical structure (left) and its corresponding 2-D representation (right). $r$ , $\phi$ and $z$ represent the radial, azimuthal and longitudinal positions, respectively. ....	53
Figure 2.20 2-D radially-layered circular laser designed by Yao et al. [23]. ....	58
Figure 2.21 Real $H_z$ distribution of (b) $\text{TM}_{2,2}$ and (a) $\text{TM}_{2,1}$ mode of a bare active core of radius $R_1 = 400$ nm with and without a 50-nm gold layer, respectively; real $H_z$ distribution of (c) $\text{TM}_{9,2}$ and (a) $\text{TM}_{9,1}$ mode of a bare active core of radius $R_1 = 1000$ nm with and without a 50-nm gold layer, respectively. ....	59
Figure 2.22 (a) Mode wavelength $\lambda_0$ , (b) confinement factor $\Gamma$ , (c) quality factor $Q$ and (d) threshold gain $G_{\text{th}}$ of the $\text{TM}_{2,1}$ ( $\text{TM}_{2,2}$ ) mode ( $R_1 = 400$ nm) (blue curves) and the $\text{TM}_{9,1}$ ( $\text{TM}_{9,2}$ ) mode ( $R_1 = 1000$ nm) (red curves) of a bare active core with different gold layer thicknesses $t_{\text{Au}}$ . ....	60
Figure 2.23 (a) Mode wavelength $\lambda_0$ , (b) confinement factor $\Gamma$ , (c) quality factor $Q$ and (d) threshold gain $G_{\text{th}}$ of the $\text{TM}_{10,1}$ (blue curves) and $\text{TM}_{10,2}$ (red curves) modes in the	



circular cavity with an active core of radius $R_1 = 1000$ nm and gold layer thickness $t_{\text{Au}} = 200$ nm, when the thickness of the separation layer ( $t_{\text{sep}}$ ) varies from 0 to 1000 nm.....	63
Figure 2.24 Real $H_z$ distribution of the $\text{TM}_{10,1}$ and $\text{TM}_{10,2}$ modes in the circular cavity with separation layer of thickness $t_{\text{sep}} = 0$ nm, 200 nm, 600 nm, 750 nm, 800 nm and 1000 nm inserted between the active core ( $R_1 = 1000$ nm) and the gold layer ( $t_{\text{Au}} = 200$ nm). .....	64
Figure 3.1 Wavelength spectrum of photoluminescence (PL) and amplified spontaneous emission (ASE) of a gain medium, and that of laser emission upon feedback of ASE inside a laser cavity. (The figure is modified from Ref. [26]) .....	68
Figure 3.2 Wavelength spectrum of a $\text{CH}_3\text{NH}_3\text{PbI}_3$ nanowire at various levels of pump fluence (pump density). Inset: The corresponding light-light curve (black dots) and FWHM plotted against pump fluence (blue triangles). (Figure from Ref. [28]) .....	69
Figure 3.3 (a) A Czerny-Turner monochromator [30] and (b) its corresponding schematic diagram [31]. .....	71
Figure 3.4 Schematic diagram of the configuration of room temperature spectral measurement for bulk samples through pulsed laser excitation.....	72
Figure 3.5 (a) Front view and (b) side view of the micro quartz cuvette filled with rhodamine 6G (R6G) solution, and (c) the orientation of the cuvette during PL measurement of the sample.....	73
Figure 3.6 PL spectra of the R6G solution at different pump powers. ....	74
Figure 3.7 Microscope system for spectral analysis of small samples. (Figure modified from Ref. [33]) .....	75
Figure 3.8 Microscope images of (a) perovskite nanowire [34], (b) perovskite microplates [35] and (c) ZnO nanowire [36] under optical excitation.....	76



Figure 3.9	Wavelength spectra of the emission from a crystalline polymer random laser excited at different pump powers. Inset: the corresponding light-light curve, showing that the PL regime has a slope close to 2, which confirms the spontaneous emission is induced by 2-photon absorption (2PA). (Figure from Ref. [40]).....	78
Figure 3.10	Configuration of the open-aperture z-scan technique.....	79
Figure 3.11	Experimental open-aperture z-scan signature of a platinum acetylide complex, with the corresponding fitted curves for 2PA and 3PA. (Figure from Ref. [42]) .....	81
Figure 4.1	Crystal structure of halide perovskite. (Figure from Ref. [43]).....	84
Figure 4.2	(a) Scanning electron microscope (SEM) images, (b) X-ray diffraction (XRD) pattern, (c) photoluminescence (PL)/absorption spectra of the $\text{CsPbCl}_3$ microplates. The PL is obtained from linear excitation using 355-nm photons; (d) Tunnelling electron microscope (TEM) images, and the corresponding selected area electron diffraction (SAED) pattern of a single $\text{CsPbCl}_3$ microplate. ....	86
Figure 4.3	(a) Emission spectra, (c) linewidth and light-light curve of the $\text{CsPbCl}_3$ microplate clusters under 800-nm excitation at different pump densities; (b) emission spectra, (d) linewidth and light-light curve of the $\text{CsPbCl}_3$ microplate clusters under 1280-nm excitation at different pump densities. All measurements are taken at temperature $T = 83$ K. ....	89
Figure 4.4	(a) Light-light curve in the PL regime under log-log scale and (c) z-scan data of the $\text{CsPbCl}_3$ microplate clusters under 800-nm excitation; (b) light-light curve in the PL regime under log-log scale and (d) z-scan data of the $\text{CsPbCl}_3$ microplate clusters under 1280-nm excitation. The measurement of the light-light curves is taken at $T = 83$ K, whereas that of the z-scan data is taken at room temperature $T = 298$ K. ....	90





Figure 4.5 (a) Emission spectra and (b) light-light curve of a CsPbCl <sub>3</sub> microplate ( $W = 8.9 \mu\text{m}$ ) under 800-nm excitation at 83 K; (c) emission spectra and (d) light-light curve of a CsPbCl <sub>3</sub> microplate ( $W = 8.9 \mu\text{m}$ ) under 1280-nm excitation at 83 K; (e) plot of $\Delta\lambda$ versus $1/L$ obtained from the CsPbCl <sub>3</sub> microplates with different $W$ . (f) Semi-log plot of $P_{\text{th}}$ versus $W$ of the CsPbCl <sub>3</sub> microplates under 800-nm and 1280-nm excitation at 83 K.	92
Figure 4.6 (a) Emission spectra and (b) light-light curve of a CsPbCl <sub>3</sub> microplate ( $W = 3.7 \mu\text{m}$ ) under 1280-nm excitation at 83 K. The optical microscope images of the same single microplate before and during excitation are shown in (c) and (d), respectively.	95
Figure 4.7 (a) Theoretically calculated electric field strength $ E $ distribution of the lasing mode supported by the CsPbCl <sub>3</sub> microplate of side length $W = 3.7 \mu\text{m}$ over the microplate's surface, and (b) the explanation of the support of single-WGM operation from the microplate.	96
Figure 5.1 (a) – (c) SEM images of the NaYF <sub>4</sub> microrods. (d) The size distribution of NaYF <sub>4</sub> microrods in (a), and the schematic diagram of a single NaYF <sub>4</sub> microrod. It is noted that the radius of the microrods varies from 0.5 to 4.5 $\mu\text{m}$ . The microrods, in general, have six flat surfaces and two sharp ends. Under optical excitation, whispering-gallery modes (i.e. red arrows) are established on the hexagonal flat surfaces to support coherent optical feedback (i.e. lasing emission).	102
Figure 5.2 (a) XRD pattern of the as-synthesized Yb <sup>3+</sup> –Er <sup>3+</sup> –Tm <sup>3+</sup> tri-doped $\beta$ -NaYF <sub>4</sub> hexagonal microrods. The inset shows the corresponding SEM image. (b) HR-TEM and FFT image of the $\beta$ -NaYF <sub>4</sub> hexagonal microrod.	103
Figure 5.3 Experimental setup for the PL and lasing spectra measurement of a NaYF <sub>4</sub> microrod.	105



- Figure 5.4 (a) Plot of calculated Q-factor of a  $\text{NaYF}_4:\text{Yb}^{3+}, \text{Er}^{3+}, \text{Tm}^{3+}$  hexagonal microrod ( $r = 2 \mu\text{m}$ ) deposited on an Ag-coated (50 nm) substrate, which is also protected by a  $\text{MgF}_2$  dielectric layer with different thickness. (b) Measured spontaneous emission spectra from a microrod ( $r = 2 \mu\text{m}$ ) deposited on an Ag-coated substrate with a different thickness of  $\text{MgF}_2$  protection layer, as well as that from a bare microrod without Ag and  $\text{MgF}_2$ ..... 107
- Figure 5.5 (a) Emission spectra of a  $\text{NaYF}_4:\text{Yb}^{3+}, \text{Er}^{3+}, \text{Tm}^{3+}$  hexagonal microrod deposited on an Ag-coated substrate under 980-nm laser excitation with two orthogonal orientations  $\theta_{\text{in}} = 90^\circ$  (perpendicular to the length of the microrod) and  $\theta_{\text{in}} = 0^\circ$  (parallel to the length of the microrod); (b) the corresponding microscope images of the microrod at these two polarizations. (c) Two-dimensional plot of emission intensity versus  $\theta_{\text{in}}$  and emission wavelength. .... 110
- Figure 5.6 PL characteristics of (a)  $\text{NaYF}_4:\text{Yb}^{3+}, \text{Er}^{3+}$  and (b)  $\text{NaYF}_4:\text{Yb}^{3+}, \text{Tm}^{3+}$  hexagonal microrods ( $r = 2 \mu\text{m}$ ) under excitation at polarizations (i.e.  $\theta_{\text{in}} = 0^\circ$  and  $90^\circ$ ). At  $\theta_{\text{in}} = 90^\circ$ , the emission intensity is enhanced by 30% compared to that using  $\theta_{\text{in}} = 0^\circ$ . .... 111
- Figure 5.7 Photos of a  $\text{NaYF}_4:\text{Yb}^{3+}, \text{Er}^{3+}, \text{Tm}^{3+}$  hexagonal microrod ( $r = 2 \mu\text{m}$ ) deposited on the Ag-coated substrate under (a) edge and (b) center excitation. The corresponding photos for the microrods deposited on a substrate without Ag coating are also shown for comparison..... 112
- Figure 5.8 (a) Light–light curves of the hexagonal microrods with and without deposition on a 50-nm Ag coat for the emission peaks of the three colors (i.e.,  $\sim 450$ ,  $\sim 540$  and  $\sim 654$  nm). (b) Corresponding emission spectra of the hexagonal microrods



with and without deposition on the Ag-coated substrate at a pumped density of 3.5 mJ / cm<sup>2</sup> . ..... 113

Figure 5.9 Numerical simulation results of the  $|E|^2$  distribution of the resonant modes inside a hexagonal microrod at different wavelengths (450, 540, and 654 nm) (c) with and (a) without the Ag-coated substrate; Near-field photo of a hexagonal microrod (d) with and (b) without the Ag-coated substrate under 980-nm pulsed excitation. .... 115



# List of Tables

Table 1 Values of $\beta$ ( $\times 10^8 \text{ m}^{-1}$ ) of Mode 1 to 3 of the gold-air-gold system ( $2a = 100$ nm) deduced by RPM and by Equation (2.16) for $\lambda = 250$ nm and $\lambda = 600$ nm, up to 12 significant figures.....	39
---	----



# 1. Introduction

To give a general idea of this work, this chapter discusses the basic information on plasmonic upconversion lasers made of waveguide structures, as well as the main contributions of the thesis.

## 1.1. Overview of Optical Waveguides

Waveguides are structures which transport energy of waves. In particular, optical waveguides are designed for wavelengths within the visible-infrared range. The topic of optical waveguides was studied since the early 20<sup>th</sup> century and started to draw attention from researchers since the 1960s with a well-established theory based on Maxwell's equations. [1, 2] During that time, waveguide designs using dielectric was the main focus, and various useful applications had been invented as technology advanced, especially optical fibers for energy and signal transmission.

Optical waveguides can be classified according to the materials they are made of. Waveguides made of only dielectric are called dielectric waveguides, whereas those including any metallic part can be regarded as metallic waveguides. The former kind transmits light by total internal reflection, in which light is well confined within the high-index dielectric, with small amount of optical loss due to material absorption and scattering (Figure 1.1a). This leads to the great performance of its applications. However, dielectric waveguides cannot be applied to devices with scales comparable to or smaller than the operation wavelength because of the diffraction limit. As the demand of micro- and nano-devices grows, researches in the 21<sup>st</sup> century started to focus more

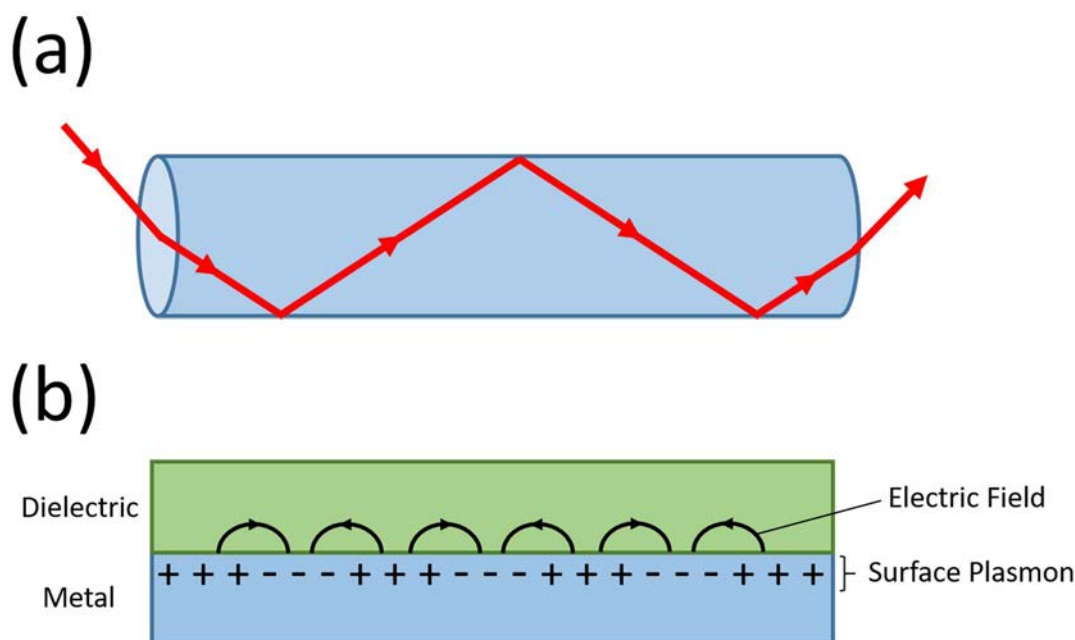


**Figure 1.1 (a) Total internal reflection in a dielectric waveguide and (b) surface plasmon polariton in a metallic waveguide.**

on metallic waveguides, which enabled subwavelength confinement of the propagating light by surface plasmon formation at the metal-dielectric interfaces (Figure 1.1b).

There are a variety of typical waveguide shapes, with the planar slab structure being one of the most common types. Other examples include cylindrical, hexagonal and triangular structures as shown in Figure 1.2. In practice, despite the exact waveguide structures may vary with added complexity, they are usually designed based on these simple shapes, especially in small-scale optical devices, because they have excellent waveguiding properties and are easy to fabricate by film deposition and crystal growth. A few examples of complex structures used in experimental studies are shown in Figure 1.3 [3-5]. Adopting highly-symmetric geometry in waveguide designs is also advantageous in theoretical analysis, as simpler mathematical models can be used for performance optimization, which would be further discussed in following sections.

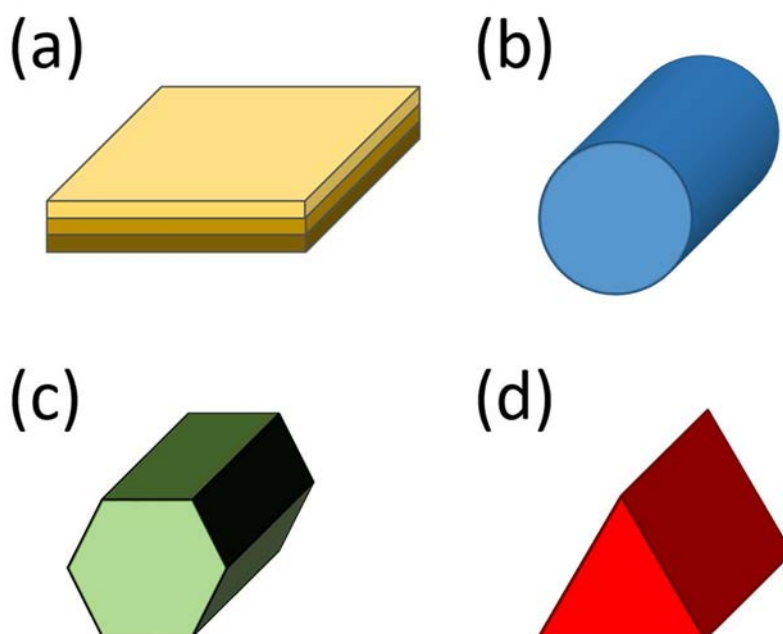


**Figure 1.2** Common waveguide shapes, including (a) planar slab, (b) cylindrical, (c) hexagonal and (d) triangular structures.

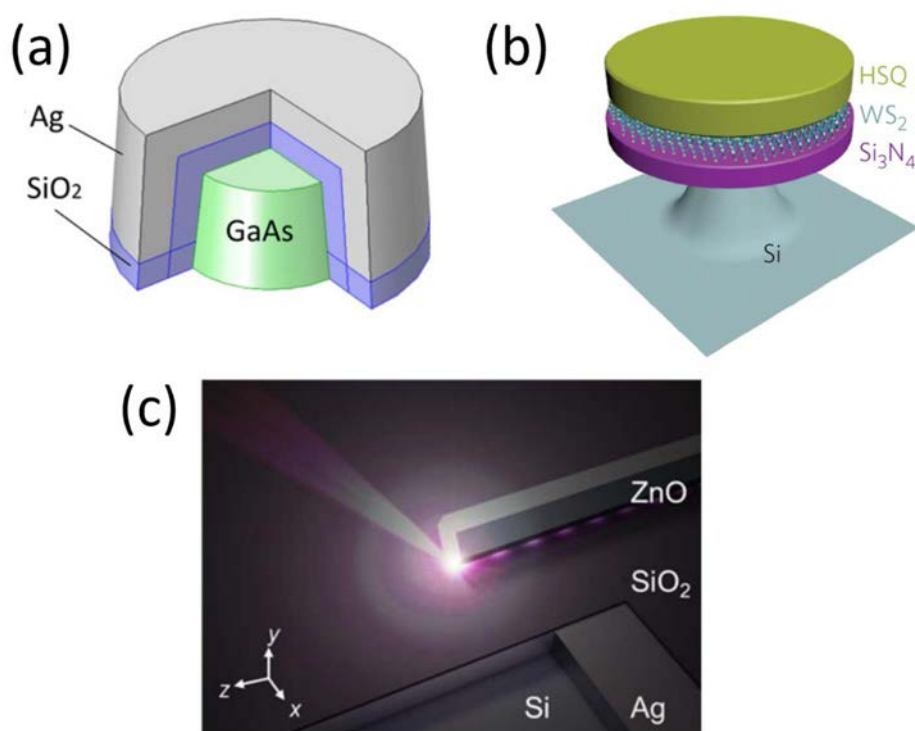


**Figure 1.3** Examples of waveguide structures fabricated for experimental study, including (a) layered frustum, (b) circular slabs and (c) hexagonal rod on planar slabs.



## 1.2. Basic Formulation for Optical Mode Analysis

In an optical waveguide, there exists a number of modes, depending on its physical features and the surrounding environmental conditions. A mode is a specific distribution of electric and magnetic field that exists in the waveguide without attenuation due to destructive interference. This is important to study in order to optimize the optical energy distribution in any laser design to fit its purpose. Typically, a mathematical model for optical mode analysis is derived from the Maxwell equations

$$\nabla \cdot \vec{E} = \frac{\rho_v}{\epsilon_0} \quad (1.1)$$

$$\nabla \cdot \vec{H} = 0 \quad (1.2)$$

$$\nabla \times \vec{E} = -\mu \frac{\partial \vec{H}}{\partial t} \quad (1.3)$$

$$\nabla \times \vec{H} = \vec{J} + \epsilon \frac{\partial \vec{E}}{\partial t}, \quad (1.4)$$

where  $\vec{E}$ ,  $\vec{H}$ ,  $\vec{J}$ ,  $t$ ,  $\rho_v$ ,  $\mu$ ,  $\epsilon$  and  $\epsilon_0$  are the electric field, magnetic field, electric current density, time, total volume charge density, permeability, permittivity and vacuum permittivity, respectively. In our study, we can assume  $|\vec{J}| = \rho_v = 0$  and  $\mu = \mu_0$ , where  $\mu_0$  is the permeability of free space. By taking curls on both sides of Equations (1.3) and (1.4), we have

$$\nabla \times (\nabla \times \vec{E}) = -\mu \frac{\partial (\nabla \times \vec{H})}{\partial t} = -\mu \epsilon \frac{\partial^2 \vec{E}}{\partial t^2} = -\mu_0 \epsilon_0 \epsilon_r \frac{\partial^2 \vec{E}}{\partial t^2} \quad (1.5)$$

$$\nabla \times (\nabla \times \vec{H}) = \epsilon \frac{\partial (\nabla \times \vec{E})}{\partial t} = -\mu \epsilon \frac{\partial^2 \vec{H}}{\partial t^2} = -\mu_0 \epsilon_0 \epsilon_r \frac{\partial^2 \vec{H}}{\partial t^2}, \quad (1.6)$$



where  $\varepsilon_0$  and  $\varepsilon_r$  are the permittivity of free space and relative permittivity respectively, since  $\varepsilon = \varepsilon_0 \varepsilon_r$ . By using the identity that  $\nabla \times (\nabla \times \vec{A}) \equiv \nabla (\nabla \cdot \vec{A}) - \nabla^2 \vec{A}$  for any vector  $\vec{A}$ , as well as Equations (1.1) and (1.2), Equations (1.5) and (1.6) can be written as

$$\nabla^2 \vec{\psi} = \mu_0 \varepsilon_0 \varepsilon_r \frac{\partial^2 \vec{\psi}}{\partial t^2}, \quad (1.7)$$

where  $\vec{\psi} = \vec{E}$  or  $\vec{H}$ . The equation (1.7) is the wave equation commonly used in optics. It effectively expresses the Maxwell equations with a single equation in one unknown, which much simplifies the problem. To solve Equation (1.7), we can consider using a trial solution. The solution should describe  $\vec{\psi}$  fully in the type of mode being analyzed. As an example, we now consider the guided modes in a 2-layer semi-infinite planar slab waveguide as shown in Figure 1.4 below.

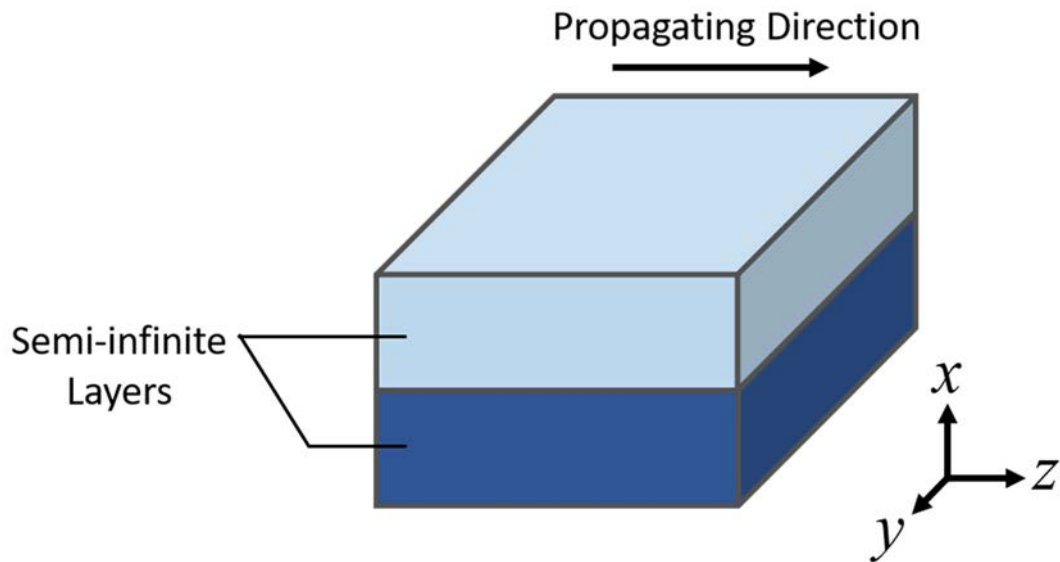


**Figure 1.4** 2-layer semi-infinite planar slab waveguide



In this particular waveguide, the guided modes are expected to oscillate in harmonic time dependence as they propagate along the  $z$ -direction. Therefore, we can describe  $\bar{\psi}$  mathematically as

$$\bar{\psi}(x, y, z, t) = \bar{\psi}_0(x) \exp[j(\omega t - \beta z)], \quad (1.8)$$

where  $\bar{\psi}_0$  is a function in  $x$ , and  $\omega$  and  $\beta$  are the angular frequency and the propagation constant in the  $z$ -direction, respectively. By putting (1.8) into (1.7), we have the Helmholtz equation

$$\frac{\partial^2 \bar{\psi}}{\partial x^2} + (k_0^2 \epsilon_r - \beta^2) \bar{\psi} = 0, \quad (1.9)$$

where  $k_0 = \omega \sqrt{\mu_0 \epsilon_0}$  is the vacuum wavenumber. At this point, we need to determine whether it is more convenient to solve for  $\bar{\psi}$  as  $\bar{E}$  or  $\bar{H}$  in Equation (1.9). To do this, we need to find out the relationship between all of the field components by putting (1.8) into (1.3) and (1.4). This result gives

$$\left(-\frac{\partial E_y}{\partial z}\right) \hat{x} + \left(\frac{\partial E_x}{\partial z} - \frac{\partial E_z}{\partial x}\right) \hat{y} + \left(\frac{\partial E_y}{\partial x}\right) \hat{z} = j\omega\mu_0 (H_x \hat{x} + H_y \hat{y} + H_z \hat{z}) \quad (1.10)$$

$$\left(-\frac{\partial H_y}{\partial z}\right) \hat{x} + \left(\frac{\partial H_x}{\partial z} - \frac{\partial H_z}{\partial x}\right) \hat{y} + \left(\frac{\partial H_y}{\partial x}\right) \hat{z} = -j\omega\epsilon_0\epsilon_r (E_x \hat{x} + E_y \hat{y} + E_z \hat{z}), \quad (1.11)$$

where  $E_x$ ,  $E_y$ ,  $E_z$ ,  $H_x$ ,  $H_y$ , and  $H_z$  are the field components, with  $\hat{x}$ ,  $\hat{y}$  and  $\hat{z}$  being the unit vectors in the Cartesian coordinate plane, such that  $\bar{E} = E_x \hat{x} + E_y \hat{y} + E_z \hat{z}$  and  $\bar{H} = H_x \hat{x} + H_y \hat{y} + H_z \hat{z}$ . By comparing the three components in each of (1.10) and (1.11), we can get the following system of six equations.



$$H_x = \frac{\beta}{\omega\mu_0} E_y \quad (1.12)$$

$$H_z = -\frac{j}{\omega\mu_0} \frac{\partial E_y}{\partial x} \quad (1.13)$$

$$\frac{\partial^2 E_y}{\partial x^2} + (k_0^2 \epsilon_r - \beta^2) E_y = 0 \quad (1.14)$$

$$E_x = -\frac{\beta}{\omega\epsilon_0 \epsilon_r} H_y \quad (1.15)$$

$$E_z = \frac{j}{\omega\epsilon_0 \epsilon_r} \frac{\partial H_y}{\partial x} \quad (1.16)$$

$$\frac{\partial^2 H_y}{\partial x^2} + (k_0^2 \epsilon_r - \beta^2) H_y = 0. \quad (1.17)$$

It can be found that Equations (1.12), (1.13) and (1.14) form an independent system in  $H_x$ ,  $E_y$  and  $H_z$ , while Equations (1.15), (1.16) and (1.17) form another independent system in  $E_x$ ,  $H_y$ , and  $E_z$ . The former and latter system correspond to the transverse electric (TE) and transverse magnetic (TM) modes, respectively. Note that Equations (1.14) and (1.17) have exactly the same form as Equation (1.9) that we previously derived because  $E_y$  and  $H_y$  are respectively the only electric and magnetic field component in TE and TM modes. Therefore, for TE (TM) modes, it would be more convenient to solve  $E_y$  ( $H_y$ ) in Equation (1.14) (Equation (1.17)) first, followed by finding other field components that are already expressed in terms of  $E_y$  ( $H_y$ ) in (1.12) and (1.13) ((1.15) and (1.16)).

In the above derivation, the assumption that the waveguide slabs are infinite on the  $yz$ -plane allows us to use a trial solution independent of  $y$  in (1.8), hence all of the



derivatives with respect to  $y$  becomes zero as shown in (1.10) and (1.11), effectively simplifying the problem. For this reason, in general, it is favorable to have the waveguide design as symmetric as possible. However, regardless of the waveguide geometry analyzed under any coordinate system, the mathematical deduction is usually similar to the case discussed in this section. Further details and analysis of the waveguide modes will be discussed in the next chapter.

### 1.3. Surface Plasmon Excitation

Surface plasmon (SP) can be excited at an interface formed by a dielectric and a conductive material (e.g. metal and semiconductor). Consider, in the waveguide mentioned in Figure 1.4, that the bottom layer (layer 1) is metallic and the top layer (layer 2) is dielectric, such a dielectric-metal interface is formed. When surface plasmon is excited, we expect that all the fields concentrate at the interface and they should decay exponentially as  $x \rightarrow \pm\infty$ . By letting  $x = 0$  be the position of the interface, we can describe  $E_y$  and  $H_y$ , according to (1.8), as

$$\psi_{y1} = \psi_{y1,0}(x) \exp[j(\omega t - \beta z)] = A_1 \exp[k_{x1}x + j(\omega t - \beta z)] \quad (1.18)$$

in layer 1 and

$$\psi_{y2} = \psi_{y2,0}(x) \exp[j(\omega t - \beta z)] = A_2 \exp[-k_{x2}x + j(\omega t - \beta z)] \quad (1.19)$$

in layer 2, where  $k_{xi} > 0$  is the propagation constant in layer  $i$  in the  $x$ -direction and  $A_i$  is a constant ( $i = 1, 2$ ). Now, we can apply the boundary conditions for (1.18) and (1.19) at  $x = 0$ . The boundary conditions require each of the field components that is tangential to the interface to be equal in both layers (since there is no surface current), and each of those being perpendicular to the interface to keep their amplitudes in both layers



according to their permittivity ratio (for electric field) or permeability ratio (for magnetic field). In our waveguide structure, they can be described as follows.

$$\varepsilon_{r1}E_{x1} = \varepsilon_{r2}E_{x2} \quad (1.20)$$

$$H_{y1} = H_{y2} \quad (1.21)$$

$$E_{z1} = E_{z2} \quad (1.22)$$

$$H_{x1} = H_{x2} \quad (1.23)$$

$$E_{y1} = E_{y2} \quad (1.24)$$

$$H_{z1} = H_{z2}, \quad (1.25)$$

where  $\varepsilon_{r1}$  and  $\varepsilon_{r2}$  are the relative permittivities in layer 1 and 2 respectively. As a result, by considering the boundary  $x = 0$ , for TE modes, we have

$$A_1 = A_2 \quad (1.26)$$

$$A_1 k_{x1} = -A_2 k_{x2}. \quad (1.27)$$

This leads to the requirement that  $A_1(k_{x1} + k_{x2}) = 0$ . However, in our convention,  $\text{Re}(k_{x1})$  and  $\text{Re}(k_{x2})$  are positive, so  $k_{x1} + k_{x2} \neq 0$ . This leads to the conclusion that  $A_1 = A_2 = 0$ . Thus, all field components become zero in this case and we cannot have SP in TE mode. In contrast, for TM mode, the boundary conditions are

$$A_1 = A_2 \quad (1.28)$$

$$A_1 \varepsilon_{r2} k_{x1} = -A_2 \varepsilon_{r1} k_{x2}. \quad (1.29)$$

Since  $\varepsilon_{r2}k_{x1} + \varepsilon_{r1}k_{x2}$  can be zero, this system can be solved in the case  $A_1 = A_2 \neq 0$ . By putting  $H_{yi} = A_i \exp[\pm k_{xi}x + j(\beta z - \omega t)]$  into Equation (1.9), we can express  $k_{xi}$  as

$$k_{xi}^2 = \beta^2 - k_0^2 \varepsilon_{ri}. \quad (1.30)$$

Combining (1.29) and (1.30) we have the dispersion relation

$$\beta = k_0 \sqrt{\frac{\varepsilon_{r1}\varepsilon_{r2}}{\varepsilon_{r1} + \varepsilon_{r2}}} = \frac{\omega}{c} \sqrt{\frac{\varepsilon_{r1}\varepsilon_{r2}}{\varepsilon_{r1} + \varepsilon_{r2}}}, \quad (1.31)$$

where  $c$  is the speed of light in vacuum. It proves that SP exists for TM mode. Therefore, we can conclude that all of the plasmonic modes can only be TM modes but not TE modes.

At this point, for enhanced readability, we put  $\varepsilon_{r1} = \varepsilon_{\text{m}}$  and  $\varepsilon_{r2} = \varepsilon_{\text{d}}$ , corresponding to the relative permittivities of the metallic and the dielectric layer respectively. To visualize (1.31), we first assume  $\varepsilon_{\text{m}}$  follows the simple Drude model [6]

$$\varepsilon_{\text{m}} = 1 - \frac{\omega_{\text{p}}^2}{\omega^2}, \quad (1.32)$$

where  $\omega_{\text{p}}$  is the bulk plasma frequency. This model assumes the electrons in the metal are completely free, neglecting the damping effect due to electron motion and interband transitions. However, it still gives useful insights for plasmonic waveguide design in a simple manner by having purely real  $\varepsilon_{\text{m}}$ . Here, for  $\omega_{\text{p}} = 1.5 \times 10^{16} \text{ rad s}^{-1}$  and  $\varepsilon_{\text{d}} = 1$  (i.e. air), the Drude model in (1.32) and the dispersion relation (1.31) are plotted in Figure 1.5. From Figure 1.5a, it can be seen that  $\varepsilon_{\text{m}} < 0$  only if  $\omega < \omega_{\text{p}}$ , indicating that the

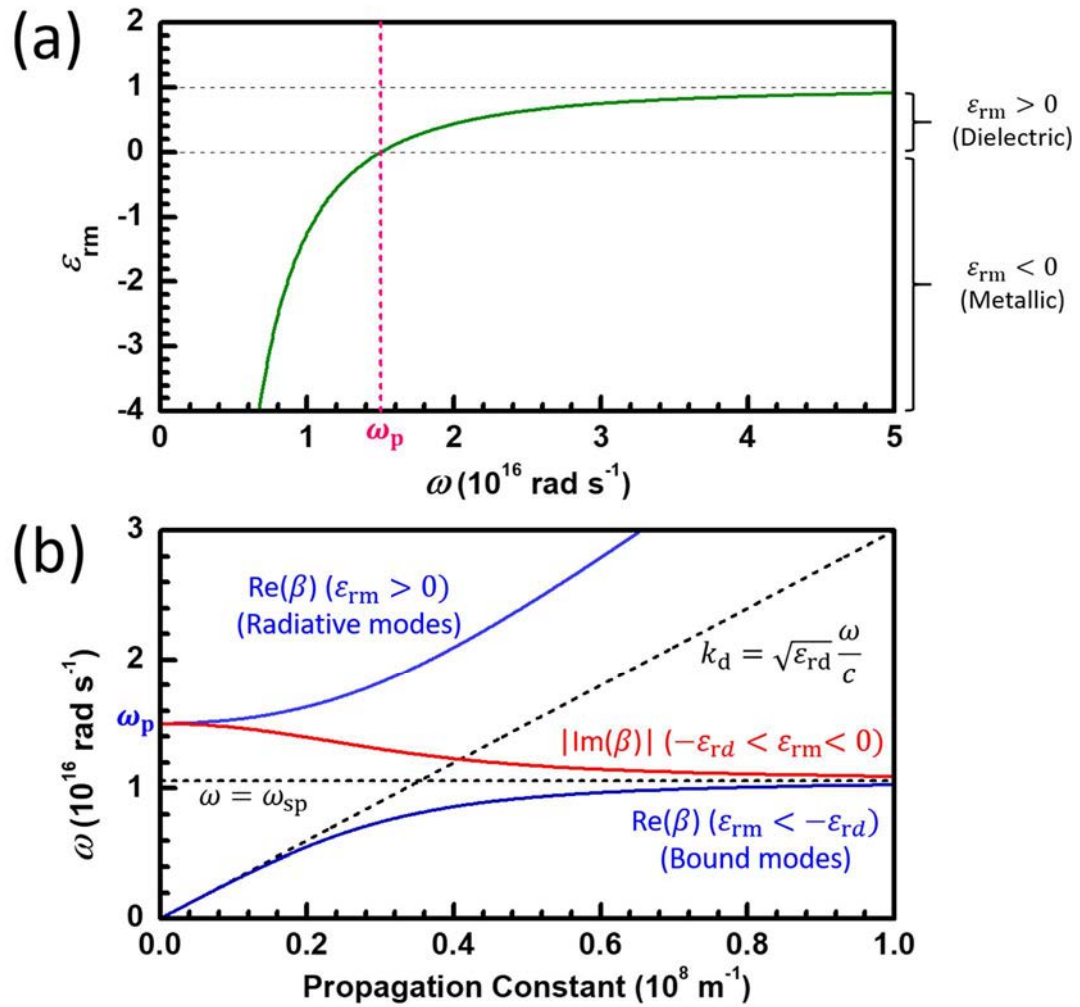


**Figure 1.5** (a)  $\epsilon_{rm}$  of a metal ( $\omega_p = 1.5 \times 10^{16} \text{ rad s}^{-1}$ ) at different values of  $\omega$  according to the simple Drude model and (b) the corresponding dispersion relation of an interface formed by such a metal with a dielectric ( $\epsilon_{rd} = 1$ ).  $k_d$  is the wavenumber in the dielectric.

metal shows its metallic behavior only at lower frequencies. In contrast, at higher frequencies such that  $\omega > \omega_p$ , the metal behaves like a dielectric. As a result, only at the regime  $\omega < \omega_p$  would the excitation of SP be possible. Then, we move on to look at more information about the optical modes at the dielectric-metal system by referring to the dispersion relationship plotted in Figure 1.5b. It is observed that the propagation constant  $\beta$  is purely real when  $\omega > \omega_p$  or  $\omega < \omega_{sp}$ , where  $\omega_{sp}$  is the surface plasmon



frequency. For  $\omega > \omega_p$ ,  $k_{x2}$  (mentioned in Equation (1.30)) is purely imaginary since  $\beta^2 < k_0^2 \epsilon_{rd}$  for any given value of  $\omega$  according to the plot. This indicates light propagates along both  $x$ - and  $z$ -direction freely in the dielectric without being confined at the interface, corresponding to the radiative modes. It also agrees with the previous conclusion from Figure 1.5a that the metallic layer behaves like a dielectric without SP formation. For another case with  $\omega < \omega_{sp}$ , both  $k_{x1}$  and  $k_{x2}$  are purely real, which means light decays exponentially as an evanescent wave in the  $x$ -direction in both layers, according to the field component expressions (1.18) and (1.19) used in the first place. However, since  $\beta$  is purely real, this forms bound modes with light propagating in the  $z$ -direction but is confined along the  $x$ -direction at the interface, which is the result of SP formation. As for the frequency range  $\omega_{sp} < \omega < \omega_p$ ,  $\beta$  is purely imaginary and quasi-bound modes are formed. We do not focus on it considering there is no light propagation along the interface.

After identifying the types of modes supported by a single dielectric-metal interface at different frequencies, we can now make further analysis regarding the excitation of SP (i.e. the bound modes). As discussed, for bound modes,  $\beta^2 > k_0^2 \epsilon_{rd}$  for any given excitation frequency. This gives us the important fact that it is impossible to have SP excited at a dielectric-metal interface by illuminating the metal surface through that same dielectric due to insufficient momentum. To solve this problem, we can do the excitation from a dielectric of higher  $\epsilon_r$  than the one that formed the interface, which is demonstrated in Figure 1.6. Figure 1.6a shows one of the possible set-ups to achieve this, with a piece of metal placed on a high-index dielectric prism. In this way, light directed inside the prism would have sufficient energy to excite SP at the air-metal



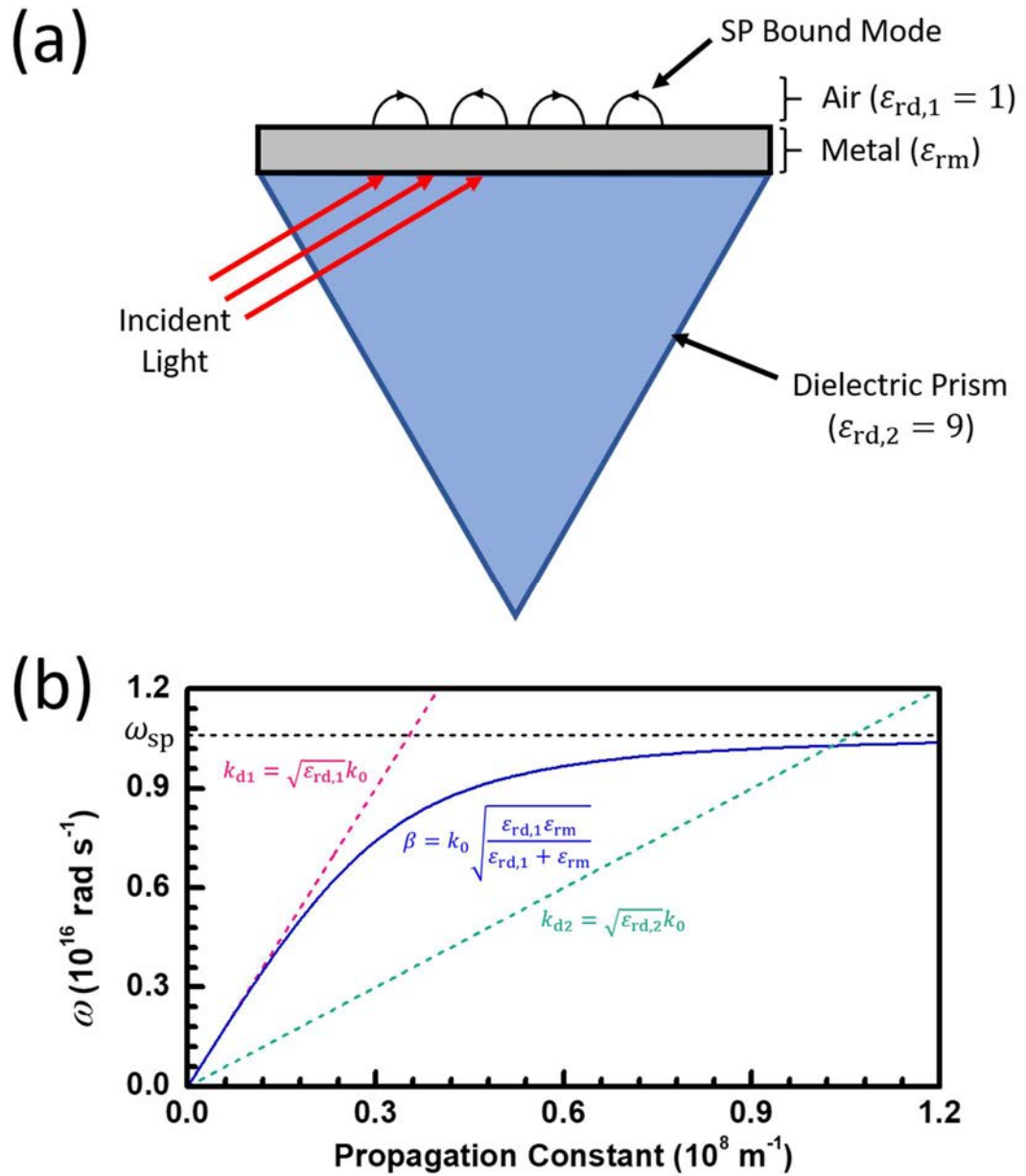


**Figure 1.6** (a) Schematic diagram of surface plasmon excitation at an air-metal interface using light coupled from a dielectric prism; (b) dispersion relation of the air-metal bound modes overlapped with the light lines of air and the dielectrics.

interface. The frequency range which allows SP excitation using this method highly depends on the relative permittivities of the interface dielectric and the prism, denoted by  $\epsilon_{rd,1}$  and  $\epsilon_{rd,2}$ , respectively. To illustrate this, the dispersion relation of the interface bound modes is overlapped with the light lines of air and the prism in Figure 1.6b. From



this plot, it can be pointed out that the photon momentum in the prism is higher than that in the interface bound modes for some  $\omega$ , which defines the region SP excitation is possible. In the light of this, in plasmonic laser design, materials used to fabricate the resonators should be chosen carefully such that bound modes at the operation wavelength can be excited easily in practice.

## 1.4. Waveguide as Lasing Cavity

A waveguide can be specifically designed for lasing purpose, in which a gain medium is inserted as part of the waveguide. A gain medium is a material which emits light with a characteristic wavelength when pumped from the ground energy level to higher energy level, followed by stimulated emission from the upper lasing level to the lower lasing level in a laser cavity. Figure 1.7a shows a three-level energy system [7], which explains one of the possible mechanisms for a gain medium to achieve lasing. In this system, the gain medium is pumped from the ground state (level 0) to a short-lived state (level 2), which transfers to a meta-stable state (level 1) as the upper lasing level. In a typical gain medium, the short-lived state should have a significantly shorter relaxation time than the upper lasing level, such that most of the pumped atoms would decay rapidly and stay at the upper lasing level for a long time. When the upper lasing level has more atoms than the lower lasing level (i.e. the ground state), it is said that the system has achieved population inversion. In this case, at the upper lasing level, most atoms which encounters a photon with energy equals to the bandgap between the upper and lower lasing levels would undergo stimulated emission, which causes the atom to fall back to the lower lasing level, generating a photon identical to the one triggered the process. Another example is the four-level system shown in Figure 1.7b, with level 1, 2

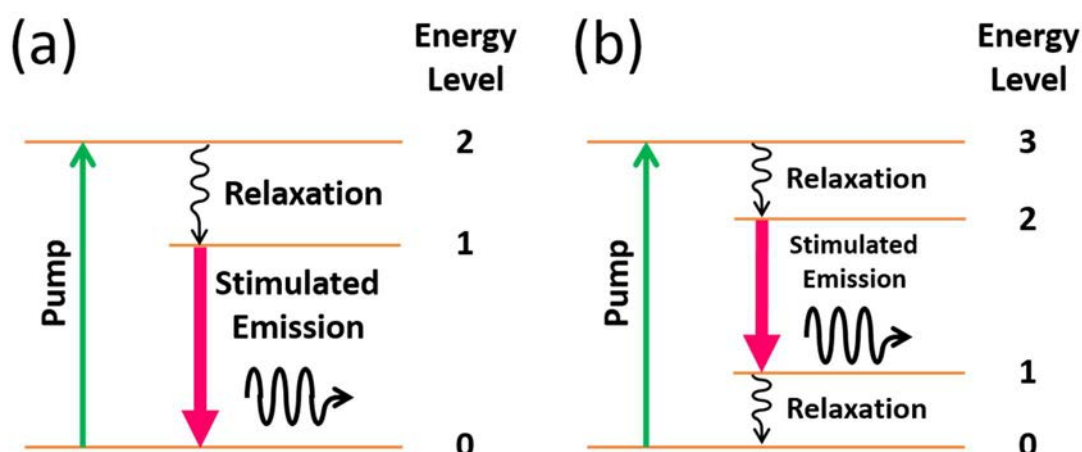


**Figure 1.7 Principle of (a) three-level and (b) four-level laser.**

and 3 being the lower lasing level, upper lasing level and short-lived state respectively. The only difference of this system compared to the three-level system is that the lower lasing level is not the ground state. In this case, it is desirable to have a short relaxation time for the lower lasing level. This allows replenishment of the atoms at the ground level quickly for the atoms to be pumped again.

In stimulated emission, since the generated photons are identical to the incoming ones, we can design waveguide structures which select and preserve photons propagating along a certain path to generate an intense coherent light beam. Such structures are called laser cavities. To illustrate how a laser cavity works, a simple Fabry-Pérot cavity in Figure 1.8a is used as an example. The cavity consists of a piece of gain medium with reflective mirrors at both ends. When the gain medium is pumped, photons with the lasing wavelength are emitted in all directions through spontaneous emission. Since only the photons that align with the propagating direction can stay within the cavity, when population inversion is achieved, stimulated emission triggers a large number of coherent photons in this direction, resulting in an intense laser beam. In practice, one of the mirrors should be partially reflective such that the beam can exit the

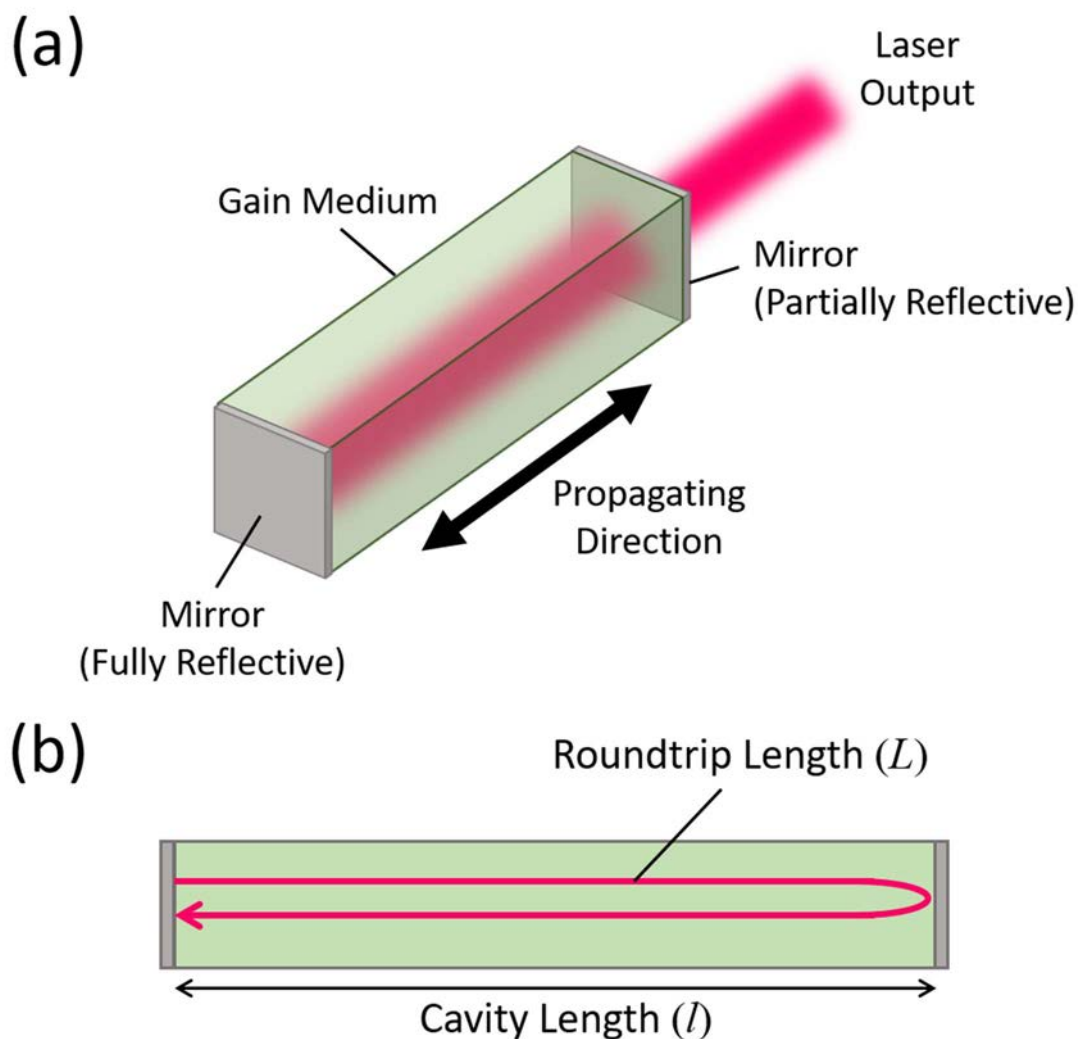


**Figure 1.8** (a) Simple Fabry-Pérot Laser Cavity and (b) its 2-D side-view schematic.

cavity as the laser output. Furthermore, the cavity length  $l$  should be chosen in the design such that there is an optical mode at the desired operating wavelength. For the Fabry-Pérot cavity in our example, if we consider simple plane wave propagation inside the cavity, the roundtrip length  $L = 2l$  should be a multiple of the wavelength inside the gain medium to support the Fabry-Pérot mode, where constructive interference is achieved after light propagates for every roundtrip and returns to the initial position (Figure 1.8b). Mathematically, we can write



$$L = 2l = \frac{m\lambda_0}{n}, \quad (1.33)$$

where  $n$  and  $\lambda_0$  are the refractive index of the gain medium and the vacuum wavelength, respectively.  $m$  is the mode order of the cavity, which is a positive integer. When an optical mode is excited, the number of aligned photons can be built up quickly without loss due to destructive interference. Cavities of other shapes may involve more complicated mathematics, but all of them depend on optical mode excitation to achieve lasing.

There are a few commonly used parameters in lasing mode analysis, both theoretically and experimentally, to indicate the waveguiding performances of an optical mode to support lasing. To begin with, the loss of an optical mode can be measured by the effective absorption coefficient  $\alpha_{\text{eff}}$ , which represents the decay of the modal optical energy according to the factor of  $\exp(-\alpha_{\text{eff}}z)$  as propagation takes place in the  $z$ -direction. On the other hand, pumping the gain material yields a certain amount of optical gain  $G$ , which counteracts the optical loss in the system by a factor of  $\exp(Gz)$ . To overcome the loss and achieve population inversion,  $G$  should be greater than or equal to  $\alpha_{\text{eff}}$ , meaning that the minimum optical gain required for lasing (i.e. threshold gain) is given by

$$G_{\text{th}} = \frac{\alpha_{\text{eff}}}{\Gamma}, \quad (1.34)$$

where  $\Gamma$  is the confinement factor (i.e. fractional energy in the gain medium of a given mode), which can be calculated by numerical integration over the solved modal field energy distribution. In the theoretical part of this work, it is assumed that the reflectivity



of any reflector is 100%, such that no light is lost at the reflectors and  $\alpha_{\text{eff}}$  only depends on the optical loss due to absorption and scattering by material inside the cavity. Furthermore, we can interpret the performance of a lasing mode by quality factor  $Q$ , which is broadly defined as [8]

$$Q = 2\pi \times \frac{\text{Energy stored}}{\text{Energy lost in one cycle of oscillation}}. \quad (1.35)$$

From this definition,  $Q$  of a lasing mode can be expressed in terms of common parameters in laser physics, such as

$$Q = \frac{\lambda_0}{\Delta\lambda_0}, \quad (1.36)$$

where  $\Delta\lambda_0$  is the full-width at half-maximum (FWHM) of the lasing peak in the wavelength spectrum. This is commonly used when measuring  $Q$  experimentally. For theoretical analysis,  $Q$  is calculated with different methods depending on the cavity structure and the mathematical model used, but they are all based on its definition stated in Equation (1.35). More details concerning parameter calculation, both theoretically and experimentally, would be discussed in the following chapters.

## 1.5. Upconversion Laser

For maximum efficiency, the gain material in the laser is usually optically excited with a pump light source of shorter wavelength (i.e. higher photon energy) than the peak gain wavelength of the material. This is a one-to-one process, in which each pump photon excites an atom (or a molecule) of the gain material, and the atom ends up at the upper lasing level. Such a process is called downconversion. If we take a three-level laser system as an example, as shown in Figure 1.9a, it can be seen that the gain

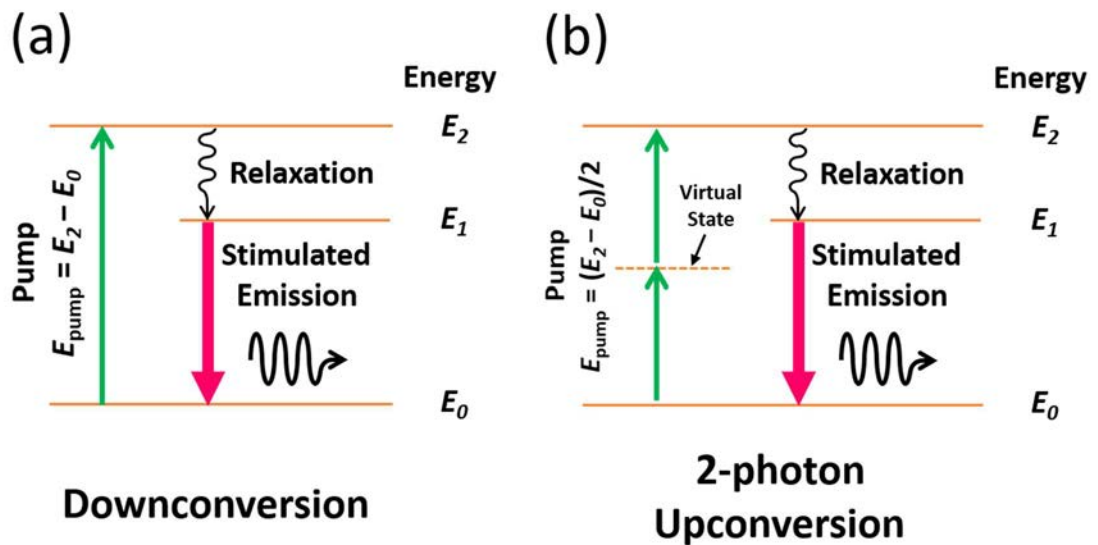


**Figure 1.9 Principle of (a) downconversion and (b) 2-photon upconversion lasers.** material absorbs pumping photons of energy  $(E_2 - E_0)$ , which is the bandgap between the meta-stable state and the ground level (non-radiative de-excitation is neglected.). In this case, one pumping photon is capable of exciting one of the gain material species from energy level  $E_0$  to  $E_2$ . However, it is also possible to achieve the same excitation through pump photons with energy  $(E_2 - E_0)/2$ , in which two photons are required. This process is called 2-photon upconversion, which is illustrated in Figure 1.9b. In general,  $n$ -photon upconversion is possible when  $n$  photons with pump photon energy  $E_{\text{pump}} = (E_2 - E_0)/n$  excites one atom or molecule simultaneously. Upconversion occurs at a much lower rate than downconversion, hence lasers excited through this mechanism has a much higher lasing threshold. Nevertheless, upconversion lasers can be useful in converting photons of lower energy into higher ones, allowing the laser to find more applications. For instance, upconversion lasers excited by infra-red photons and emitting visible light can be used in non-invasive tumor imaging and treatment [9].



## 1.6. Contribution of the Thesis

This thesis demonstrates how plasmonic upconversion lasers can be tuned to give different lasing characteristics, especially the reduction of optical loss. The main contribution include

- 1) demonstration of high-quality single- and multi-mode lasing in halide perovskite micro-lasers via multiphoton excitation. (Chapter 4, see Ref. [10])
- 2) demonstration of emission enhancement and lasing threshold reduction of lanthanide-doped  $\text{NaYF}_4$  hexagonal micro-rod lasers through plasmonic effect. (Chapter 5, see Ref. [11])

Other contribution include

- 1) theoretical optimization of Fabry-Pérot modes in rectangular plasmonic slot GaN lasers by Reflection Pole Method (RPM) (Chapter 2)
- 2) demonstration of high tunability of lasing characteristics in whispering-gallery modes (WGMs) of radially-layered cylindrical lasers. (Chapter 2)

## 1.7. Conclusion

Waveguides can act as lasers when their structures support the feedback of stimulated emission, which is triggered by pumping of a gain medium to achieve population inversion. To enhance the performance of a laser, plasmonic effect can be introduced to a laser to achieve subwavelength confinement of light. Moreover, multiphoton pumping (i.e. upconversion) of the gain medium allows lasers to find more applications by having a pump wavelength much longer than the emission wavelength. These two areas would be discussed extensively in the following chapters.





## 2. Theoretical Analysis of Cavity Modes

A laser cavity design can be optimized with the help of theoretical mode analysis. It determines how well each of the optical modes supported in a laser cavity is performing, indicated by various parameters as figures of merit. In this chapter, a few common metallic waveguide structures will be considered for more in-depth mode analysis.

### 2.1. Two-layer Planar Slab Waveguide

Since our work focuses on metallic waveguides, a two-layer planar slab structure refers to a metal-dielectric interface, in which the mathematical derivation for mode analysis is already discussed extensively in Chapter 1 as an example. In this section, we will make use of the previous results to analyze the surface plasmon modes (i.e. bound modes) at a single dielectric-metal interface.

We first consider the aforementioned air-metal structure again with  $\epsilon_{\text{rd}} = 1$ ,  $\epsilon_{\text{rm}} = 1 - \frac{\omega_p^2}{\omega^2}$  and  $\omega_p = 1.5 \times 10^{16} \text{ rad s}^{-1}$ . Three different frequency values,  $\omega = 0.3 \times 10^{16}$ ,  $0.5 \times 10^{16}$  and  $0.9 \times 10^{16} \text{ rad s}^{-1}$  (corresponding to wavelengths  $\lambda \approx 628, 377$  and  $209 \text{ nm}$  respectively), were chosen for bound mode analysis. The intensity distribution of the propagating optical energy (i.e. magnitude distribution of the  $z$ -component of the Poynting vector  $|S_z|$ ) for each of the frequency values, is plotted in Figure 2.1b, corresponding to purely real propagation constants of  $\beta_1$ ,  $\beta_2$  and  $\beta_3$  as indicated on the dispersion curve plotted in Figure 2.1a. Within the bound mode frequency range ( $\omega < \omega_{\text{sp}}$ ), it can be seen that  $\beta$  increases as  $\omega$  with  $\beta_1 < \beta_2 < \beta_3$ . As a result, light

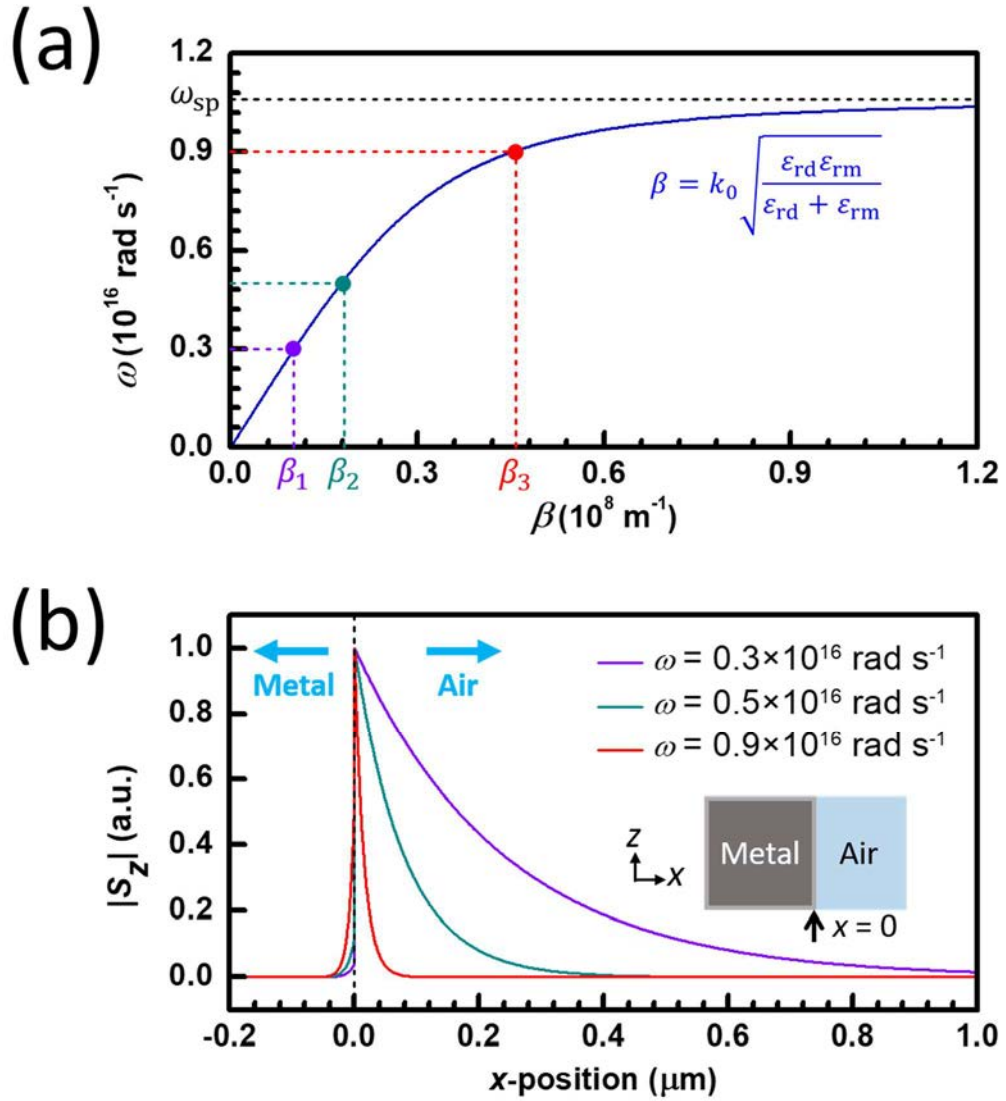


**Figure 2.1** (a) Dispersion relation of bound modes in an air-metal interface using the simple Drude model ( $\omega_p = 1.5 \times 10^{16} \text{ rad s}^{-1}$ ) and (b) the  $|S_z|$  distributions of bound modes at different frequencies.

becomes more confined at the interface located at  $x = 0$  with a greater fraction of the light confined at the metallic layer. There exists a surface plasmon frequency  $\omega_{sp}$  such that  $\beta \rightarrow \infty$  as  $\omega \rightarrow \omega_{sp}$ , which is given by

$$\epsilon_{rd} = -\epsilon_{rm} = -1 + \frac{\omega_p^2}{\omega_{sp}^2} \Rightarrow \omega_{sp} = \frac{\omega_p}{\sqrt{1 + \epsilon_{rd}}}. \quad (2.1)$$

The results shown in Figure 2.1 are based on the simple Drude model, which neglects any damping effect in the metallic layer and infinite degree of optical confinement without loss can be achieved. However, in practice, this phenomenon would be impossible. We can illustrate this by considering  $\epsilon_{\text{m}}$  as a complex number, in which the imaginary part represents the relaxation effects in the metal. To achieve this, a factor can be added to the simple Drude model to represent the relaxation behavior due to electron collisions, resulting in [6]

$$\epsilon_{\text{m}} = 1 - \frac{\omega_{\text{p}}^2}{\omega^2 - j\gamma\omega}, \quad (2.2)$$

where  $\gamma$  is the collision frequency. Although Equation (2.2) does not consider damping due to interband transitions, it would be sufficient to demonstrate the effect of metal relaxation on  $\beta$ . Using this modified Drude model with  $\gamma = 5 \times 10^{14}$  Hz, the dispersion curve of the air-metal interface was plotted again in Figure 2.2, which clearly shows that  $\beta$  is always finite. Furthermore,  $\beta$  is no longer purely real in the region  $\omega < \omega_{\text{sp}}$ , in which  $\text{Im}(\beta)$  represents the field decay because of the  $\exp(-j\beta z)$  field dependence upon propagation. As  $\text{Re}(\beta)$  approaches its maximum near  $\omega = \omega_{\text{sp}}$ ,  $|\text{Im}(\beta)|$  rises rapidly, showing that a bound mode with strong confinement is associated with large optical loss due to increased involvement of the metallic layer (hence increased metallic absorption of light). Therefore, there is often a trade-off between confinement strength and lasing threshold in real plasmonic laser design. A balance between the two should be made for optimal performance.

From the above results concerning the bound modes of an air-metal interface, a simple Drude model effectively predicts the dispersion relation even when the metal is

considered as a lossless medium for simplicity. However, in practice, one should note that the degree of confinement is usually enhanced at the cost of increased optical loss, which can be visualized by modeling the metal as a lossy material with a slight modification of the simple Drude model.

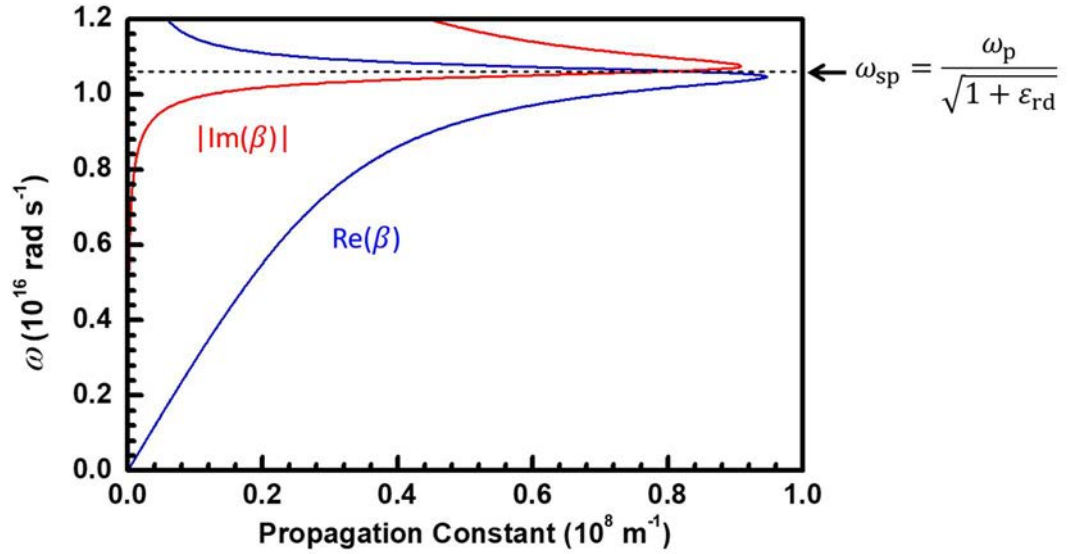


**Figure 2.2** Dispersion relation of an air-metal interface using a modified Drude model with electron collision damping

## 2.2. Three-layer Planar Slab Waveguide

After studying the modal characteristics of a single air-metal interface, we now move on to analyze waveguides that are more complicated. In this section, we would focus on the three-layer planar structure. For plasmonic waveguides, IMI (insulator-metal-insulator) or MIM (metal-insulator-metal) configuration are common structures that can be taken as examples. Both of them involve two dielectric-metal interfaces that interact with each other.

Before the optical modes can be found and analyzed, the dispersion relation of

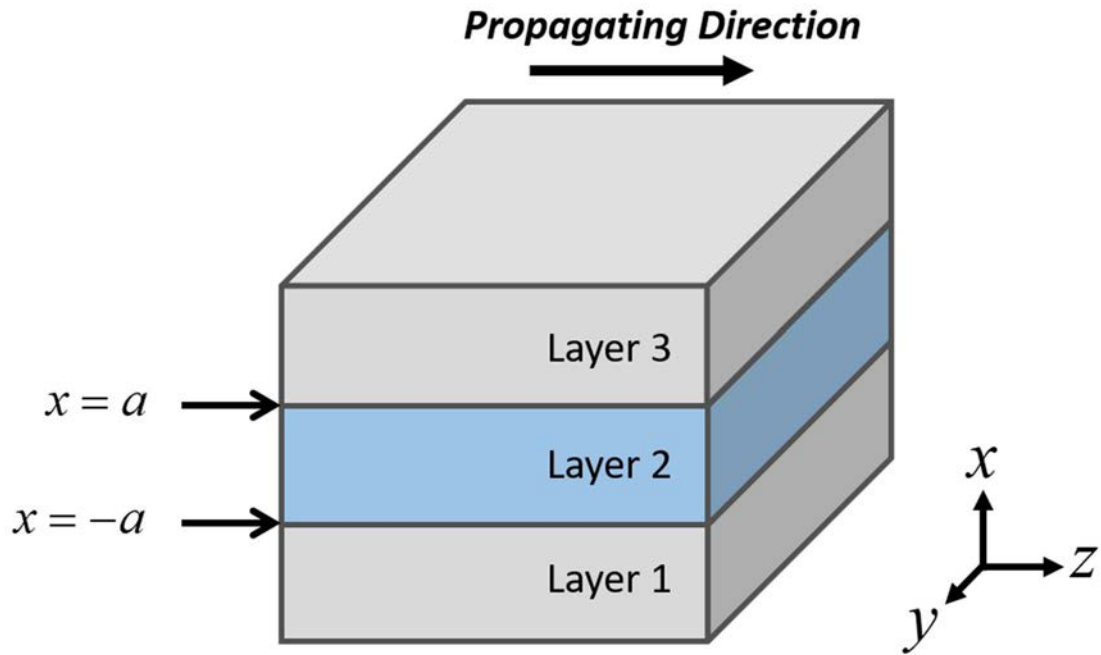


**Figure 2.3 Three-layer planar slab waveguide.**

the three-layer system has to be deduced. To achieve this, a schematic diagram is drawn in Figure 2.3 for mathematical derivation. The structure includes Layer 2 with a finite thickness  $2a$  along the  $x$ -direction sandwiched between two semi-infinite end layers (Layers 1 and 3). According to the figure, one can describe the field components using techniques similar to the previous case with the two-layer system, such that it decays outward exponentially along the  $x$ -direction at the end layers. As for Layer 2, the field should involve both forward and backward wave components propagating along and against the  $x$ -direction respectively. By considering  $t = 0$  in the harmonic term  $\exp(j\omega t)$  at position  $z = 0$ , the field components of TM modes can be expressed as

$$H_{y1} = A \exp(k_{x1}x) \quad (2.3)$$

$$E_{x1} = -A \frac{\beta}{\omega \epsilon_0 \epsilon_{r1}} \exp(k_{x1}x) \quad (2.4)$$



$$E_{z1} = jA \frac{k_{x1}}{\omega \epsilon_0 \epsilon_{r1}} \exp(k_{x1}x) \quad (2.5)$$

for Layer 1,

$$H_{y2} = B \exp(k_{x2}x) + C \exp(-k_{x2}x) \quad (2.6)$$

$$E_{x2} = -B \frac{\beta}{\omega \epsilon_0 \epsilon_{r2}} \exp(k_{x2}x) - C \frac{\beta}{\omega \epsilon_0 \epsilon_{r2}} \exp(-k_{x2}x) \quad (2.7)$$

$$E_{z2} = jB \frac{k_{x2}}{\omega \epsilon_0 \epsilon_{r2}} \exp(k_{x2}x) - jC \frac{k_{x2}}{\omega \epsilon_0 \epsilon_{r2}} \exp(-k_{x2}x) \quad (2.8)$$

for Layer 2 and

$$H_{y3} = D \exp(-k_{x3}x) \quad (2.9)$$

$$E_{x3} = -D \frac{\beta}{\omega \epsilon_0 \epsilon_{r3}} \exp(-k_{x3}x) \quad (2.10)$$

$$E_{z3} = -jD \frac{k_{x3}}{\omega \epsilon_0 \epsilon_{r3}} \exp(-k_{x3}x) \quad (2.11)$$

for Layer 3, where  $k_{xi}^2 = \beta^2 - k_0^2 \epsilon_{ri}$  ( $i = 1, 2, 3$ ) and  $A$ ,  $B$ ,  $C$ , and  $D$  are amplitude coefficients. The field components also have to satisfy the boundary conditions

$$A \exp(-k_{x1}a) = B \exp(-k_{x2}a) + C \exp(k_{x2}a) \quad (2.12)$$

$$A \frac{k_{x1}}{\epsilon_{r1}} \exp(-k_{x1}a) = B \frac{k_{x2}}{\epsilon_{r2}} \exp(-k_{x2}a) - C \frac{k_{x2}}{\epsilon_{r2}} \exp(k_{x2}a) \quad (2.13)$$

at  $x = -a$  and

$$D \exp(-k_{x3}a) = B \exp(k_{x2}a) + C \exp(-k_{x2}a) \quad (2.14)$$

$$D \frac{k_{x3}}{\varepsilon_{r3}} \exp(-k_{x3}a) = -B \frac{k_{x2}}{\varepsilon_{r2}} \exp(k_{x2}a) + C \frac{k_{x2}}{\varepsilon_{r2}} \exp(-k_{x2}a) \quad (2.15)$$

at  $x = a$ . Combining Equations (2.12) to (2.15), we have the dispersion relation

$$\exp(-4k_{x2}a) = \frac{\left(\frac{k_{x2}}{\varepsilon_{r2}} + \frac{k_{x1}}{\varepsilon_{r1}}\right)\left(\frac{k_{x2}}{\varepsilon_{r2}} + \frac{k_{x3}}{\varepsilon_{r3}}\right)}{\left(\frac{k_{x2}}{\varepsilon_{r2}} - \frac{k_{x1}}{\varepsilon_{r1}}\right)\left(\frac{k_{x2}}{\varepsilon_{r2}} - \frac{k_{x3}}{\varepsilon_{r3}}\right)}. \quad (2.16)$$

Note that when  $a \rightarrow \infty$ , Equation (2.16) reduces to  $\varepsilon_{r2}k_{x1} = -\varepsilon_{r1}k_{x2}$  or  $\varepsilon_{r2}k_{x3} = -\varepsilon_{r3}k_{x2}$ , which corresponds to the dispersion relation of the single dielectric-metal interfaces deduced previously in Equations (1.28) and (1.29). This matches with our expectation that the interaction between the SP at two dielectric-metal interfaces that are separated far apart is negligible. As for the case that  $a$  is finite, further simplification of the problem can be done by considering Layer 1 and Layer 2 being identical (i.e.  $\varepsilon_{r1} = \varepsilon_{r3}$  and  $k_{x1} = k_{x3}$ ). In this case, (2.16) can be separated into the following two equations:

$$\exp(-2k_{x2}a) = \frac{\frac{k_{x2}}{\varepsilon_{r2}} + \frac{k_{x1}}{\varepsilon_{r1}}}{\frac{k_{x2}}{\varepsilon_{r2}} - \frac{k_{x1}}{\varepsilon_{r1}}} \Rightarrow \tanh(k_{x2}a) = -\frac{k_{x1}\varepsilon_{r2}}{k_{x2}\varepsilon_{r1}} \quad (2.17)$$

$$\exp(-2k_{x2}a) = -\frac{\frac{k_{x2}}{\varepsilon_{r2}} + \frac{k_{x1}}{\varepsilon_{r1}}}{\frac{k_{x2}}{\varepsilon_{r2}} - \frac{k_{x1}}{\varepsilon_{r1}}} \Rightarrow \tanh(k_{x2}a) = -\frac{k_{x2}\varepsilon_{r1}}{k_{x1}\varepsilon_{r2}}. \quad (2.18)$$

By putting (2.17) back into (2.12) and (2.13), it can be seen that (2.17) represents modes with  $B = C$  and  $A = D$ , in which  $H_y$  and  $E_x$  are even functions and  $E_z$  is an odd function in  $x$  (i.e. odd parity). Similarly, it can be proven that (2.18) corresponds to the case with  $B = -C$  and  $A = -D$ , such that  $H_y$  and  $E_x$  are odd functions and  $E_z$  is an even function

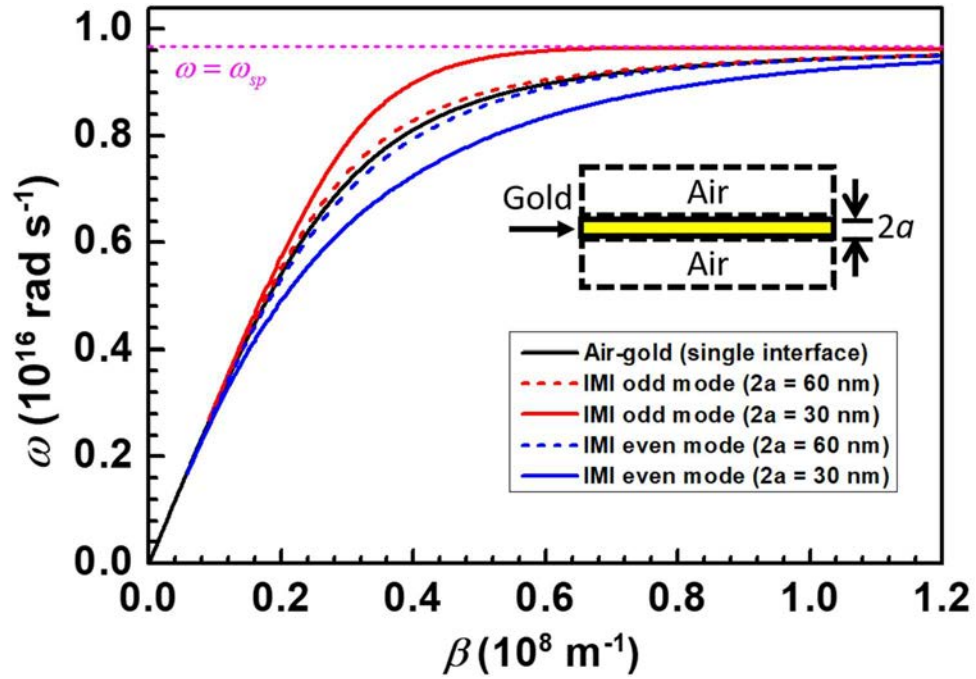


**Figure 2.4** Dispersion relation of odd and even modes of IMI (air-gold-air) system with gold thicknesses  $2a = 30$  nm and  $2a = 60$  nm.

in  $x$  (i.e. even parity). As a result, the modes represented by (2.17) and (2.18) are called odd modes and even modes respectively.

Here, we consider the IMI system with gold ( $\omega_p = 1.3687 \times 10^{16}$  rad s<sup>-1</sup>) and air under the simple Drude model. The dispersion relations of the system with gold thickness  $2a = 30$  nm and  $2a = 60$  nm, are plotted in Figure 2.4. The result shows that the dispersion curve in each of the two cases splits into two, corresponding to the odd modes and even modes. It can be seen that the dispersion curve of odd (even) mode shifts upward (downward) from that of the air-gold single interface, indicating that SP propagating in multiple air-gold interfaces would interact with each other to give a modification to the resulting plasmonic modes. It is within our expectation that a thicker gold layer (i.e. larger value of  $2a$ ) in the IMI system results in less SP interaction and dispersion curve shift, as the two air-gold interfaces are separated further apart. In addition, for any gold thickness, as the propagation constant  $\beta \rightarrow \infty$ , we have  $k_{xi} \rightarrow \beta$



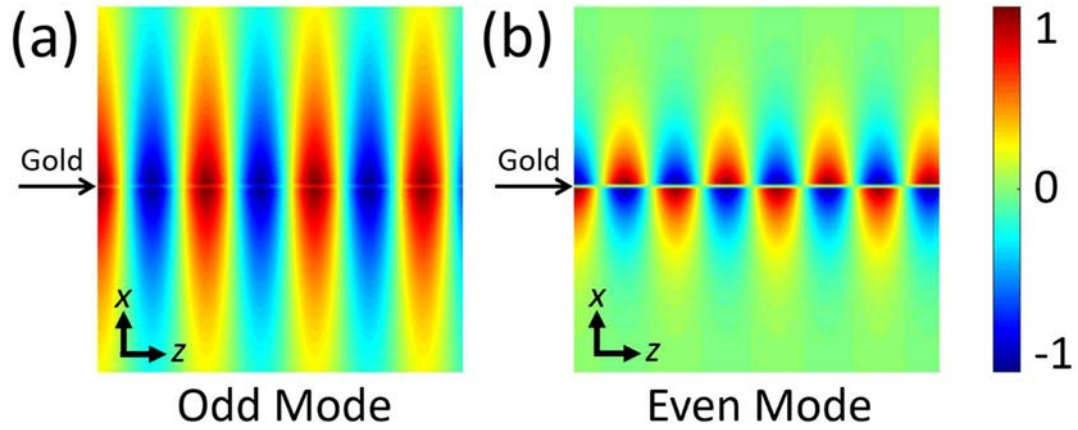


**Figure 2.5** Magnetic field ( $H_y$ ) distribution of the (a) odd mode and (b) even mode supported by the IMI (air-gold-air) system on the  $xz$ -plane over a  $2\ \mu\text{m} \times 2\ \mu\text{m}$  area, with gold thickness  $2a = 30\ \text{nm}$  and wavelength  $\lambda = 600\ \text{nm}$  (i.e.  $\omega \approx 3.14 \times 10^{15}\ \text{rad s}^{-1}$ ). The gold layer is assumed to be lossless, following the simple Drude model.

since  $k_{xi}^2 = \beta^2 - k_0^2 \epsilon_{ri}$  ( $i = 1, 2$ ). By putting  $k_{xi} = \beta$  into Equations (2.17) and (2.18), we have

$$\omega_{\pm} \approx \frac{\omega_p}{\sqrt{1 + \epsilon_1}} \sqrt{1 \pm \frac{2\epsilon_1 e^{-2\beta a}}{1 + \epsilon_1}} = \omega_{sp} \sqrt{1 \pm \frac{2\epsilon_1 e^{-2\beta a}}{1 + \epsilon_1}}, \quad (2.19)$$

where  $\omega_+$  and  $\omega_-$  are the angular frequencies of the odd and even modes respectively. According to this equation,  $\omega_+$  and  $\omega_-$  approaches to  $\omega_{sp}$  from above and below respectively, as  $\beta \rightarrow \infty$ . To visualize the odd and even modes, their magnetic field ( $H_y$ ) distributions on the  $xz$ -plane is plotted according to the field expressions (2.3), (2.6) and (2.9) for  $2a = 30\ \text{nm}$  and wavelength  $\lambda = 600\ \text{nm}$ . The results are presented in Figure 2.5, which agree with the fact that  $H_y$  is an even (odd) function for the odd (even) modes. Furthermore, it can be seen that the field of the even modes is more confined than the odd modes, which matches with the fact (from Figure 2.4) that for the same value of  $\omega$ ,  $\beta$  of the even mode is always larger than that of the odd modes. It is also worthy to note

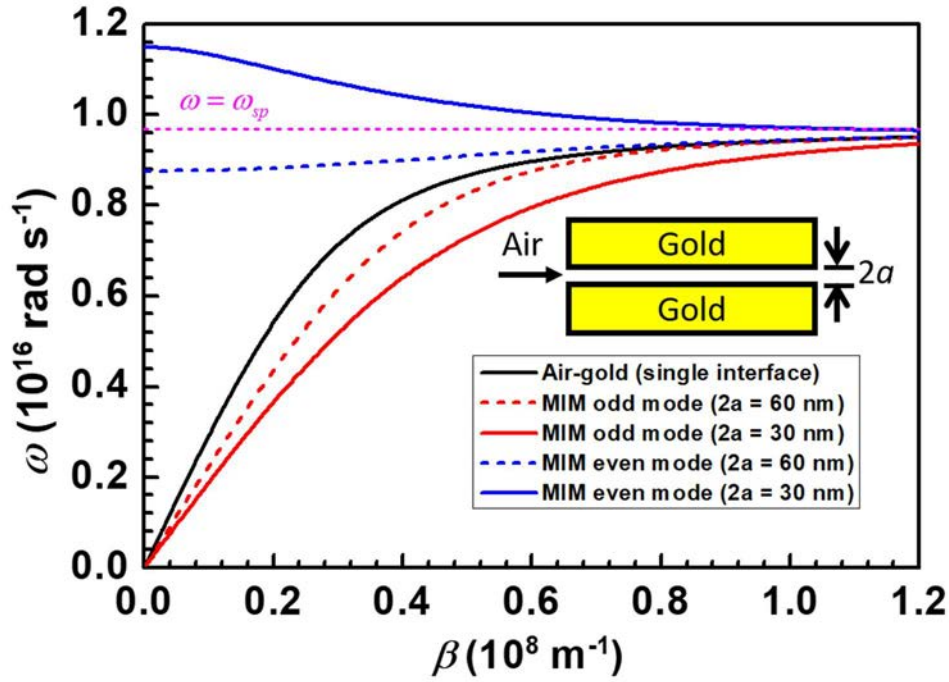


**Figure 2.6** Dispersion relation of odd and even modes of MIM (gold-air-gold) system with air gap thicknesses  $2a = 30$  nm and  $2a = 60$  nm.

that a small value of  $2a$  actually shifts the dispersion curve of the odd modes closer to the light line  $\omega = ck$ , because high degree of light confinement within two close air-gold interfaces is less favourable in this case, and the light wave tends to behave like typical plane waves travelling in a homogeneous dielectric. This can also be observed in Figure 2.5a, where light propagation depends less on SP propagation, resulting in less degree of light confinement along the  $x$ -direction.

For the gold-air-gold MIM system, the dispersion relations of the odd and even modes are also different from that of the single air-gold interface, as shown in Figure 2.6. Similar to the previous case with the IMI system, a larger value of  $2a$  in the MIM system separates the two air-gold interfaces further apart, resulting in less interaction between them, as well as a dispersion curve closer to that of a single air-gold interface. However, in the case of the MIM system,  $2a$  refers to the air gap thickness between the

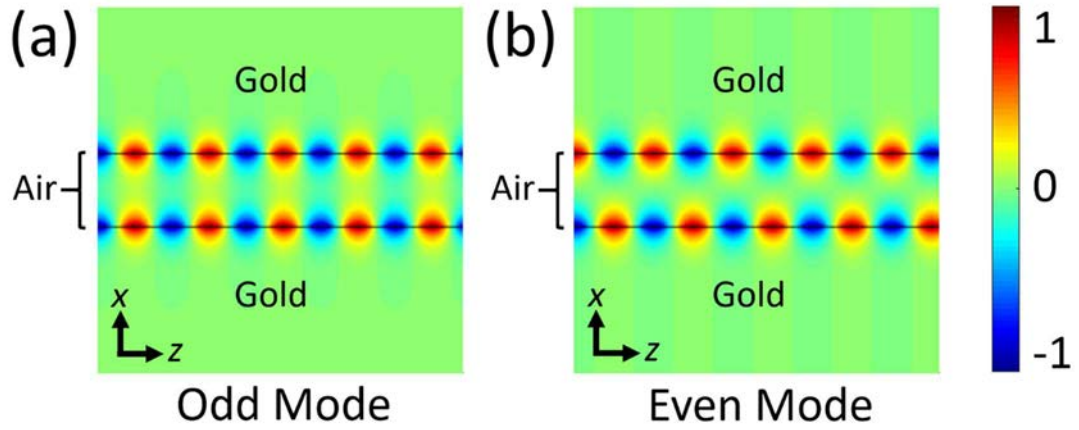


**Figure 2.7** Magnetic field ( $H_y$ ) distribution of the (a) odd mode and (b) even mode supported by the MIM (gold-air-gold) system on the  $xz$ -plane over a  $0.3 \mu\text{m} \times 0.3 \mu\text{m}$  area, with air gap thickness  $2a = 60 \text{ nm}$  and wavelength  $\lambda = 200 \text{ nm}$  (i.e.  $\omega \approx 9.42 \times 10^{15} \text{ rad s}^{-1}$ ). The gold layer is assumed to be lossless, following the simple Drude model.

two gold layers instead. In addition, regardless of the air gap thickness, the dispersion curve of the odd modes and even modes respectively approaches to the line  $\omega = \omega_{\text{sp}}$  from below and above when  $\beta \rightarrow \infty$ , because one can derive another relation similar to (2.19), that

$$\omega_{\pm} \approx \frac{\omega_p}{\sqrt{1 + \epsilon_2}} \sqrt{1 \mp \frac{2\epsilon_2 e^{-2\beta a}}{1 + \epsilon_2}} = \omega_{\text{sp}} \sqrt{1 \mp \frac{2\epsilon_2 e^{-2\beta a}}{1 + \epsilon_2}}. \quad (2.20)$$

The shapes of the dispersion curves for the MIM system are very different from those of the IMI one. First, for the odd modes, the initial slope at  $\omega = 0$  depends on  $2a$ , and is different from that of the single air-gold interface. Second, for the even modes, the dispersion curve does not pass through the origin. These properties can be attributed to the thin and finite air gap of the MIM system, in contrast to the semi-infinite air regions available in the IMI system for plane-wave-like propagation at low frequencies. The magnetic field distributions of the odd and even modes in the MIM system ( $2a = 60 \text{ nm}$ )



at wavelength  $\lambda = 200$  nm are plotted in Figure 2.7. Again,  $H_y$  is found to be an even and an odd function for the odd and even mode, respectively. Moreover, since the odd mode has larger  $\beta$  than the even mode, as presented in Figure 2.6, it packs a higher number of wavelengths within 300 nm along the  $z$ -direction.

By studying simple symmetric IMI and MIM systems, it can be seen that when multiple dielectric-metal interfaces exist in a structure, its modal behavior would be very different from that of a system with only one interface. A smaller distance between the SP sites results in stronger interaction.

### 2.3. Reflection Pole Method for Multi-layer Slab Waveguide

In the previous section, optical modes of simple planar waveguides can be found directly by plotting the dispersion curve. However, for more complicated planar structures with more layers, solving for the modes can be numerically challenging. In this case, it is more convenient to use the reflection pole method (RPM) [12] to find the supported optical modes. This method involves expressing the boundary and initial conditions in matrix form, followed by solving the resonant condition for a single wavelength. In this section, the full mathematical derivation of such method, as well as its application in the analysis of a few waveguide examples, will be discussed.

To make our mathematical model more general, we suppose the planar waveguide to be studied has  $N$  layers (where  $N \geq 2$  is an integer), which are infinite over the  $yz$ -plane. In the  $x$ -direction, the end layers (Layer 1 and Layer  $N$ ) are assumed to be semi-infinite, while the other layers have finite thicknesses.  $x = 0$  is defined as the location of the first interface between Layer 1 and 2, as illustrated in Figure 2.8. In this case, for TM modes, we can describe the magnetic field  $H_y$  in each layer at time  $t = 0$  as

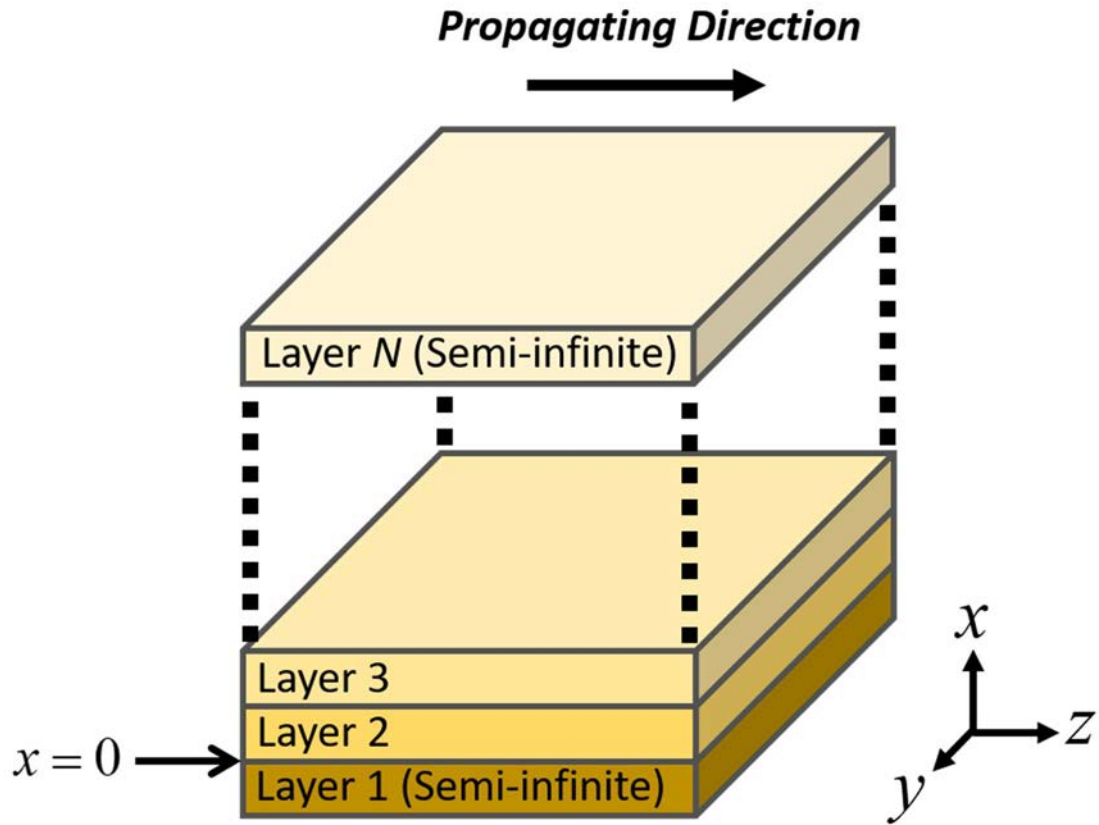


**Figure 2.8**  $N$ -layer planar slab waveguide.

$$H_{yi} = \{ A_i \exp[-k_{xi}(x - x_i)] + B_i \exp[k_{xi}(x - x_i)] \} \exp(-j\beta z), \quad (2.21)$$

where  $k_{xi}$  is the wave constant of the  $i$ -th layer ( $i = 1, 2, 3, \dots, N$ ) in the  $x$ -direction given by  $k_{xi}^2 = \beta^2 - k_0^2 \epsilon_{ri}$ , with  $\epsilon_{ri}$  being the relative permittivity of that layer.  $x_i$  is the  $x$ -position of the  $i$ -th boundary, and  $A_i$  and  $B_i$  are the amplitude coefficients. Similar to the formulation for the two- and three-layer planar systems, Equation (2.21) describes the forward and backward waves in each layer along the  $x$ -direction with light propagation along the  $z$ -direction. However, unlike the previous sections, for systems that may involve more than three layers, it is much more convenient to express  $H_{yi}$  in terms of  $x_i$  instead of omitting it, such that, as one would notice in the future steps of the



mathematical derivation, the resulting dispersion relation can be expressed in terms of the thickness of each layer easily. With  $H_y$  written for each layer as  $H_{yi}$ , the functions of adjacent layers can be related by the boundary conditions  $H_{yi} = H_{y,i+1}$ ,  $\epsilon_{ri} E_{xi} = \epsilon_{r,i+1} E_{x,i+1}$  and  $E_{zi} = E_{z,i+1}$  (see Equations (1.20) to (1.22) in Chapter 1). This leads to

$$\begin{bmatrix} A_i \\ B_i \end{bmatrix} = T_{i-1} \begin{bmatrix} A_{i-1} \\ B_{i-1} \end{bmatrix}, \quad (2.22)$$

where the matrix  $T_i$  can be defined as

$$T_i = \frac{1}{2} \begin{bmatrix} \left(1 + \frac{\epsilon_{r,i+1}}{\epsilon_{ri}} \frac{k_{xi}}{k_{x,i+1}}\right) \exp(-k_{xi} d_i) & \left(1 - \frac{\epsilon_{r,i+1}}{\epsilon_{ri}} \frac{k_{xi}}{k_{x,i+1}}\right) \exp(k_{xi} d_i) \\ \left(1 - \frac{\epsilon_{r,i+1}}{\epsilon_{ri}} \frac{k_{xi}}{k_{x,i+1}}\right) \exp(-k_{xi} d_i) & \left(1 + \frac{\epsilon_{r,i+1}}{\epsilon_{ri}} \frac{k_{xi}}{k_{x,i+1}}\right) \exp(k_{xi} d_i) \end{bmatrix}, \quad (2.23)$$

with  $d_i$  being the thickness of the  $i$ -th layer. Inductively, Equation (2.22) can be applied from  $i = N$  to  $i = 2$  to give

$$\begin{bmatrix} A_N \\ B_N \end{bmatrix} = T_{N-1} T_{N-2} \dots T_2 T_1 \begin{bmatrix} A_1 \\ B_1 \end{bmatrix} = \begin{bmatrix} t_{11} & t_{12} \\ t_{21} & t_{22} \end{bmatrix} \begin{bmatrix} A_1 \\ B_1 \end{bmatrix}. \quad (2.24)$$

During the optical excitation of the system, it can be assumed that light wave comes from the bottom of the system in Layer 1. Therefore, there should be no reflected backward wave along the  $x$ -direction in the  $N$ -th layer since no interface is located beyond  $x = x_{N-1}$ , this results in  $B_N = 0$ , so

$$\begin{bmatrix} A_N \\ 0 \end{bmatrix} = \begin{bmatrix} t_{11} & t_{12} \\ t_{21} & t_{22} \end{bmatrix} \begin{bmatrix} A_1 \\ B_1 \end{bmatrix}. \quad (2.25)$$

As a result, when the system is in resonance, we have

$$\text{Reflectance } (R) = \frac{B_1}{A_1} = -\frac{t_{21}}{t_{22}} = \infty \Rightarrow t_{22} = 0. \quad (2.26)$$

In RPM, Our main objective is to solve  $t_{22}(\beta) = 0$  (i.e. finding  $\beta$  of the optical modes) mentioned in Equation (2.26), which is numerically challenging and computationally heavy. RPM is a method designed to solve complicated complex equations like this. In the method,  $\text{Im}(\beta)$  is fixed at 0, and the phase of  $t_{22}$  is monitored as  $\text{Re}(\beta)$  varies. Any sudden and rapid change in the phase of  $t_{22}$  that results in a symmetric pole (sharp peaks) in the phase derivative curve of  $t_{22}$  indicates the existence of a root of  $\beta$  with that particular real part. In this way, we can locate the approximate value of the real part of the root and hence narrow down the range for root searching by setting it as the initial value for computational techniques like Newton-Raphson Method. For enhanced readability and convenience of computation, we first express the propagation constant  $\beta$  as

$$\beta = k_0 n_{\text{eff}} = k_0 (n_r - jn_i), \quad (2.27)$$

where  $k_0$  is the (purely real) vacuum wavenumber and  $n_{\text{eff}} = n_r - jn_i$  is the complex effective refractive index (i.e. mode index), with  $n_r$  and  $n_i$  as the real and imaginary part indices respectively. In this case, we can vary  $n_r$  to monitor the phase of  $t_{22}$  ( $\phi$ ). To visualize the roots, one can plot the phase derivative  $d\phi/dn_r$  against  $n_r$ . After solving  $\beta$ , we can substitute it back to Equation (2.21) to find  $H_{yi}$  for each layer. The other two field components  $E_{xi}$  and  $E_{zi}$  can be deduced by

$$E_{xi} = -\frac{\beta}{\omega \epsilon_0 \epsilon_r} H_{yi} \quad (2.28)$$

$$E_{zi} = \frac{j}{\omega \epsilon_0 \epsilon_r} \frac{\delta H_{yi}}{\delta x}, \quad (2.29)$$

which are essentially the same as Equations (1.15) and (1.16) mentioned in Chapter 1. We further note that RPM also works for TE modes by replacing  $H_{yi}$  with  $E_{yi}$  in Equation (2.21) at the beginning of the mathematical derivation process. However, as discussed in Chapter 1, TE modes do not support SP, so they are not our focus.

In the following, we will verify our mathematical model by applying it to a gold-air-gold (MIM) system, and compare the results with that derived from the dispersion relation in the previous section. Figure 2.9 shows the dispersion curves of odd and even modes of the MIM system with air gap thickness  $2a = 100$  nm, according to the dispersion relation derived previously (Equation (2.16)). Two wavelengths,  $\lambda = 250$  nm and  $\lambda = 600$  nm, are nominated for the verification, their corresponding  $\omega$  values are marked as black horizontal dashed lines on the plot. By looking at the intersections between the black dashed lines and the dispersion curves, it can be seen clearly that both odd and even modes are supported at  $\lambda = 250$  nm, whereas only the odd mode is supported for  $\lambda = 600$  nm. Here, we try to apply RPM to the same waveguide system to see if the results are consistent with what is shown in Figure 2.9 for the two nominated wavelengths. To begin with, the phase derivative of  $t_{22}$  ( $d\phi/dn_r$ ) is plotted against  $n_r$  in Figure 2.10 for each of the nominated wavelengths. It is noted that the full-width at half-maximum (FWHM) of each of the poles in the plots is equal to  $|2n_i|$ . For this reason, a very small imaginary part  $\text{Im}(\epsilon_{r1}) = \text{Im}(\epsilon_{r3}) = -0.0001$  is given to the relative permittivity of gold used in RPM (instead of keeping it zero according to the simple Drude model), such that  $n_i \neq 0$  and  $\text{FWHM} > 0$  for the poles to become visible on the phase derivative plot, as presented in the figure. This modification will not have a



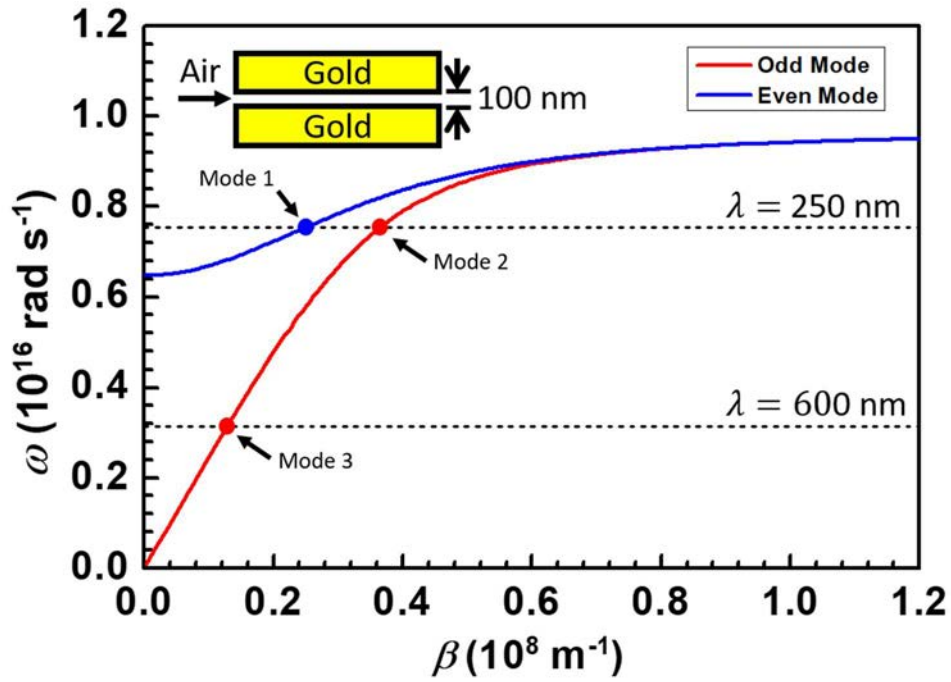


**Figure 2.9** Dispersion relation of 1-dimensional gold-air-gold (MIM) system with semi-infinite gold layers and air gap thickness  $2a = 100$  nm. The black dashed lines indicate both odd and even mode (Mode 1 & 2) exists at wavelength  $\lambda = 250$  nm, and only odd mode (Mode 3) exists at  $\lambda = 600$  nm.

noticeable impact on the value of  $n_r$ , see Table 1. With the poles become visible, Mode 1 to 3 are marked on Figure 2.10, with each pole corresponding to an optical mode. These modes are numbered corresponding to the intersection points marked on Figure 2.9. To confirm such a correspondence is valid,  $\beta$  of each mode solved from RPM is found by  $\beta = k_0 n_r$ , and is matched with the result according to Equation (2.16) using the Newton- Raphson Method. According to Table 1, the values of  $\beta$  of Mode 1 to 3 found by RPM matched with those by Equation (2.16) for up to 8 significant figures when  $\text{Im}(\varepsilon_{r1}) = \text{Im}(\varepsilon_{r3}) = -0.0001$  is applied, and up to 12 significant figures when  $\text{Im}(\varepsilon_{r1}) = \text{Im}(\varepsilon_{r3}) = 0$ . To further verify the results of RPM, the magnetic field ( $H_y$ ) distribution of the supported modes indicated on Figure 2.10 are presented in Figure 2.11, showing that the magnetic field of Mode 1 is an odd function in  $x$  (i.e. even mode)

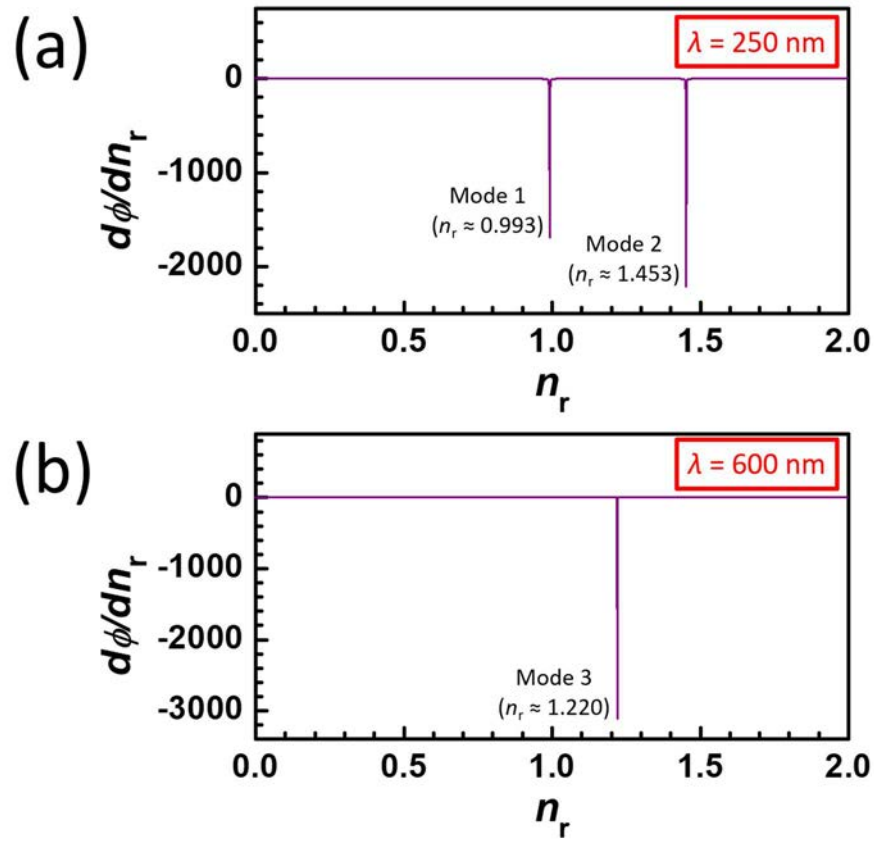


**Figure 2.10** Phase derivative of  $t_{22}$  ( $d\phi/dn_r$ ) against real part index ( $n_r$ ) of the gold-air-gold system (air gap thickness  $2a = 100$  nm) for (a)  $\lambda = 250$  nm and (b)  $\lambda = 600$  nm. The imaginary part index ( $n_i$ ) is set as zero. Simple Drude model is used to model the relative permittivity of gold, with  $-0.0001$  as the fixed imaginary part.

while that of Mode 2 and 3 are even functions in  $x$  (odd modes). Therefore, it is convincing to conclude that RPM essentially gives the same results as with the dispersion relation.

Solving the optical modes in terms of  $n_{\text{eff}}$  instead of finding  $\beta$  directly, is more intuitive. The group index  $n_r$  is analogous to the bulk material refractive index. It can be regarded as the “refractive index” of the optical mode in the propagating direction  $z$ . Using the  $n_r$  values from Figure 2.10, one can find that over a  $1\text{-}\mu\text{m}$   $z$ -distance, Mode 1, 2 and 3 should accommodate around 3.972, 5.812 and 2.033 wavelengths respectively (calculated by  $n_r L_z / \lambda$ , where  $L_z$  is the  $z$ -distance). This agrees with Figure 2.11.

**Table 1** Values of  $\beta$  ( $\times 10^8 \text{ m}^{-1}$ ) of Mode 1 to 3 of the gold-air-gold system ( $2a = 100 \text{ nm}$ ) deduced by RPM and by Equation (2.16) for  $\lambda = 250 \text{ nm}$  and  $\lambda = 600 \text{ nm}$ , up to 12 significant figures.

Mode	RPM ( $\text{Im}(\epsilon_{r1}) = -0.0001$ )	RPM ( $\text{Im}(\epsilon_{r1}) = 0$ )	Equation (2.16)
1 (Even Mode)	0.249253517896	0.249253518395	0.249253518395
2 (Odd Mode)	0.365102410514	0.365102410869	0.365102410869
3 (Odd Mode)	0.127803149056	0.127803149056	0.127803149056

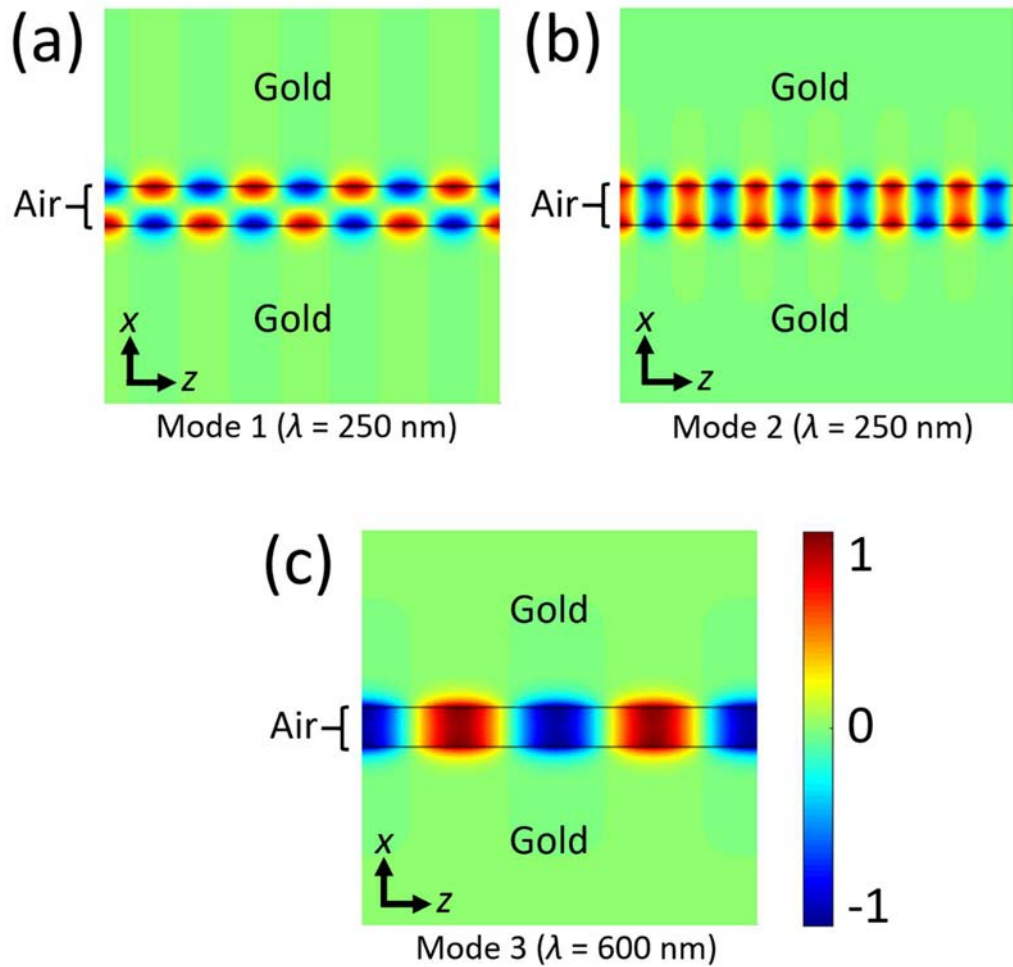


**Figure 2.11** Magnetic field ( $H_y$ ) distribution of Mode 1 to 3 supported by the MIM (gold-air-gold) system on the  $xz$ -plane, with air gap thickness  $2a = 100 \text{ nm}$ . The dimension of each of the plots is  $1 \mu\text{m} \times 1 \mu\text{m}$ , and  $\text{Im}(\epsilon_{r1}) = \text{Im}(\epsilon_{r3}) = -0.0001$ .

Despite RPM only solves the TM modes at one wavelength at a time, it is still very useful in the analysis of laser cavities. As mentioned in the previous chapter, a laser depends on a gain medium to enable stimulated emission of certain specific wavelengths, so the application of RPM on those specific wavelengths is often sufficient. There is no need to apply RPM over a large range of wavelengths. In the following, we would use RPM to predict the optical mode in a more realistic laser structure. The structure, which is shown in Figure 2.12a, is designed by Zhang et al. [13]. It includes a GaN triangular nano-rod as the gain medium, which is placed on an Al film with an 8-nm SiO<sub>2</sub> coating. Usually, it is challenging to perform theoretical analysis on a structure with such a complicated geometry using relatively simple methods like the RPM we have derived. Instead, finite-element method is commonly used to solve the modes, at the cost of a great amount of computational resource. However, by considering the middle part of the cross-section of the original design, a simplified structure with only planar slabs can be generated in order to apply RPM, see Figure 2.12b. Using RPM, it is found that the simplified structure has only one plasmonic mode, with the electric field strength ( $|E|$ ) distribution shown in Figure 2.12d. When comparing this result with Figure 2.12c, which is the  $|E|$  distribution of the original structure obtained by Zhang et al. with 3-D finite-element method, it can be observed that RPM effectively predicts the field distribution at the middle part of the cross-section of the original design. The noticeable difference of  $|E|$  between the two sets of result can be found at the GaN-air interface, which is due to the sharp edge of the triangular rod, compared to a flat GaN surface in the simplified structure. In general, many 2-D and 3-D structures with combinations of common shapes can be simplified into a 1-D planar structure for quick prediction of modal light distribution using RPM with reasonable accuracy.

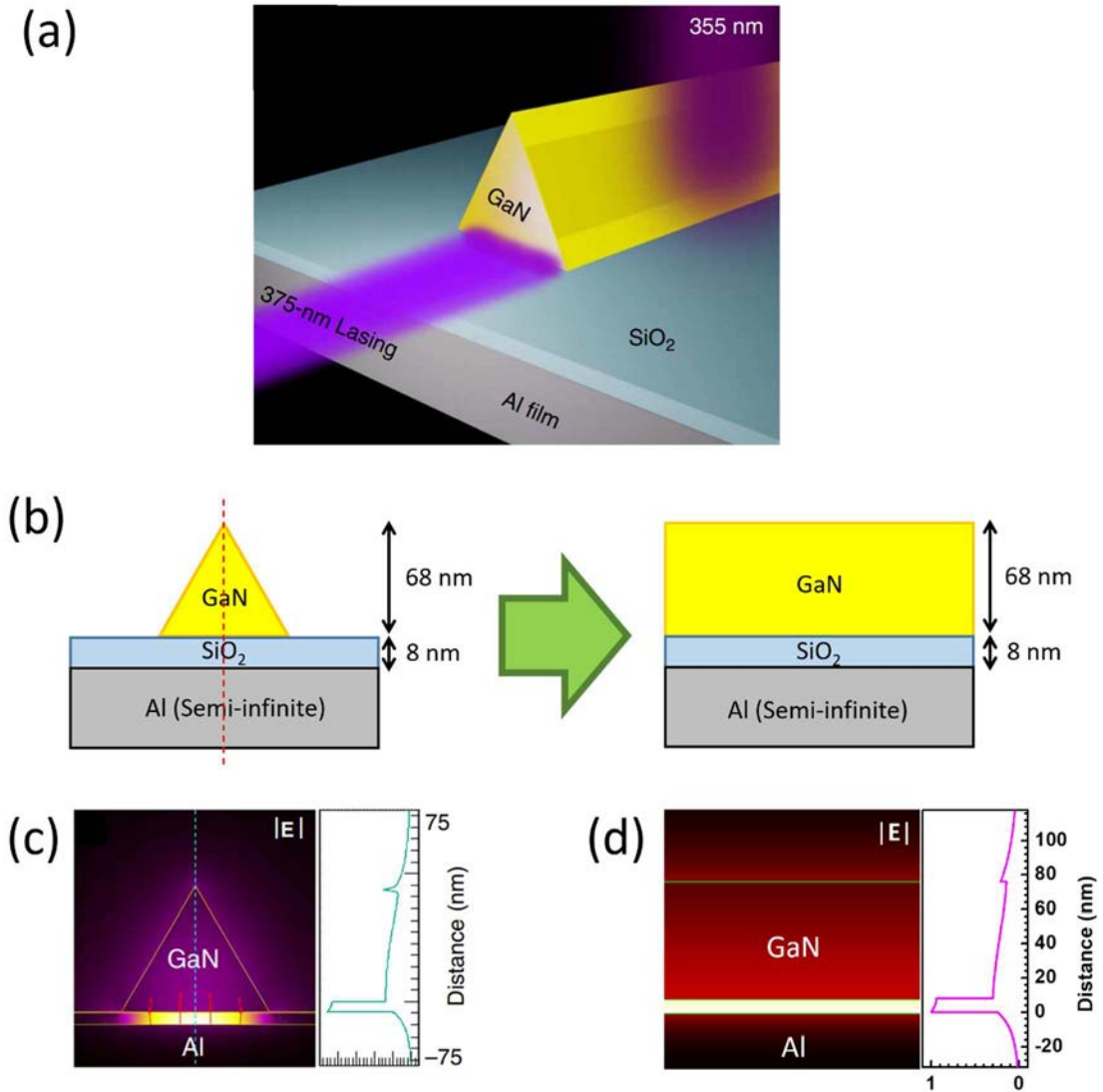
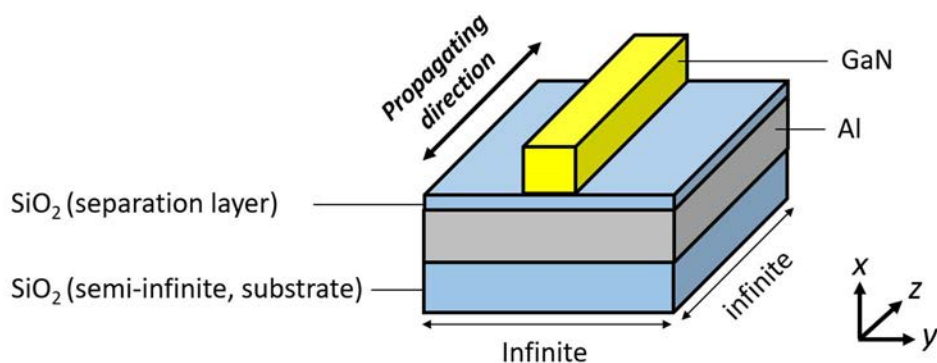


**Figure 2.12** (a) 3-D schematic of the GaN laser designed by Zhang et al. in Ref. [13], with a GaN triangular rod placed on a piece of SiO<sub>2</sub>-coated Al. (b) shows the cross-section of the simplified semi-infinite planar waveguide structure (right) considered for theoretical analysis by RPM, compared to that of the original structure (left). The simulation result by Zhang et al. [13] on the original structure is shown in (c), and that by RPM on the simplified planar structure is shown in (d). The material refractive indices used in RPM are the same as those used in Ref. [13].

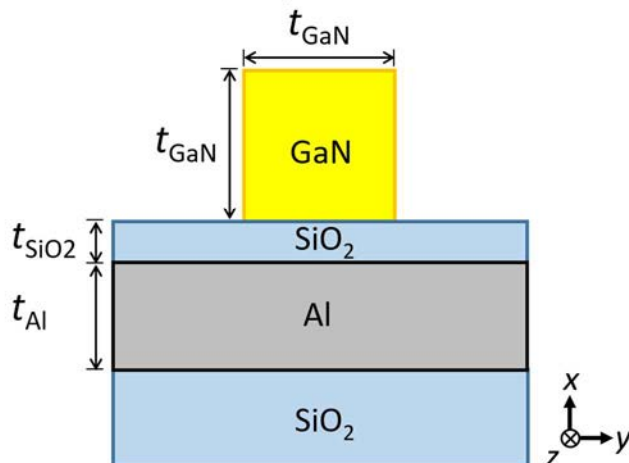
There are many well-known techniques and considerations regarding the design of a plasmonic laser. Here, with reference to the laser structure in Figure 2.12a, we will discuss some of the effects of material and dimension on the performance of a plasmonic laser. A structure similar to the one in Figure 2.12a is proposed as an example, which is shown in Figure 2.13. It is formed by a GaN rod placed on a SiO<sub>2</sub>-Al-

(a)



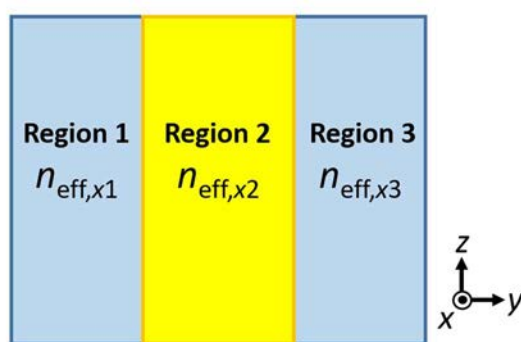
**Oblique View**

(b)



**Front View**

(c)



**Top View**

Figure 2.13 (a) Oblique, (b) front and (c) top view of the proposed GaN laser for 2-D RPM analysis.

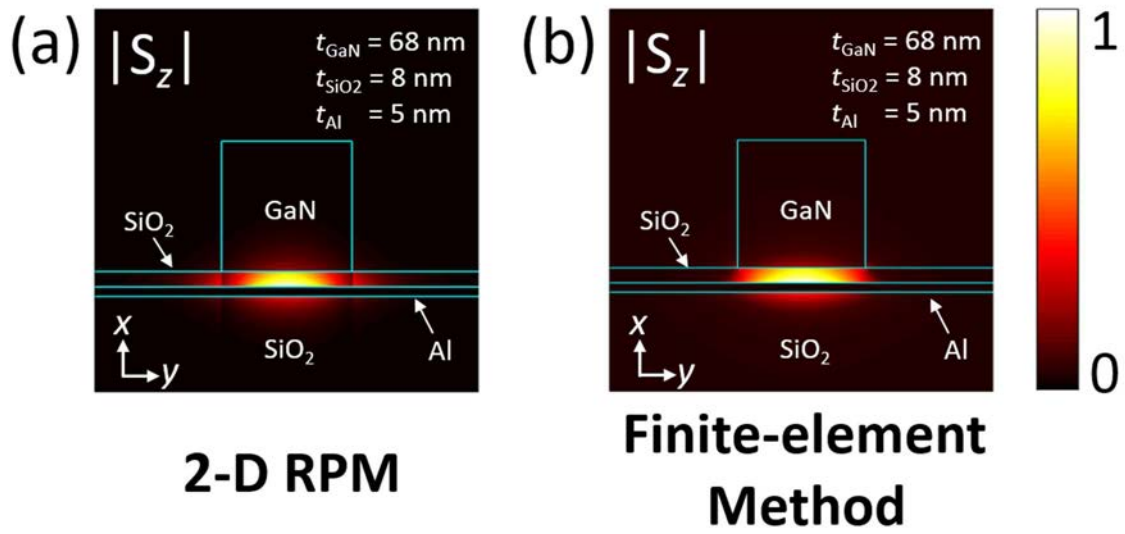


**Figure 2.14** Deduced modal  $|S_z|$  distribution of the planar plasmonic slot laser for  $t_{\text{GaN}} = 68 \text{ nm}$ ,  $t_{\text{SiO}_2} = 8 \text{ nm}$  and  $t_{\text{Al}} = 40 \text{ nm}$  using (a) 2-D RPM and (b) finite-element method (COMSOL Multiphysics 5.0).

SiO<sub>2</sub> slab system. Unlike the original design by Zhang et al., the Al layer is assumed to be grown on a semi-infinite SiO<sub>2</sub> substrate in the proposed system, such that it has finite thickness. In this case, the effect of the Al thickness on the laser performance can be studied as well. Moreover, the cross-section of the GaN rod is assumed to be square in shape, which facilitates 2-D analysis with RPM. The 2-D analysis is done by first applying the original 1-D RPM over Region 1 to 3 shown in Figure 2.13c along the  $x$ -direction to obtain the effective refractive index  $n_{\text{eff},xi}$  ( $i = 1,2,3$ ) for each region, followed by applying 1-D RPM for an additional time on a virtual 3-layer waveguide formed by virtual planar slabs with refractive indices equal to  $n_{\text{eff},x1}$ ,  $n_{\text{eff},x2}$  and  $n_{\text{eff},x3}$ , along the  $y$ -direction. The resulting 2-D modal field distribution of any point on the  $xy$ -plane is the product of the two normalized field strengths of that point solved in the  $x$ - and  $y$ -direction. Such a method may not give exactly the same results compared to the finite-element method, especially for the field distributions at locations around sharp corners and edges of the structure, but is useful in predicting the performance trend of



the 2-D structure quickly as the lasing and structural conditions vary. To verify the reliability of the 2-D RPM, the magnitude distribution of the  $z$ -component of Poynting vector  $|S_z|$  (i.e. propagating energy distribution) is plotted for the planar laser with  $t_{\text{GaN}}$  (side length of the GaN rod),  $t_{\text{SiO}_2}$  (thickness of the  $\text{SiO}_2$  separation layer) and  $t_{\text{Al}}$  (thickness of the Al layer) being 68, 8 and 5 nm respectively, see Figure 2.14. From the figure, it can be seen that the distribution calculated by 2-D RPM roughly matched with that by finite-element method with reasonable degree of accuracy.

In the following analysis, we try to vary the dimension of one of the layers at a time and look for the changes in laser performance. In doing so, the dimension of each layer can be fixed one by one in the optimization process. At the operation wavelength  $\lambda_0 = 375 \text{ nm}$ , the refractive indices used for GaN,  $\text{SiO}_2$ , and Al are 2.6221 [14], 1.4731 [15] and  $0.42484 - j4.5244$  [16], respectively. To begin with, we assume the base side length of the GaN rod ( $t_{\text{GaN}}$ ) to be 68 nm, which is equal to the base height of triangular rod in the original design in Figure 2.12a. Then, by fixing the thickness of the  $\text{SiO}_2$  separation layer ( $t_{\text{SiO}_2}$ ) to a few nominated values, the effective refractive index  $n_{\text{eff},x2}$ , optical confinement factor  $\Gamma$  and effective threshold gain  $G_{\text{th}}$ , are plotted against Al thickness ( $t_{\text{Al}}$ ) in Figure 2.15a to Figure 2.15d. The results show that a thicker Al layer is associated with a smaller modal loss by lowering  $|n_{i,x2}|$  (the magnitude of the imaginary part of  $n_{\text{eff},x2}$ ) (Figure 2.15b), which is proportional to the effective absorption coefficient  $\alpha_{\text{eff}}$  in the decay term  $\exp(-\alpha_{\text{eff}} z)$  of the optical energy, according to

$$\alpha_{\text{eff}} = 2k_0 |n_{i,x2}|. \quad (2.30)$$

The reduction in optical loss is due to the capability of a thicker Al layer to prevent light



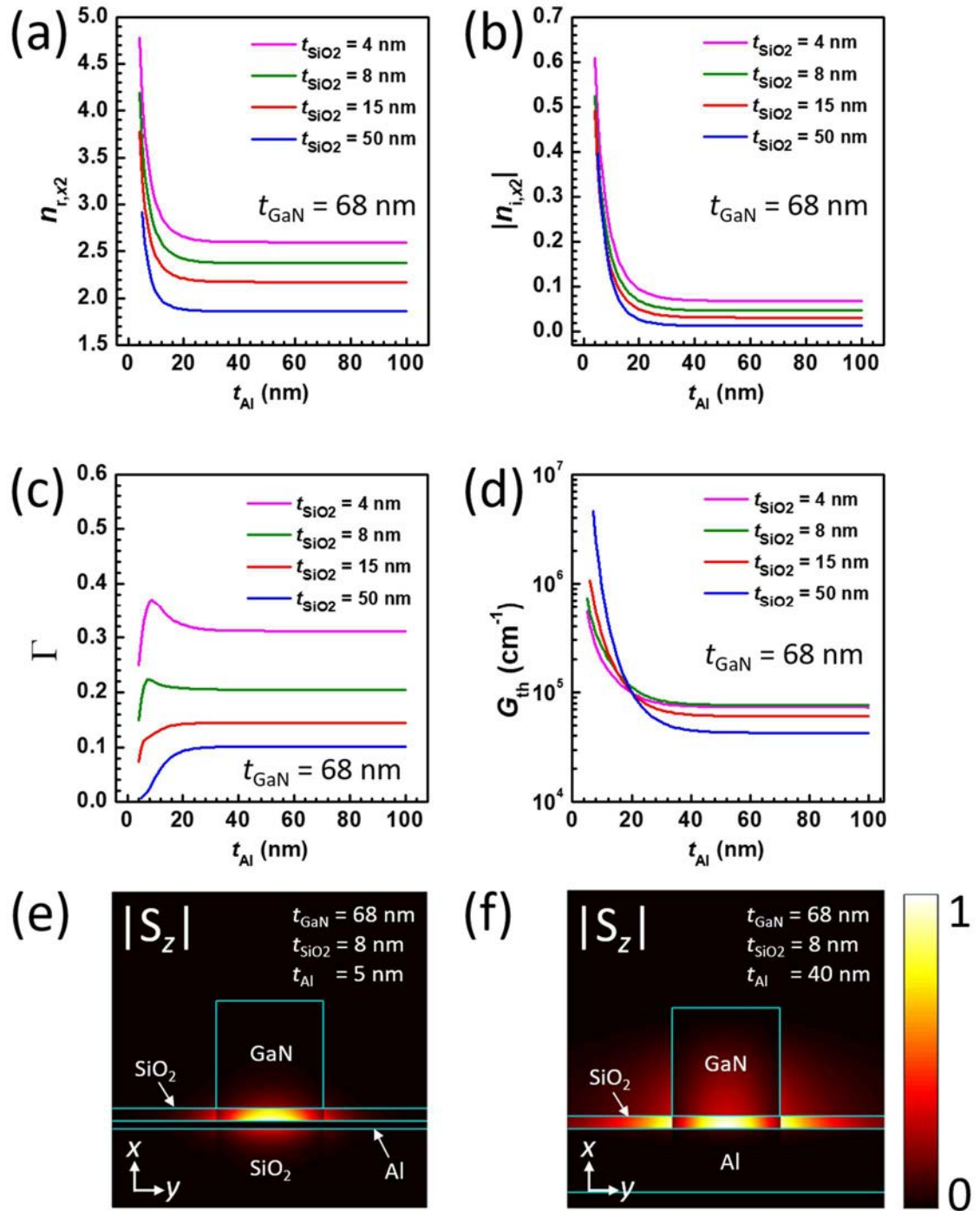


**Figure 2.15** (a) Real part index  $n_{r,x2}$ , (b) imaginary part index  $n_{i,x2}$ , (c) confinement factor  $\Gamma$  and (d) effective threshold gain  $G_{th}$  of the GaN laser formed by square-based GaN rod ( $t_{GaN} = 68$  nm) on SiO<sub>2</sub>-Al-SiO<sub>2</sub> planar structure for various Al thicknesses ( $t_{Al}$ ) when the thickness of SiO<sub>2</sub> separation layer ( $t_{SiO_2}$ ) is fixed at 4, 8, 15 and 50 nm, calculated by 2-dimensional RPM. (e) and (f) respectively show the deduced modal magnitude distribution of the z-component of the Poynting vector  $|S_z|$  of the laser for  $t_{Al} = 5$  nm and  $t_{Al} = 40$  nm, when  $t_{GaN} = 68$  nm and  $t_{SiO_2} = 8$  nm.

from penetrating through it, such that it is able to form surface plasmon exclusively with the separation layer and the gain medium GaN, but not with the substrate. To visualize this idea, we have plotted the modal  $|S_z|$  distribution for  $t_{Al} = 5$  nm and  $t_{Al} = 40$  nm in Figure 2.15e and Figure 2.15f respectively. The two figures clearly show that for the same  $t_{GaN}$  and  $t_{SiO_2}$  values, a thinner Al layer causes significantly more optical energy confined at the substrate, because it allows surface plasmon to couple to the substrate-Al interface. In this way, a much higher amount of light propagates in the metallic layer in the optical mode by forming surface plasmon on both Al interfaces, so more optical energy is lost through metallic absorption. For this reason, it is desirable to use a thicker Al layer to confine most of the light within the upper part of the structure, resulting in a much larger fraction of total optical energy in the gain medium (i.e. confinement factor  $\Gamma$ , see Figure 2.15c and f). With both effects from the decrease in  $|n_{i,x2}|$  and increase in  $\Gamma$  due to a thicker Al layer,  $G_{th}$  ( $= \alpha_{eff} / \Gamma$ ) is reduced by a significant amount (Figure 2.15d), making laser output from the structure possible with lower pump energy. It is important to note that a 40-nm Al layer is thick enough to block almost all of the light from penetrating through it, a further increase in  $t_{Al}$  beyond 40 nm makes negligible difference in the performance of the laser. This phenomenon is shown in Figure 2.15a to Figure 2.15d, where all of the parameters,  $n_{eff,x2}$ ,  $\Gamma$ , and  $G_{th}$  are stabilized for  $t_{Al} > 40$  nm, indicating that the optical energy distribution and the optical mode in the structure is independent of  $t_{Al}$  in this regime. Therefore, one may choose  $t_{Al} = 40$  nm for this laser structure in order to attain low  $G_{th}$  with minimum physical size, as well as small fluctuation in performance due to a slight deviation in  $t_{Al}$  during fabrication of the real structure. As a side note, one may also notice from Figure 2.15e and Figure 2.15f that increasing  $t_{Al}$  also causes light to be less tightly confined when the formation of SP

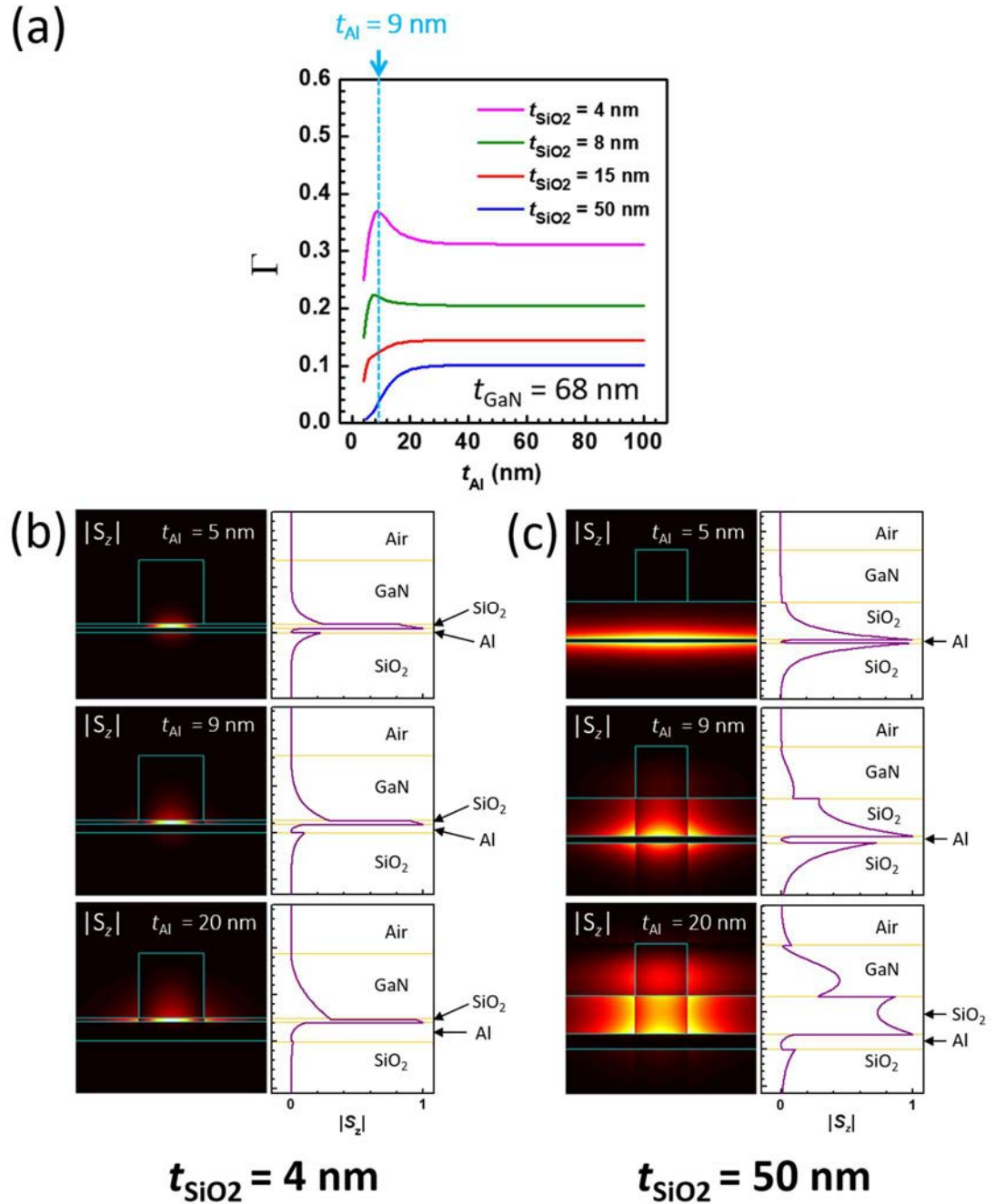


**Figure 2.16** Explanation of the existence of local maxima in Figure 2.14c.

mainly relies on one instead of both Al interfaces. This effect negatively impacts  $\Gamma$  and counteracts the effect of  $\Gamma$  enhancement due to exclusive SP confinement at the top Al-SiO<sub>2</sub> interface. For example, in the case of  $t_{\text{SiO}_2} = 4 \text{ nm}$ , this counteraction results in a local maximum at  $t_{\text{Al}} = 9 \text{ nm}$  as shown in Figure 2.16a. When thickening the Al layer

while  $t_{\text{Al}} < 9$  nm, the effect of  $\Gamma$  enhancement outweighed that of  $\Gamma$  reduction, which gives an overall rise in  $\Gamma$ . However, for  $t_{\text{Al}} > 9$  nm, since almost all of the light is confined at the top Al interface, the effect of  $\Gamma$  enhancement is minimal and an overall reduction of  $\Gamma$  results. See the modal energy distributions in Figure 2.16b at different Al thicknesses. It is noted that a local maximum of  $\Gamma$  does not exist for greater values of  $t_{\text{SiO}_2}$  (e.g. 50 nm) because a larger amount of light is coupled at the bottom initially for small  $t_{\text{Al}}$  when a thicker low-index separation layer is inserted (Figure 2.16c). Therefore, the effect of  $\Gamma$  enhancement upon the thickening of Al layer would be much more significant and it would always be dominant in this case.

We now take a look at the effect of the  $\text{SiO}_2$  separation layer and its thickness  $t_{\text{SiO}_2}$  on the performance of the laser. In fact, it is common for researchers to consider a thin dielectric separation layer between the gain medium and metallic layer to control the metallic absorption and confinement factor in this kind of plasmonic slot waveguides [17-19]. A very thin separation layer is sufficient to bring about major changes in the amount of metallic absorption, field distribution, and  $G_{\text{th}}$ . To illustrate this idea, we have plotted the  $|S_z|$  distribution of the plasmonic mode of our proposed structure with and without an 8-nm  $\text{SiO}_2$  separation layer in Figure 2.17e and Figure 2.17f, respectively. On one hand, it can be observed that the structure with the separation layer has much less light confined within the GaN rod, resulting in a lower value of  $\Gamma$ . On the other hand, this causes much less energy to be confined within the Al layer as well, which leads to reduced metallic absorption of optical energy (i.e. lower  $|n_{i,x2}|$ ). The two effects caused by the insertion of the separation layer can be observed from Figure 2.17b and Figure 2.17c, where  $|n_{i,x2}|$  and  $\Gamma$  are respectively plotted against  $t_{\text{SiO}_2}$  when  $t_{\text{GaN}} = 68$  nm and  $t_{\text{Al}} = 40$  nm. At smaller values of  $t_{\text{SiO}_2}$ ,  $\Gamma$  first decreases

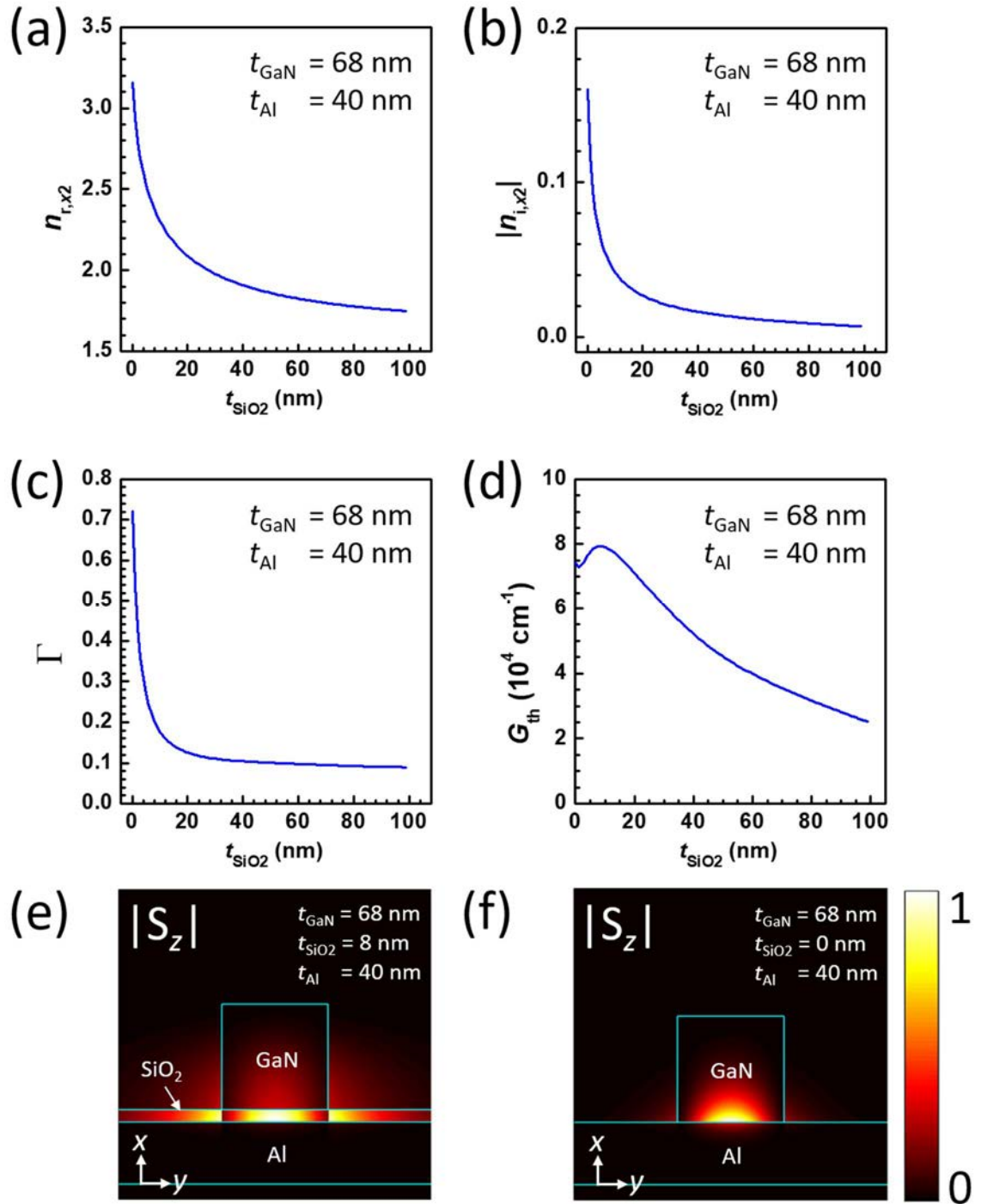
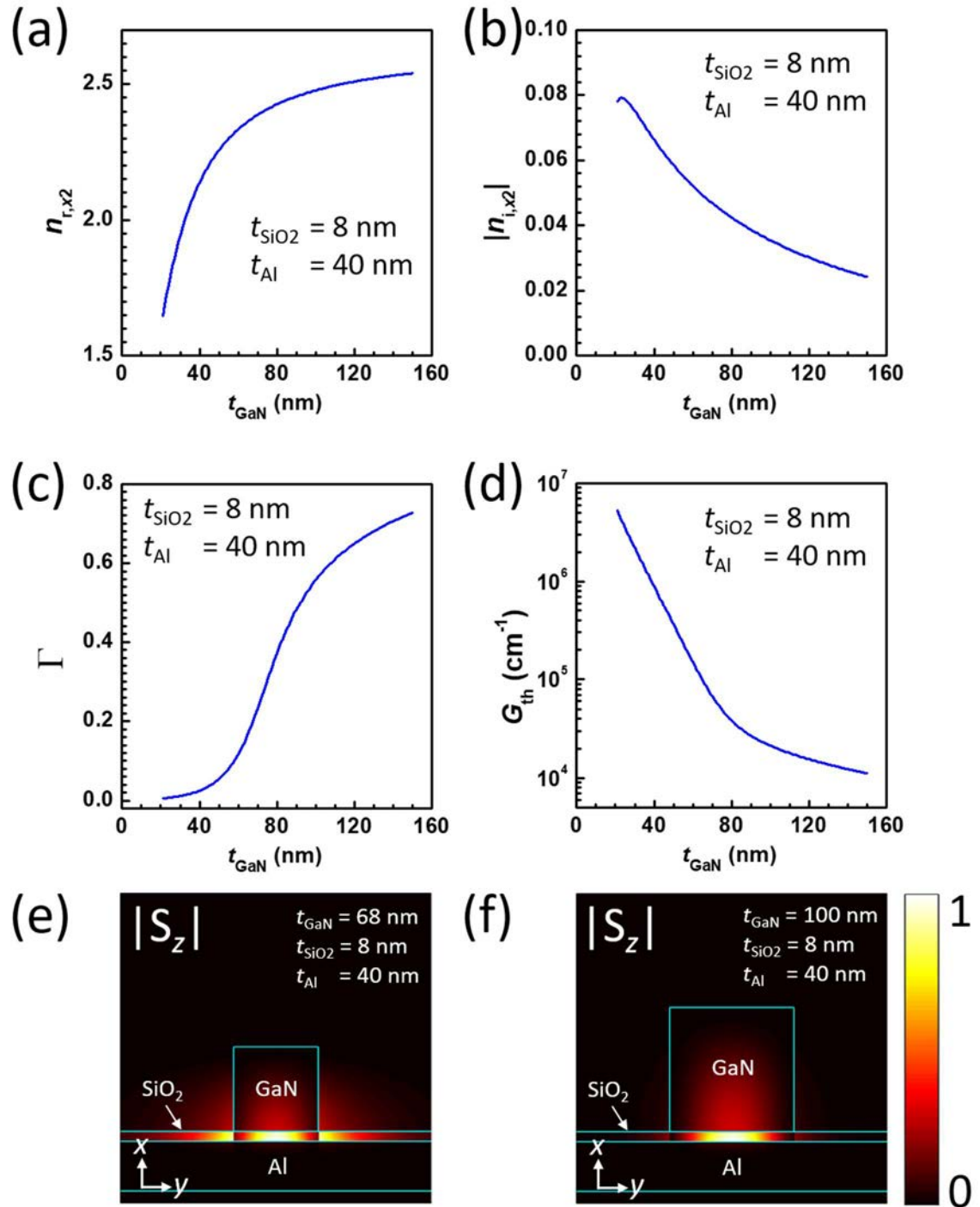


Figure 2.17 (a) Real part index  $n_{r,x2}$ , (b) imaginary part index  $n_{i,x2}$ , (c) confinement factor  $\Gamma$  and (d) effective threshold gain  $G_{\text{th}}$  of the GaN laser formed by square-based GaN rod ( $t_{\text{GaN}} = 68 \text{ nm}$ ) on  $\text{SiO}_2\text{-Al-SiO}_2$  planar structure ( $t_{\text{Al}} = 40 \text{ nm}$ ) for various  $\text{SiO}_2$  thicknesses ( $t_{\text{SiO}_2}$ ), calculated by 2-dimensional RPM. (e) and (f) respectively show the deduced modal magnitude distribution of the z-component of the Poynting vector  $|S_z|$  of the laser with and without an 8-nm  $\text{SiO}_2$  separation layer.

rapidly as  $t_{\text{SiO}_2}$  increases, since a thicker separation layer is capable of accommodating more light energy, leaving less light staying at the GaN rod. At the same time, with a much lower refractive index than GaN,  $\text{SiO}_2$  forms surface plasmon with less light distributed at the Al layer. This reduces  $|n_{i,x2}|$  (i.e. optical loss) significantly. At greater  $t_{\text{SiO}_2}$  values, further thickness increment has less impact on  $\Gamma$  and  $|n_{i,x2}|$  because the separation layer becomes thick enough to accommodate most of the light energy within itself. To further confirm that a higher fraction of modal light energy is staying at the separation layer as  $t_{\text{SiO}_2}$  increases,  $n_{r,x2}$  (i.e. the real part of  $n_{\text{eff},x2}$ ) is plotted against  $t_{\text{SiO}_2}$  in Figure 2.17a, which shows  $n_{r,x2}$  drops and approaches to the bulk refractive index of  $\text{SiO}_2$  ( $= 1.4731$ ) as the separation layer gets thicker. This is a solid indication that light is shifting from the high-index GaN rod ( $n = 2.6221$ ) to the low-index  $\text{SiO}_2$  layer. When combining the effects on  $\Gamma$  and  $|n_{i,x2}|$ , the resulting trend of  $G_{\text{th}}$  is plotted in Figure 2.17d, which shows the effect of  $\Gamma$  reduction outweighs that of  $|n_{i,x2}|$  reduction for  $t_{\text{SiO}_2} < 10$  nm, so  $G_{\text{th}}$  slightly increases. As for  $t_{\text{SiO}_2} > 10$  nm, the effect of  $|n_{i,x2}|$  becomes dominant and outweighs that of  $\Gamma$ , which gives a significant drop in  $G_{\text{th}}$ . It can be seen that the curve does not level-off for  $t_{\text{SiO}_2}$  values up to 100 nm, so the suitable value of  $t_{\text{SiO}_2}$  in the design highly depends on the laser's application. One may either incorporate a thinner separation layer for the smaller physical size of the laser at the cost of higher  $G_{\text{th}}$ , or a thicker one for lower  $G_{\text{th}}$  when the physical size is not a big concern.

Varying the cross-sectional side length of the GaN rod (i.e.  $t_{\text{GaN}}$ ) also affects the performance of the laser. Similar to the  $\text{SiO}_2$  separation layer, a GaN rod with the larger cross-sectional area is associated with the capability to confine a greater fraction of total light energy. Figure 2.18e plots the  $|S_z|$  distribution of the plasmonic mode of the laser with  $t_{\text{GaN}} = 68$  nm,  $t_{\text{SiO}_2} = 8$  nm and  $t_{\text{Al}} = 40$  nm, where a noticeable amount of light





**Figure 2.18** (a) Real part index  $n_{r,x2}$ , (b) imaginary part index  $n_{i,x2}$ , (c) confinement factor  $\Gamma$  and (d) effective threshold gain  $G_{\text{th}}$  of the GaN laser formed by square-based GaN on SiO<sub>2</sub>-Al-SiO<sub>2</sub> planar structure ( $t_{\text{SiO}_2} = 8$  nm;  $t_{\text{Al}} = 40$  nm) for various GaN side lengths ( $t_{\text{GaN}}$ ), calculated by 2-dimensional RPM. (e) and (f) respectively show the deduced modal magnitude distribution of the z-component of the Poynting vector  $|S_z|$  of the laser when  $t_{\text{GaN}} = 68$  nm and  $t_{\text{GaN}} = 100$  nm.



energy is found to be escaping from the structure to the surrounding. However, by increasing  $t_{\text{GaN}}$  (e.g. to 100 nm), the fraction of light escaped is much reduced, as presented in Figure 2.18f. With this property, it is within our expectation that  $\Gamma$  increases with increase in  $t_{\text{GaN}}$  (Figure 2.18c). Moreover, with more light confined in the GaN rod, a less fraction of light energy will be dissipated through metallic absorption, and a decrease in  $|n_{i,x2}|$  results (Figure 2.18b). Again, increasing  $t_{\text{GaN}}$  enhances  $G_{\text{th}}$  without saturation within the regime  $t_{\text{GaN}} < 150$  nm, so the suitable  $t_{\text{GaN}}$  value depends on the laser's application. There is a trade-off between the laser's physical size and performance.

With the above examples in this section, RPM is shown to be a useful technique for quick 1-D planar laser analysis with sufficient accuracy, which solves for any supported optical mode at a particular wavelength. The idea can further be extended to analyze some 2-D waveguides with simple geometry, as well as finding the performance trend as the dimension of the laser varies.

## 2.4. Whispering-gallery Modes of Multi-layer Circular Waveguides

Circular waveguides, especially the ones of cylindrical shape, is also popular among researchers in recent years [3, 20-22]. One of the most attractive properties of circular lasers is their capability to support whispering-gallery modes (WGMs), which are often expected to have low optical loss compared to the longitudinal modes. In fact, WGMs of circular waveguides can also be modeled using similar concepts in RPM under the cylindrical coordinate plane. Such a method is demonstrated in this section.



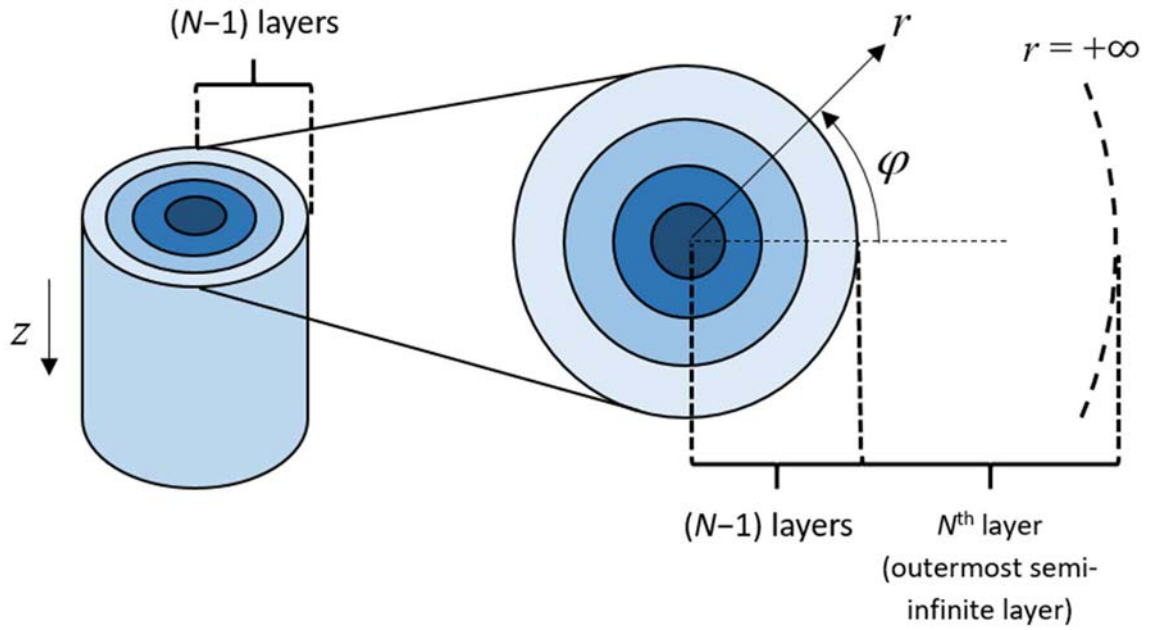


**Figure 2.19** 3-D multi-layer cylindrical structure (left) and its corresponding 2-D representation (right).  $r$ ,  $\phi$  and  $z$  represent the radial, azimuthal and longitudinal positions, respectively.

The type of multi-layer circular waveguide considered in this section is shown in Figure 2.19, which includes  $(N-1)$  radial-layers, where the core (innermost layer) is defined as the first layer ( $i = 1$ ). The semi-infinite medium surrounding the waveguide is regarded as the  $N$ -th layer. With this structure, light can propagate along the azimuth ( $\phi$ ) to form a closed loop as the roundtrip. When this roundtrip of light results in constructive interference, WGM is formed, with the general form of the magnetic field of the  $\text{TM}_{v,l}$  mode in the  $i$ -th layer ( $i = 1, 2, 3, \dots, N$ ) given by

$$H_{zi} = H_{zi0} \exp[j(\omega t \pm v\phi)], \quad (2.31)$$

where  $H_{zi0}$ ,  $\omega$  and  $t$  is the amplitude coefficient, angular frequency and time, respectively.  $v$  is the azimuthal mode number, which can be understood as the number of wavelengths accommodated within the roundtrip, so it must be an integer for constructive interference and optical resonance to occur.  $l$  is the radial mode order,



which is the number of field intensity extrema along the radial direction. To determine  $H_{zi0}$  in Equation (2.31), we first derive the Helmholtz equation in the cylindrical coordinate plane:

$$\frac{\partial H_{zi}^2}{\partial r^2} + \frac{1}{r} \frac{\partial H_{zi}}{\partial r} + \frac{1}{r^2} \frac{\partial H_{zi}^2}{\partial \varphi^2} + k_0^2 n_i^2 H_{zi} = 0, \quad (2.32)$$

where  $k_0$  is the vacuum wavenumber and  $n_i$  is the refractive index of the  $i$ -th layer. Equation (2.32) is derived from the Maxwell equations using the method similar to that discussed in Chapter 1 (see the derivation of Equation (1.17)), but under the cylindrical coordinate system instead of the Cartesian coordinate system. By putting (2.31) into (2.32), the Helmholtz equation transforms into a Bessel differential equation

$$\alpha_i^2 \frac{\partial^2 H_{zi0}}{\partial \alpha_i^2} + \alpha_i \frac{\partial H_{zi0}}{\partial \alpha_i} + (\alpha_i^2 - \nu^2) H_{zi0} = 0, \quad (2.33)$$

where  $\alpha_i = k_0 n_i r$ . When the waveguide layer is a dielectric,  $n_i$  is purely real, so we have  $\alpha_i^2 > 0$  and the solution of  $H_{zi0}$  is given by

$$H_{zi0} = A_i J_\nu(\alpha_i) + B_i Y_\nu(\alpha_i) \quad (2.34)$$

where  $J_\nu$  and  $Y_\nu$  are respectively the  $\nu$ -order Bessel functions of the first and second kind, and  $A_i$  and  $B_i$  are amplitude coefficients. Alternatively, if the layer concerned is metallic, we have  $|\text{Im}(n_i)| \gg |\text{Re}(n_i)|$ . In this case, we may assume  $\alpha_i^2 < 0$ , since  $n_i$  is approximately a purely imaginary number. With this assumption, (2.33) becomes a modified Bessel differential equation and the solution of  $H_{zi0}$  can be written as

$$H_{zi0} = A_i I_\nu(-j\alpha_i) + B_i K_\nu(-j\alpha_i) \quad (2.35)$$



where  $I_\nu$  and  $K_\nu$  are respectively the  $\nu$ -order modified Bessel functions of the first and second kind. In the cylindrical coordinate system, the electric field components  $E_r$  and  $E_\phi$  can be expressed in terms of  $H_z$  according to the Maxwell equations as

$$E_r = -\frac{j}{\omega\epsilon_0\epsilon_r} \frac{\partial H_z}{\partial \phi} \quad (2.36)$$

$$E_\phi = \frac{j}{\omega\epsilon_0\epsilon_r} \frac{\partial H_z}{\partial r} \quad (2.37)$$

which are analogous to Equations (1.15) and (1.16) in the Cartesian coordinate plane. In addition, at the  $i$ -th interface between the waveguide layers, i.e.  $r = R_i$ , where  $R_i$  is the radius of the  $i$ -th interface from the center of the core, the field components should meet the boundary conditions

$$H_{zi} = H_{z,i+1} \quad (2.38)$$

$$\epsilon_{ri} E_{ri} = \epsilon_{r,i+1} E_{r,i+1} \quad (2.39)$$

$$E_{\phi i} = E_{\phi,i+1} \quad (2.40)$$

for  $i = 1, 2, 3, \dots, (N-1)$ . By expanding and combining (2.38) to (2.40), the amplitude coefficients  $A_i$  and  $B_i$  of adjacent layers can be related by

$$\begin{bmatrix} A_i \\ B_i \end{bmatrix} = M_i \begin{bmatrix} A_{i+1} \\ B_{i+1} \end{bmatrix}, \quad (2.41)$$

where

$$M_i = \frac{1}{C_{ii}' D_{ii} - C_{ii} D_{ii}'} \begin{bmatrix} s_i D_{ii}' C_{i+1,i}' - D_{ii}' C_{i+1,i} & s_i D_{ii}' D_{i+1,i}' - D_{ii}' D_{i+1,i} \\ C_{ii}' C_{i+1,i} - s_i C_{ii}' C_{i+1,i}' & C_{ii}' D_{i+1,i} - s_i C_{ii}' D_{i+1,i}' \end{bmatrix}, \quad (2.42)$$

with

$$C_{pq} = \begin{cases} J_v(kn_p R_q) & \text{if the } p^{\text{th}} \text{ layer is a dielectric} \\ I_v(-jkn_p R_q) & \text{if the } p^{\text{th}} \text{ layer is a metal} \end{cases} \quad (2.43)$$

$$D_{pq} = \begin{cases} Y_v(kn_p R_q) & \text{if the } p^{\text{th}} \text{ layer is a dielectric} \\ K_v(-jkn_p R_q) & \text{if the } p^{\text{th}} \text{ layer is a metal} \end{cases} \quad (2.44)$$

$$s_i = \frac{b_{i+1}}{b_i} \left( \frac{n_i}{n_{i+1}} \right) \quad (2.45)$$

$$b_i = \begin{cases} 1 & \text{if the } i^{\text{th}} \text{ layer is a dielectric} \\ -j & \text{if the } i^{\text{th}} \text{ layer is a metal} \end{cases}. \quad (2.46)$$

Inductively, this can be written into

$$\begin{bmatrix} A_1 \\ B_1 \end{bmatrix} = M_1 M_2 M_3 \cdots M_{N-1} \begin{bmatrix} A_N \\ B_N \end{bmatrix} = \begin{bmatrix} m_{11} & m_{12} \\ m_{21} & m_{22} \end{bmatrix} \begin{bmatrix} A_N \\ B_N \end{bmatrix}. \quad (2.47)$$

It is noted that  $\left| \lim_{r \rightarrow 0} Y_v(\alpha_i) \right| = \left| \lim_{r \rightarrow 0} K_v(-j\alpha_i) \right| = \infty$ . Since the electromagnetic field strength cannot be infinitely large, there should not be any component for  $Y_v$  or  $K_v$  in the first layer, this results in  $B_1 = 0$ . In addition, it is expected that the field is exponentially decaying as  $r \rightarrow \infty$  in the  $N$ -th layer. If the  $N$ -th layer is a dielectric, the field components can be expressed by Hankel function of the first kind  $H_v^{(1)}$ , i.e.  $A_N = 1$  and  $B_N = j$ . If it is a metal, there cannot be any component for  $I_v$  because  $\left| \lim_{r \rightarrow +\infty} I_v(-j\alpha_i) \right| = \infty$ , thus  $A_N = 0$  and we can normalize the component of  $K_v$  by setting  $B_N = 1$ . With all of the above considerations, we can rewrite (2.47) as

$$\begin{bmatrix} A_1 \\ 0 \end{bmatrix} = \begin{cases} \begin{bmatrix} m_{11} & m_{12} \\ m_{21} & m_{22} \end{bmatrix} \begin{bmatrix} 1 \\ j \end{bmatrix} & \text{if the outermost layer is a dielectric} \\ \begin{bmatrix} m_{11} & m_{12} \\ m_{21} & m_{22} \end{bmatrix} \begin{bmatrix} 0 \\ 1 \end{bmatrix} & \text{if the outermost layer is a metal} \end{cases} \quad (2.48)$$

and the requirement for WGM to occur is

$$\begin{cases} m_{21} + jm_{22} = 0 & \text{if the outermost layer is a dielectric} \\ m_{22} = 0 & \text{if the outermost layer is a metal} \end{cases} \quad (2.49)$$

Equation (2.49) solves for the complex solution  $k_0 = k_r - jk_i$ . The initial guess solution is determined by poles (sharp peaks) on the phase derivative plot ( $d\phi/dk_r$  against  $k_r$ , where  $\phi$  is the phase of the L.H.S. of Equation (2.49)) for  $k_i = 0$ , which is similar to RPM discussed in the previous section. The real part  $k_r$  can be used to calculate the vacuum wavelength in which WGM is supported, according to  $\lambda_0 = 2\pi/k_r$ , whereas the imaginary part  $k_i$  represents the optical loss of the WGM, this is reflected in the cold-cavity quality factor ( $Q$ ) of the mode calculated by

$$Q = \left| \frac{k_r}{2k_i} \right|. \quad (2.50)$$

The threshold gain  $G_{th}$  of the gain layer can be calculated by substituting  $k_0 = k_r$  back into Equation (2.49) as a purely real number, followed by solving the equation again for the imaginary part of the refractive index  $n_i$  of the gain layer. The resulting imaginary part  $\text{Im}(n_i)$  can be used to calculate  $G_{th}$  by

$$G_{th} = 2k_r \text{Im}(n_i). \quad (2.51)$$

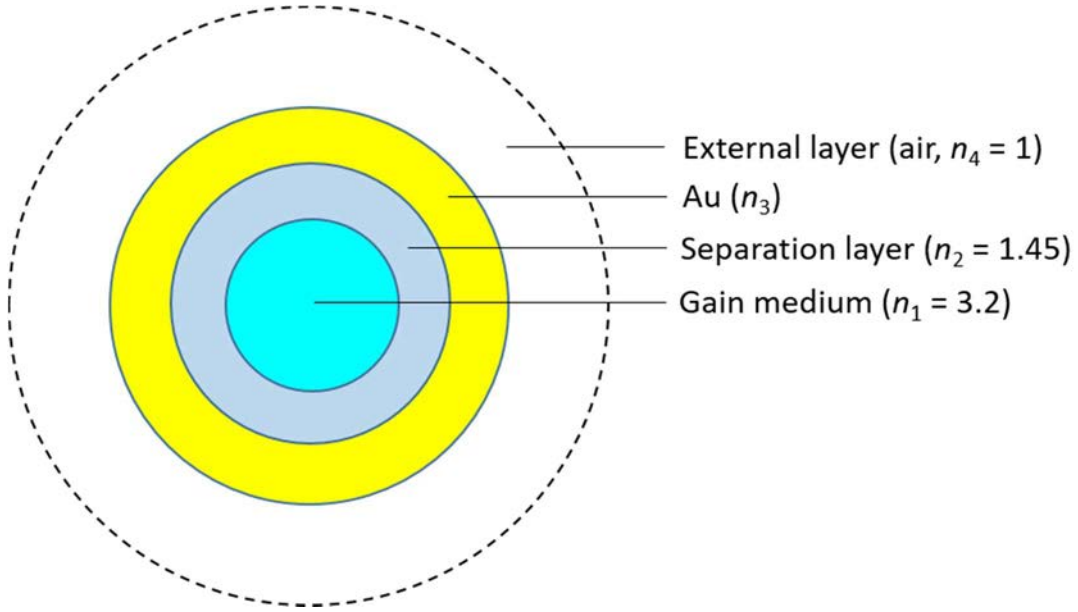


**Figure 2.20 2-D radially-layered circular laser designed by Yao et al. [23]**

The concept in the calculation of  $G_{th}$  with the circular WGM is very similar to what has been discussed in the previous section with the planar waveguides. However, in Equation (2.51), the confinement factor  $\Gamma$ , is already taken into account, there is no need to further divide the result by  $\Gamma$ .

Here, we have chosen a radially-layered circular waveguide designed by Yao et al. [23]. The design, which is shown in Figure 2.20, adopts the concept similar to the planar plasmonic slot waveguide with GaN rod. It consists of a cylindrical gain medium rod (active core) coated by gold, with a dielectric separation layer inserted in between, and the whole structure is assumed to be surrounded by air (the outermost layer). While the refractive indices of the gain medium ( $n_1 = 3.2$ ), separation layer ( $n_2 = 1.45$ ) and air ( $n_4 = 1$ ) are assumed to be constants within the wavelength range in our analysis, the refractive index of gold ( $n_3$ ) is considered to be wavelength-dependent. In the following analysis, we will determine  $n_3$  by modeling the complex relative permittivity ( $\epsilon_r$ ) of gold according to the Lorentz-Drude Model

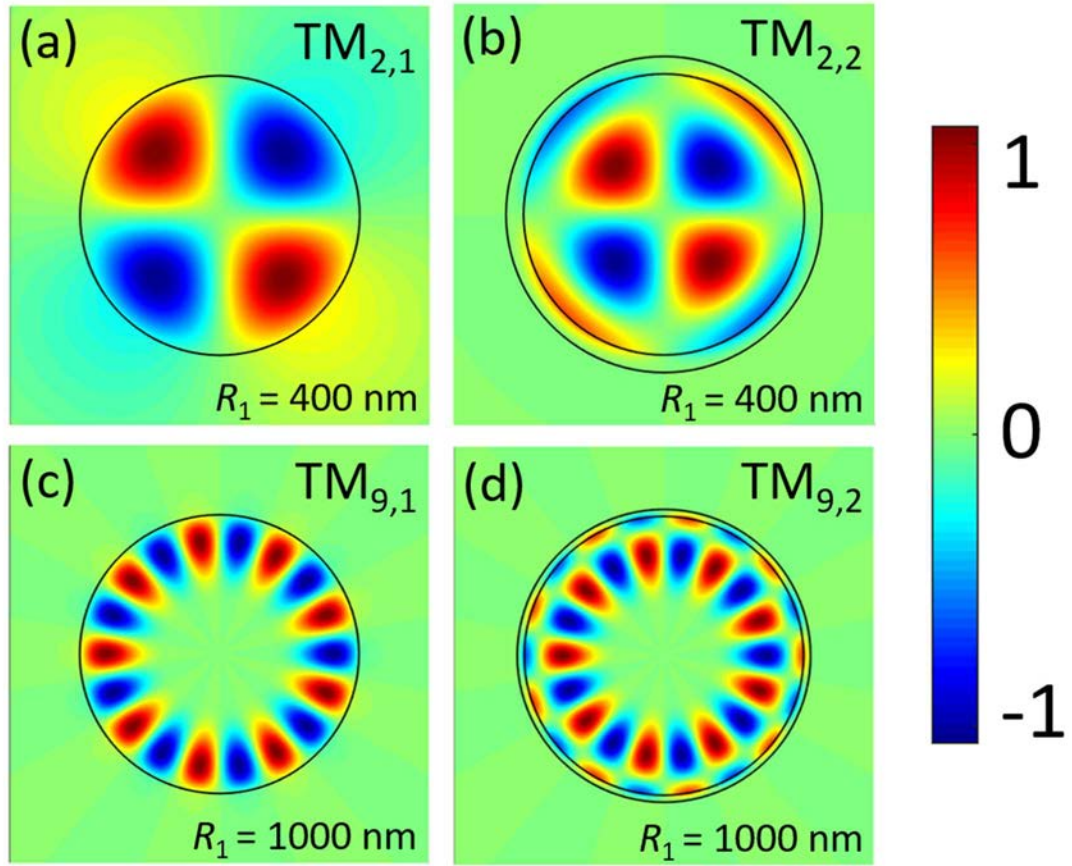


**Figure 2.21** Real  $H_z$  distribution of (b)  $TM_{2,2}$  and (a)  $TM_{2,1}$  mode of a bare active core of radius  $R_1 = 400$  nm with and without a 50-nm gold layer, respectively; real  $H_z$  distribution of (c)  $TM_{9,2}$  and (a)  $TM_{9,1}$  mode of a bare active core of radius  $R_1 = 1000$  nm with and without a 50-nm gold layer, respectively.

$$\varepsilon_r(\omega) = \varepsilon_r(\infty) - \frac{\omega_D^2}{\omega(\omega + j\gamma_D)} - \frac{\Delta\varepsilon_r\Omega_L^2}{(\omega^2 - \Omega_L^2) - j\Gamma_L\omega}, \quad (2.52)$$

where  $\frac{\omega_D}{2\pi} = 2113.6$  THz,  $\frac{\gamma_D}{2\pi} = 15.92$  THz,  $\frac{\Omega_L}{2\pi} = 650.07$  THz and  $\frac{\Gamma_L}{2\pi} = 104.86$  THz

are the plasma frequency, damping coefficient, resonance frequency and spectral width, respectively.  $\Delta\varepsilon_r = 1.09$  is a weighting factor and  $\varepsilon_r(\infty) = 5.9673$  [23].

To study the effect of the gold layer on the laser performance. We first consider the case of low  $\nu$ -order ( $\nu = 2$ ) in a bare active core of radius  $R_1 = 400$  nm without the separation layer and the gold layer. As shown in Figure 2.21a, for the  $TM_{2,1}$  mode, a



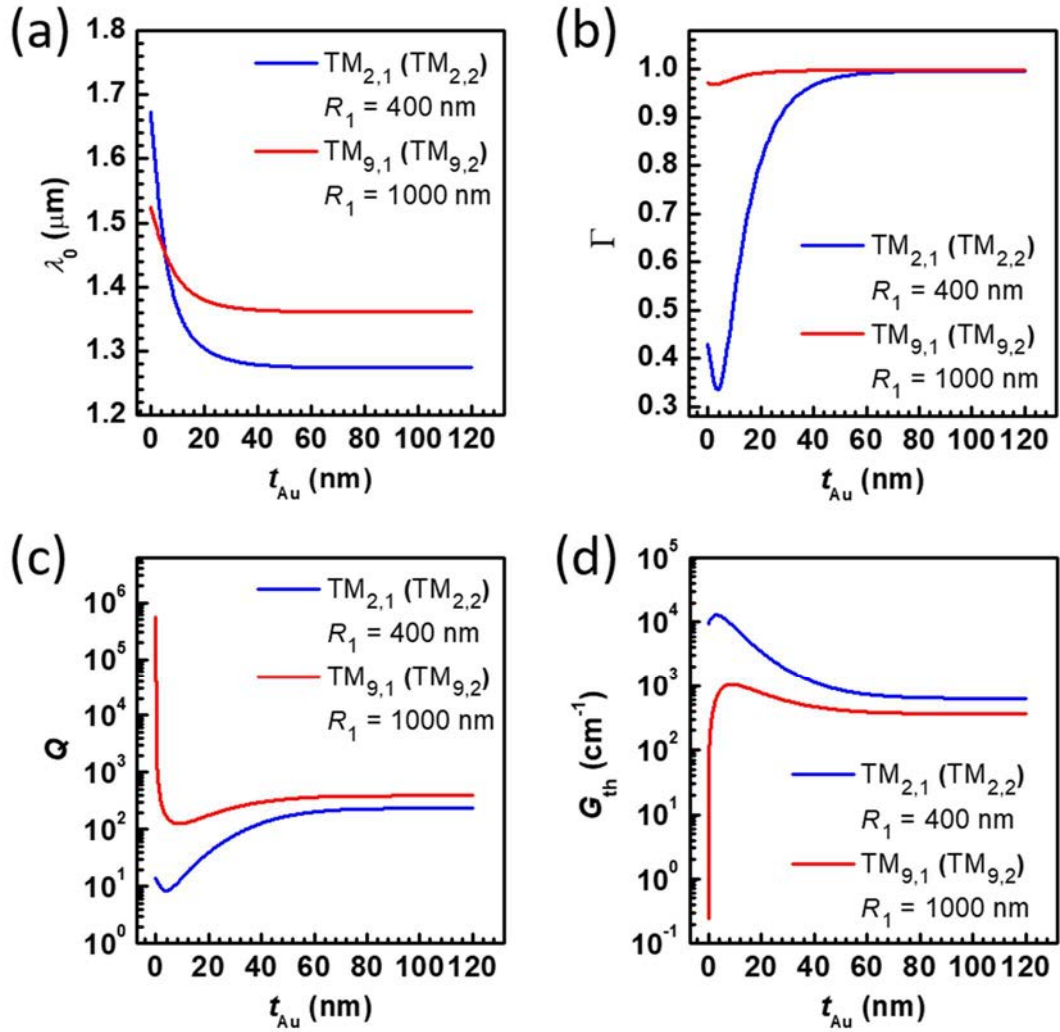


**Figure 2.22** (a) Mode wavelength  $\lambda_0$ , (b) confinement factor  $\Gamma$ , (c) quality factor  $Q$  and (d) threshold gain  $G_{th}$  of the TM<sub>2,1</sub> (TM<sub>2,2</sub>) mode ( $R_1 = 400$  nm) (blue curves) and the TM<sub>9,1</sub> (TM<sub>9,2</sub>) mode ( $R_1 = 1000$  nm) (red curves) of a bare active core with different gold layer thicknesses  $t_{Au}$ .

significant amount of light field escapes from the core to the surrounding due to the small incident angle of internal reflection inside the core. The corresponding confinement factor  $\Gamma$  is only around 0.4. This can be greatly improved by coating the core with a gold layer. The gold layer transforms the TM<sub>2,1</sub> mode into the TM<sub>2,2</sub> mode by surface plasmon formation, which is shown in Figure 2.21b. The result shows that a gold layer of thickness  $t_{Au} = 50$  nm is able to prevent light from escaping from the cavity by subwavelength light confinement at the core-metal interface, achieving  $\Gamma$



values close to unity ( $\sim 0.95$ ), see Figure 2.22b. The increment in  $\Gamma$  improves the overall performance of the laser, including the quality factor  $Q$  and threshold gain  $G_{\text{th}}$ . For the case of high  $\nu$ -order ( $\nu = 9$ ), we have chosen a bare core of radius  $R_1 = 1000$  nm, such that the mode wavelength  $\lambda_0$  is comparable to the previous case with  $\nu = 2$ . We have confirmed this by plotting  $\lambda_0$  against  $t_{\text{Au}}$  for both cases in Figure 2.22a, which indicates that both cases have values of  $\lambda_0$  between 1.2 and 1.7  $\mu\text{m}$ . In the high-order case, it is found that almost all of the light field can be kept within the bare core even without the gold layer, with  $\Gamma \sim 0.97$ , because the incident angle of light is large enough to achieve total internal reflection at the core-air interface, see Figure 2.21c. Adding a 50-nm gold layer in this case also transforms the purely dielectric mode (TM<sub>9,1</sub> mode) into a hybrid mode (TM<sub>9,2</sub> mode) (Figure 2.21d), but this does not make a significant improvement in  $\Gamma$  when compared to the low-order case.

For both the low-order and high-order cases, the trend of  $\Gamma$  for  $t_{\text{Au}}$  values between 0 and 120 nm, is presented in Figure 2.22b. When a very thin gold layer (e.g. 5 nm) is coated onto the bare active core,  $\Gamma$  is lowered slightly for both cases, since light is capable to penetrate through it to form surface plasmon at the gold-air interface. As  $t_{\text{Au}}$  further increases,  $\Gamma$  rises again and gets very close to unity at the regime  $t_{\text{Au}} > 60$  nm, where the gold layer is thick enough to prevent light from coupling to the gold-air surface to form surface plasmon. For the low-order case, since the initial value of  $\Gamma$  when  $t_{\text{Au}} = 0$  nm is much lower than the high-order one, the improvement in  $\Gamma$  is much more significant in this regime. The effect of such a great improvement in  $\Gamma$  outweighs the effect of the introduced metallic absorption due to the gold layer. This can be seen from Figure 2.22c and Figure 2.22d, where  $Q$  and  $G_{\text{th}}$  are increased and decreased by up to one order of magnitude, respectively. On the other hand, from the

same figures,  $Q$  and  $G_{th}$  are decreased and increased by three orders of magnitude for the high-order WGM, because the gold layer does not result in much increase in  $\Gamma$ , and the effect from metallic absorption becomes dominant. These results show that without a separation layer, a metallic layer can enhance the WGM lasing performance of a cylindrical bare active core only when the mode used has low  $\Gamma$  values (e.g. with low  $\nu$ -order or small core radius). The metallic layer forms a closed core-metal interface for surface plasmon formation, which confines light in subwavelength scale in the radial direction, preventing light from escaping from the core.

To further enhance the range of  $Q$  and  $G_{th}$  modulation (i.e. tunability) of the laser, a dielectric separation layer can be inserted between the core and the gold layer. With a separation layer of thickness ( $t_{sep}$ ) between 0 and 1000 nm inserted between an active core of radius  $R_1 = 1000$  nm and a 200-nm gold layer, the performance trend of the  $TM_{10,1}$  and  $TM_{10,2}$  modes of the structure is calculated. The results can be found in Figure 2.23. For the  $TM_{10,1}$  mode, the introduction of a thin separation layer causes dramatic mode shift, with the mode wavelength  $\lambda_0$  changing rapidly, as observed in Figure 2.23a. The cause of this phenomenon can be found by calculating the modal field distribution with and without a thin (e.g. 200 nm) separation layer, which are shown in Figure 2.24b and Figure 2.24a respectively. According to Figure 2.24a, the laser without a separation layer results in a purely plasmonic  $TM_{10,1}$  mode confined at the core-gold interface. However, with the presence of a 200-nm separation layer, it transforms into a hybrid mode, with only a small fraction of the light field getting involved in surface plasmon formation. On the contrary, the mode shift is much less in for the  $TM_{10,2}$  mode upon the insertion of the same separation layer, because it is initially a hybrid mode even without the separation layer (Figure 2.24g). Adding a 200-nm separation layer

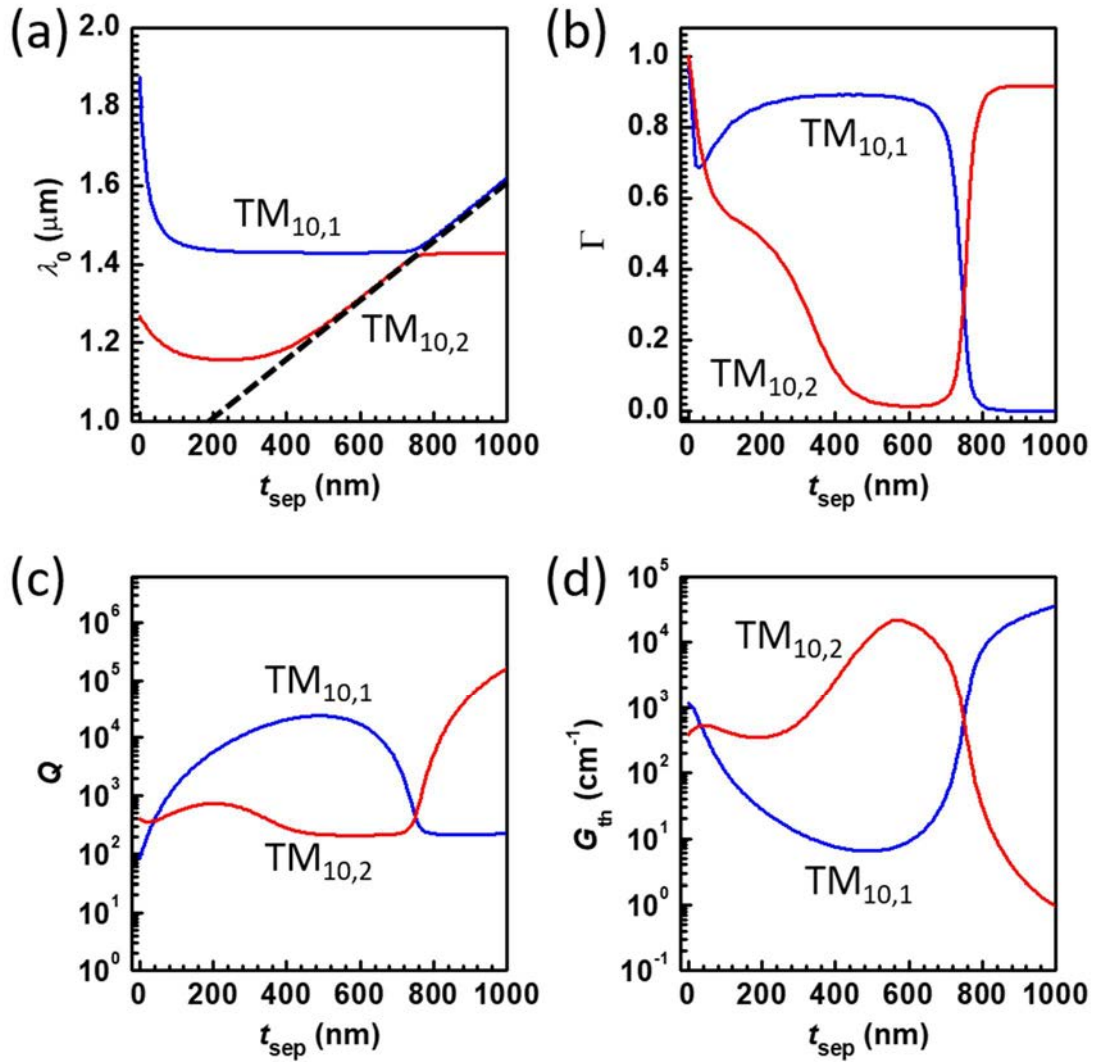


**Figure 2.23** (a) Mode wavelength  $\lambda_0$ , (b) confinement factor  $\Gamma$ , (c) quality factor  $Q$  and (d) threshold gain  $G_{\text{th}}$  of the  $\text{TM}_{10,1}$  (blue curves) and  $\text{TM}_{10,2}$  (red curves) modes in the circular cavity with an active core of radius  $R_1 = 1000$  nm and gold layer thickness  $t_{\text{Au}} = 200$  nm, when the thickness of the separation layer ( $t_{\text{sep}}$ ) varies from 0 to 1000 nm.

has little impact on the amount of surface plasmon, see Figure 2.24h. For  $200 \text{ nm} < t_{\text{sep}} < 600 \text{ nm}$ , the thickening of the separation layer causes the light field in the  $\text{TM}_{10,2}$  mode to move away from the core to the separation layer, as shown in Figure 2.24h in comparison to Figure 2.24i. The  $\text{TM}_{10,2}$  mode prefers propagating in the low-index separation layer because of its shorter mode wavelength. As a result,  $\Gamma$  drops rapidly, contributing to the increment of  $G_{\text{th}}$ .  $Q$  is also lowered due to the increased

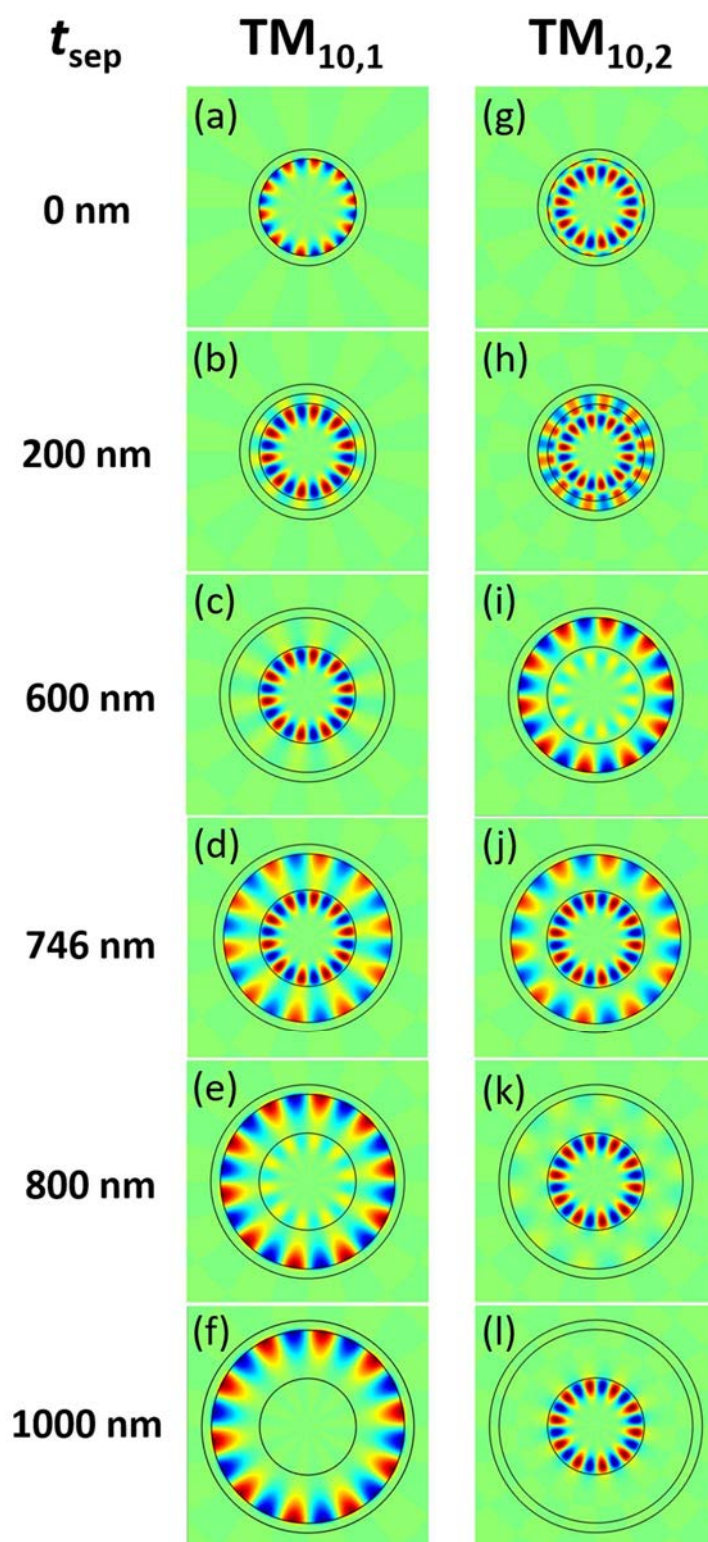


Figure 2.24 Real  $H_z$  distribution of the  $\text{TM}_{10,1}$  and  $\text{TM}_{10,2}$  modes in the circular cavity with separation layer of thickness  $t_{\text{sep}} = 0$  nm, 200 nm, 600 nm, 750 nm, 800 nm and 1000 nm inserted between the active core ( $R_1 = 1000$  nm) and the gold layer ( $t_{\text{Au}} = 200$  nm).

involvement of surface plasmon of the mode. On the contrary, such kind of transformation does not happen to the  $TM_{10,1}$  mode within this regime, as it has greater  $\lambda_0$  values, so the light field prefers to stay within the high-index core region (Figure 2.24b and Figure 2.24c). This keeps  $\Gamma$  high and steady (Figure 2.23b). The increment in  $Q$  and reduction in  $G_{th}$  for the  $TM_{10,1}$  mode in this regime are caused by less surface plasmon formation with a thicker separation layer. In another regime with  $600 \text{ nm} < t_{sep} < 1000 \text{ nm}$ , it can be noticed that the  $\lambda_0$  trends of the  $TM_{10,1}$  and  $TM_{10,2}$  modes form a virtual straight line (black dashed line in Figure 2.23a), where  $\lambda_0$  is directly proportional to  $t_{sep}$ . As  $t_{sep}$  increases, this occurs to the  $TM_{10,2}$  mode first, in which the region of the separation layer is now too large in comparison to the core. In this case, light field of the highly plasmonic mode (Figure 2.24i) gradually shifts from the separation layer back to the core region, as shown in Figure 2.24i to Figure 2.24l. This increases  $\Gamma$  and  $Q$ , which in return reduces  $G_{th}$  by around 4 orders of magnitude. On the other hand, light field of the  $TM_{10,1}$  mode now finds such a large region of separation layer preferable for propagation. In this case, it shifts from the core to the outer region for surface plasmon formation (Figure 2.24c to Figure 2.24f), resulting in a drop of  $\Gamma$  and  $Q$ , and an enormous rise in  $G_{th}$ . Within this regime, there exists a point at  $t_{sep} \sim 746 \text{ nm}$ , where both the  $TM_{10,1}$  and  $TM_{10,2}$  modes have similar values of  $\lambda_0$ ,  $\Gamma$ ,  $Q$ , and  $G_{th}$ , this is called the coupling point [23]. It is found that the field intensity distributions of both modes around this point are similar, see Figure 2.24d and Figure 2.24j. Such a phenomenon also occurs in other modes with adjacent radial mode orders (e.g.  $TM_{10,2}$  and  $TM_{10,3}$ ), enabling great tunability of the laser for various wavelengths by modifying  $t_{sep}$ .



Similar to the planar slot laser structure, it is found that the incorporation of a metallic layer also enables surface plasmon propagation in the WGMs of 2-D cylindrical lasers. A dielectric separation layer can be inserted between the dielectric active core and the metallic layer for enhanced tunability by modifying the amount of field getting involved in surface plasmon formation in the hybrid modes.

## 2.5. Conclusion

From the above theoretical analysis, it can be seen that a combination of metallic layer and a dielectric separation layer enable us to modify the waveguiding performance of lasers with different geometries. It was found that a typical metallic layer of thickness less than 100 nm is sufficient to support plasmonic modes of subwavelength confinement without unnecessary metallic loss through SP coupling on both sides of the metal. In addition, a low-index dielectric layer can be inserted between the metallic layer and the gain medium as a separation layer for the support of hybrid modes. The proportion of plasmonic and dielectric nature of the hybrid modes can be tuned over a wide range by changing the dielectric thickness, achieving high tunability of the waveguiding performances.



### 3. Experimental Study of Lasing Characteristics

Despite theoretical analysis gives us the concept of how well a laser would perform under various conditions, the performance of a laser in the practical situation can be affected by other factors, such as structural defects [24] and temperature [25]. Therefore, it is necessary for us to perform experimental analysis on real laser structures, in order to determine their performances under practical situations. In this chapter, the experimental techniques used in this work will be discussed.

#### 3.1. Spectral Analysis of Lasers

When analyzing the performance of a light-emitting optical device, it is useful to obtain the wavelength spectrum of the light emitted during its operation. We can deduce different information, including the quality factor, lasing threshold and the type of lasing mode, of the lasers, through the study of their wavelength spectra. Such a technique is called spectral analysis.

In the spectral analysis of lasers, there are three typical types of wavelength spectra obtained, which are shown in Figure 3.1 [26]. When a gain medium is pumped without achieving population inversion, spontaneous emission of the excited molecules would give photoluminescence (PL). The peak of PL on a wavelength spectrum usually has a broad full-width at half-maximum (FWHM) (e.g. 80 nm). When the pump power is sufficient to attain population inversion of the gain material, amplified spontaneous emission (ASE) results instead [27]. In this case, the FWHM of the spectral peak would



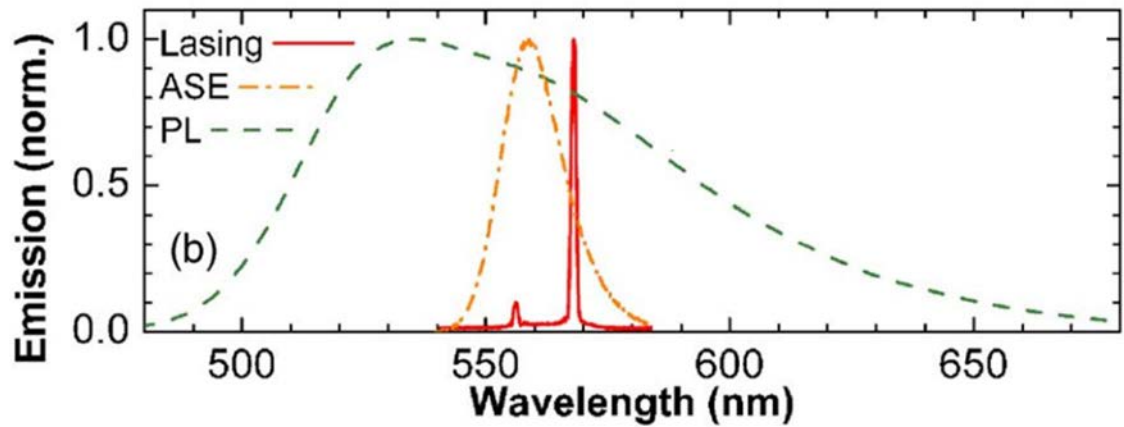


**Figure 3.1** Wavelength spectrum of photoluminescence (PL) and amplified spontaneous emission (ASE) of a gain medium, and that of laser emission upon feedback of ASE inside a laser cavity. (The figure is modified from Ref. [26])

become much narrower (e.g. 15 nm) compared to the case of PL. The feedback of ASE within a laser cavity may lead to laser emission, when the pump power exceeds the lasing threshold. The lasing peaks on the spectrum are very narrow (e.g. 0.5 nm) and the number of peaks depends on the number of modes supported within the wavelength range of ASE. Each lasing peak corresponds to a lasing mode. Some lasers give lasing spectra with only one dominant lasing peak, such as the red curve shown in Figure 3.1, these lasers are said to be single-mode.

The wavelength spectra obtained tell us about the optical characteristics of a laser. To begin with, the modal quality factor ( $Q$ ) can be calculated from the FWHM of the lasing peak ( $\Delta\lambda_0$ ) and peak wavelength ( $\lambda_0$ ) by

$$Q = \frac{\lambda_0}{\Delta\lambda_0}. \quad (3.1)$$

It is noted that  $Q$  defined here may be different from the theoretical values (e.g. Equation (2.50)), since the experimental linewidth  $\Delta\lambda_0$  is measured under optical gain, such that broadening of lasing peaks may occur. A higher  $Q$  is associated with low



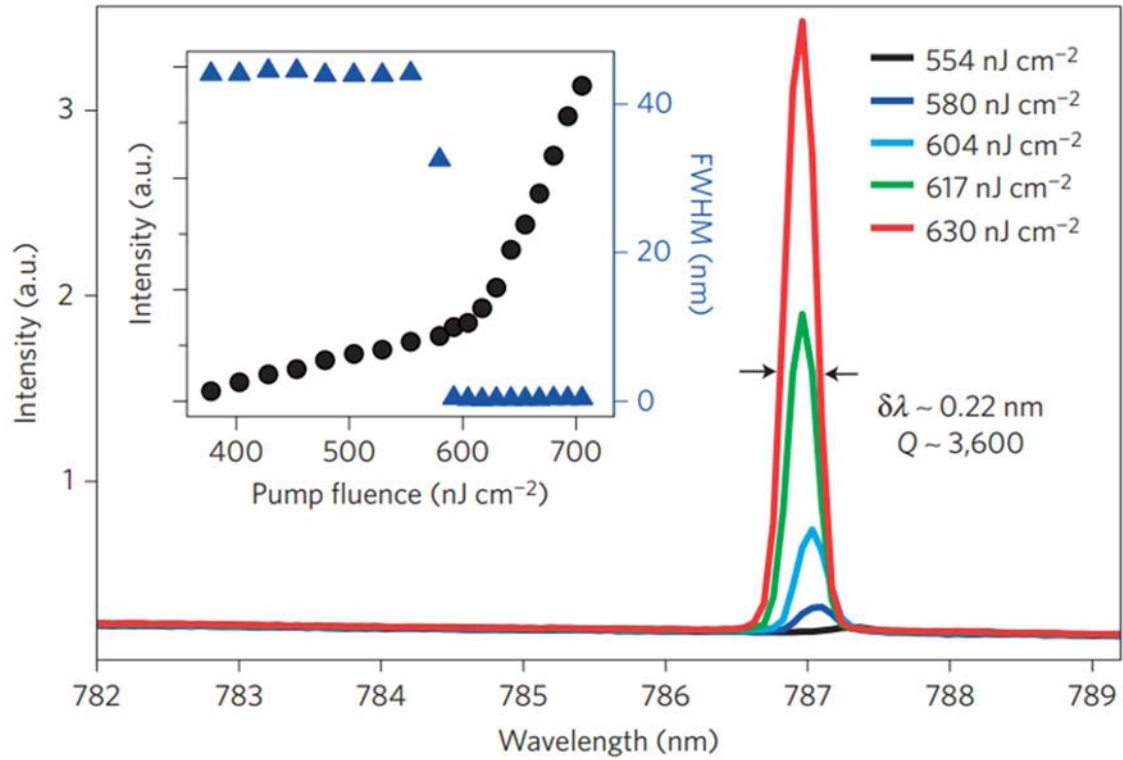


**Figure 3.2** Wavelength spectrum of a  $\text{CH}_3\text{NH}_3\text{PbI}_3$  nanowire at various levels of pump fluence (pump density). Inset: The corresponding light-light curve (black dots) and FWHM plotted against pump fluence (blue triangles). (Figure from Ref. [28])

threshold gain  $G_{\text{th}}$ , where the exact relationship depends on the optical mode being studied. Mathematically, it can be expressed as [29]

$$G_{\text{th}} = \frac{2\pi n_{\text{eff}}}{\Gamma \lambda_0 Q}, \quad (3.2)$$

where  $n_{\text{eff}}$  and  $\Gamma$  are the effective refractive index (i.e. group index) and energy confinement factor within the gain medium, respectively. Experimentally, the lasing threshold can also be found in terms of pump threshold instead of the threshold gain. This is done by plotting the relative output intensity against the pump density (i.e. light-light curve). The inset of Figure 3.2 shows the light-light curve of a certain laser cavity as an example [28], which has a kink indicating the pump threshold ( $\sim 600 \text{ nJ cm}^{-2}$ ).



This method would be adopted in the experimental part of this work in the determination of the lasing threshold.

In addition, the mode spacing (i.e. the distance between adjacent lasing peaks) of the lasing spectrum can be used to confirm the type of optical mode supported by the laser cavity. For instance, as discussed in Section 1.4, a simple Fabry-Pérot cavity supports fundamental longitudinal modes for wavelengths satisfying  $\lambda_0 = \frac{2nl}{m}$ , where  $n$  and  $l$  are the refractive index of the gain medium and cavity length parallel to the propagation direction respectively, and  $m$  is a positive integer. To confirm that the lasing emission from a lasing cavity corresponds to longitudinal modes, one may deduce the modal wavelengths theoretically according to this expression, followed by matching the results with the experimentally measured wavelength spectrum. Matching the theoretical and experimental peak wavelength values also helps to find some of the physical dimensions of the cavity, when the roundtrip length of the optical mode depends on the physical dimension concerned (e.g. cavity length  $l$  in this case).

To measure the wavelength spectrum of a light source, the emitted light should be coupled into a monochromator. A monochromator is a device which collects light from an external source as the input, and transmits light within a selected narrow wavelength range as the output. Figure 3.3 [30, 31] shows a Czerny-Turner monochromator, which directs the collimated input onto a diffraction grating and splits it into multiple light rays traveling in different directions according to their wavelengths. The angle of the diffraction grating is controlled by rotation of the turret to select a specific wavelength to be transmitted at the exit slit. In this way, the light intensity of each wavelength range can be analyzed by converting the output to a digital signal,

(a)



(b)

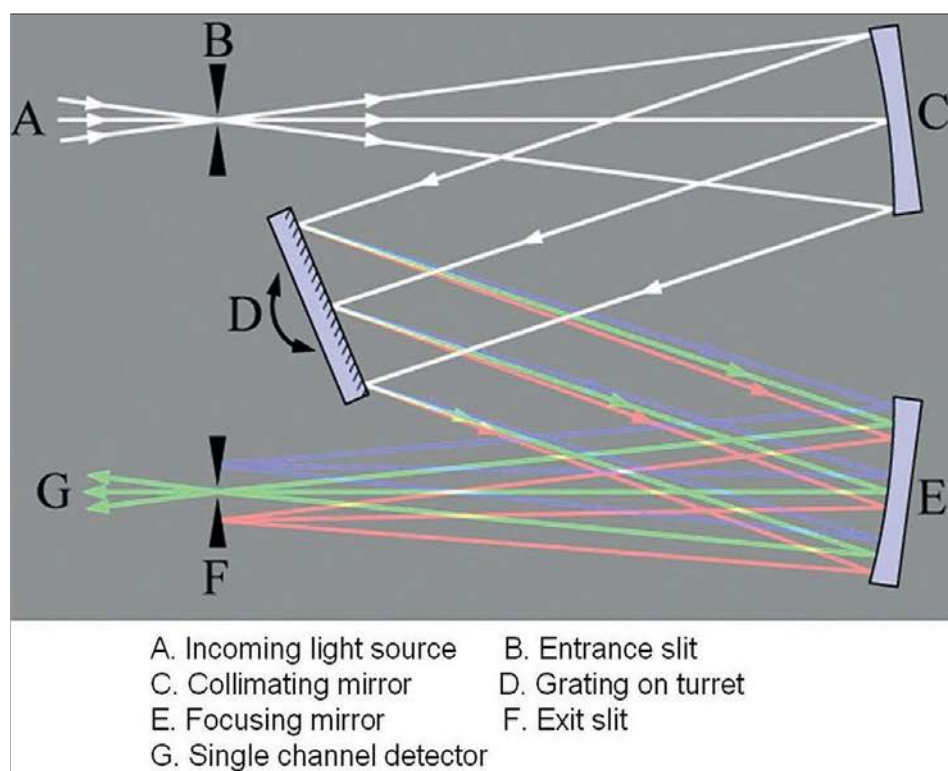


**Figure 3.3** (a) A Czerny-Turner monochromator [30] and (b) its corresponding schematic diagram [31].

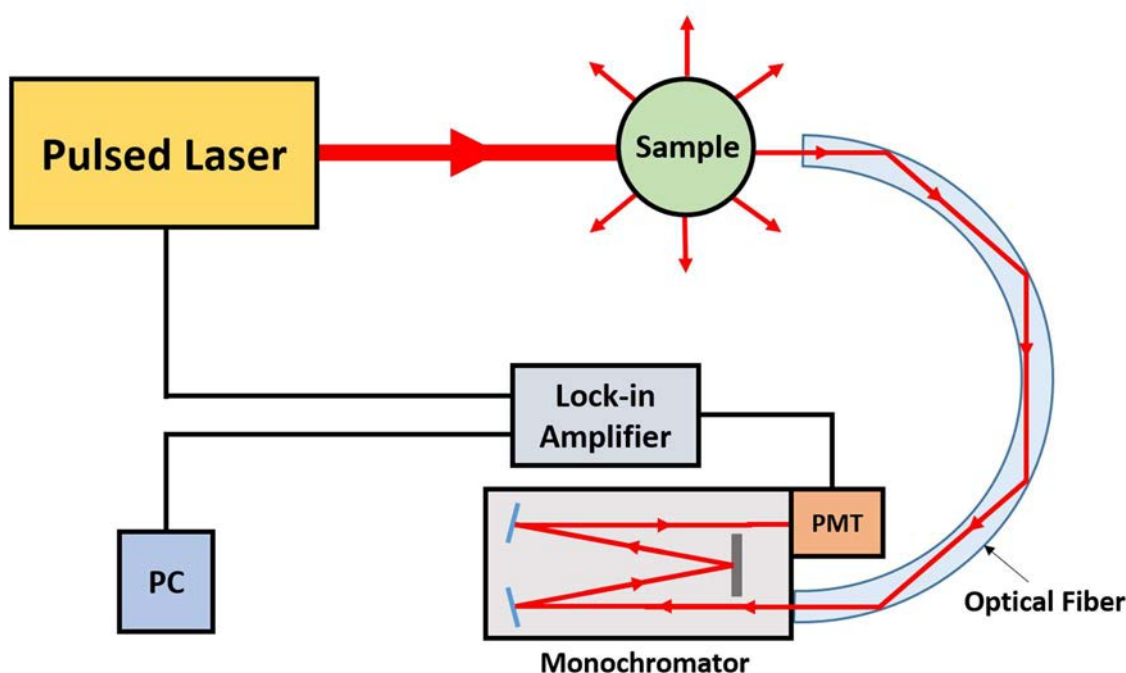


**Figure 3.4 Schematic diagram of the configuration of room temperature spectral measurement for bulk samples through pulsed laser excitation.**

forming a wavelength spectrum. For some monochromators, there is no exit slit and the output is connected to an array-type detector to measure the intensity across the whole wavelength spectrum simultaneously, such type of monochromators is also known as spectrometers.

For bulk samples, the set-up for room temperature spectral measurement can be illustrated as shown in Figure 3.4. In the set-up, an optical fiber is placed close to the sample to collect its emitted light upon excitation by the pulsed laser. The collected light is then directed into the monochromator as the input. In order to enhance the signal-to-noise ratio, the output of the monochromator can be amplified by devices such as photomultiplier tube (PMT) and lock-in amplifier. These devices require the input signal to be periodic in order to trace the frequency for amplification. The input can be made periodic either by pulsed laser excitation, or with the help of a light chopper (in the case of continuous light source). As an example, a micro quartz cuvette (with 1-mm

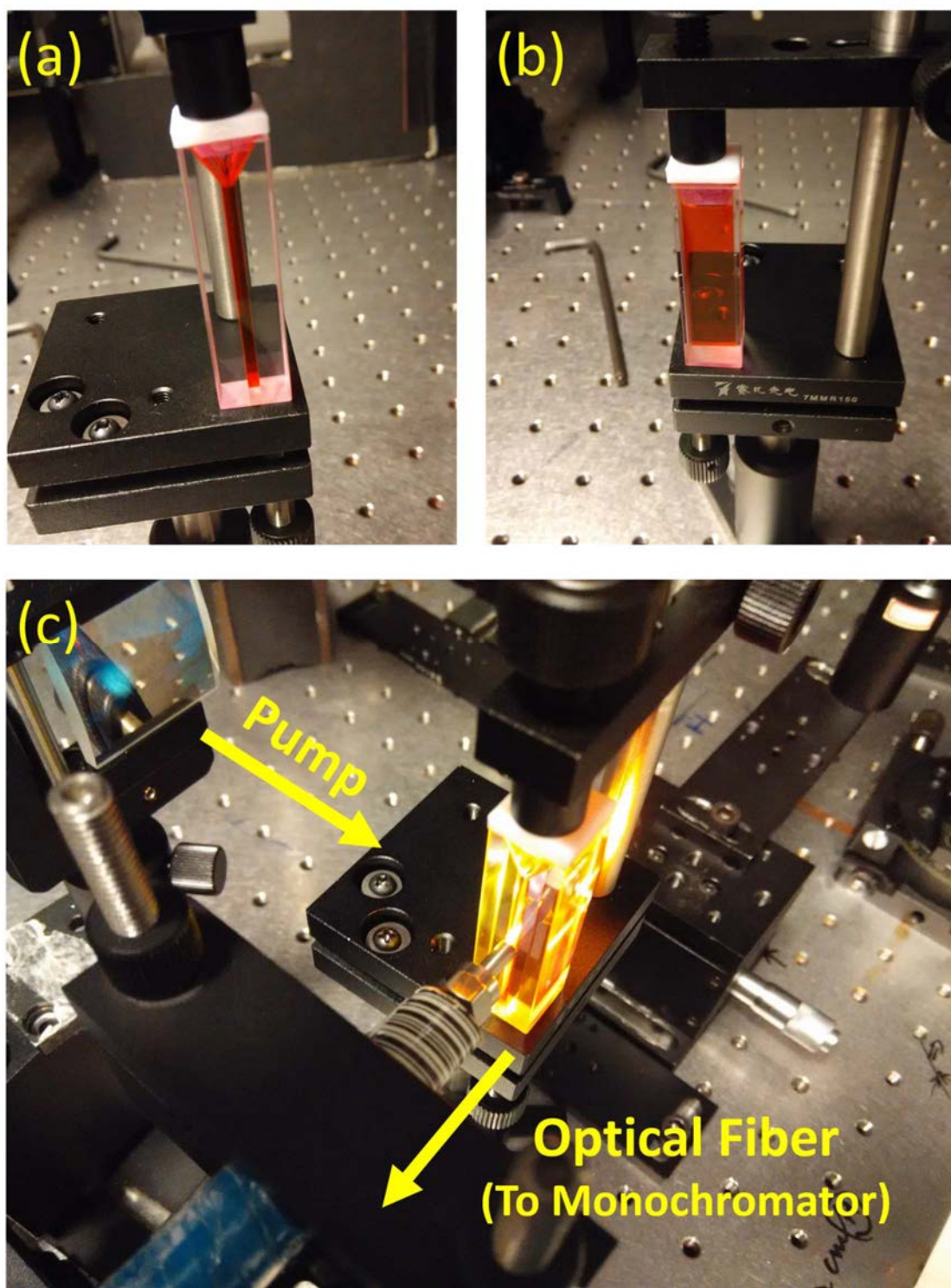


**Figure 3.5** (a) Front view and (b) side view of the micro quartz cuvette filled with rhodamine 6G (R6G) solution, and (c) the orientation of the cuvette during PL measurement of the sample.



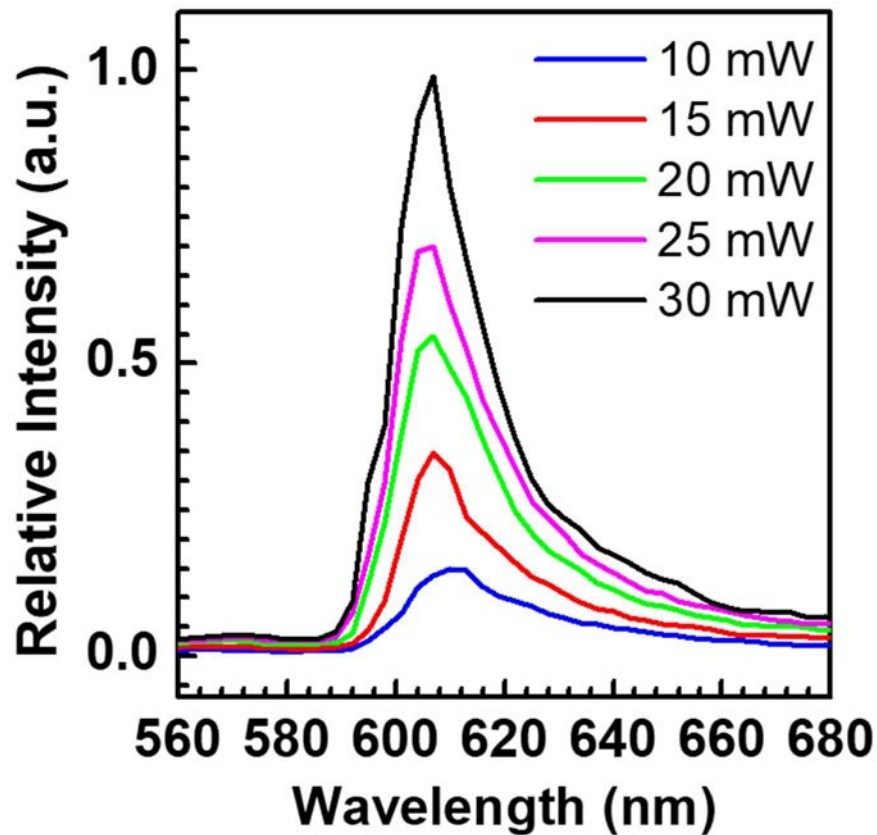


**Figure 3.6** PL spectra of the R6G solution at different pump powers.

slit) is filled with rhodamine 6G (R6G) solution as the liquid sample. The solution is then excited by horizontally focused pump pulses (generated by a cylindrical lens). The pump pulses should illuminate the cuvette from the side and the light emitted by the sample should be collected from the front, see Figure 3.5. The measured wavelength spectra of the R6G solution is shown in Figure 3.6, which shows the FWHM of the peaks is approximately 20 nm, regardless of the pump power. This corresponds to the PL of the R6G dye [32]. Similar set-up can be used for measurements of ASE and lasing spectra of bulk fluorescent materials and laser cavities, depending on the required conditions and physical dimension of the sample.

If the samples are of micro- or nano-scale, it is difficult to do the excitation

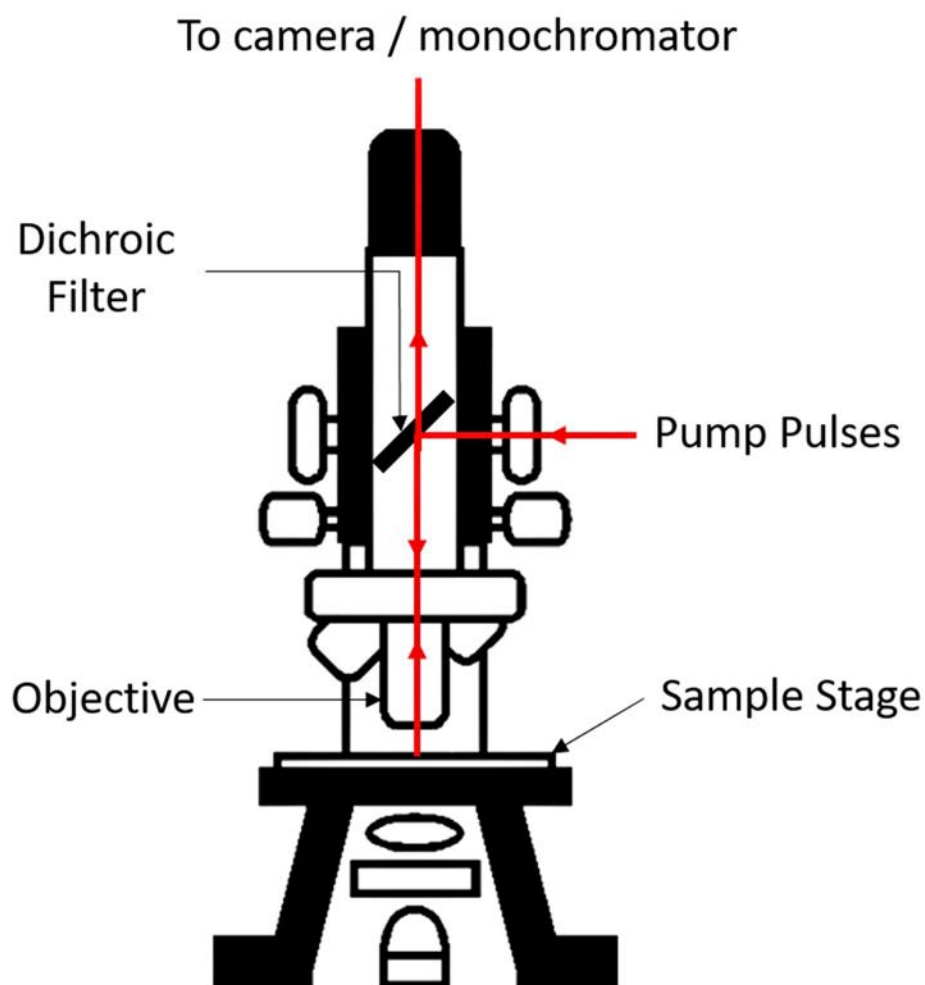


**Figure 3.7 Microscope system for spectral analysis of small samples. (Figure modified from Ref. [33])**

directly through simple optics. Moreover, their emission is usually much weaker than bulk samples, making it difficult to be detected. In this case, the emission spectra of these samples should be measured under a microscope system, which is shown in Figure 3.7. The system is formed by inserting a dichroic filter (i.e. color filter) inside an optical microscope. The wavelength range of the dichroic filter is selected, such that it reflects the incoming pump pulses, while transmitting the emission from the sample. The angle of the filter is also finely tuned in order to reflect the incoming pump pulses onto the objective lens, which is then focused onto the sample placed on the sample stage. Upon excitation, the emission from the sample would be collected at the objective lens, which

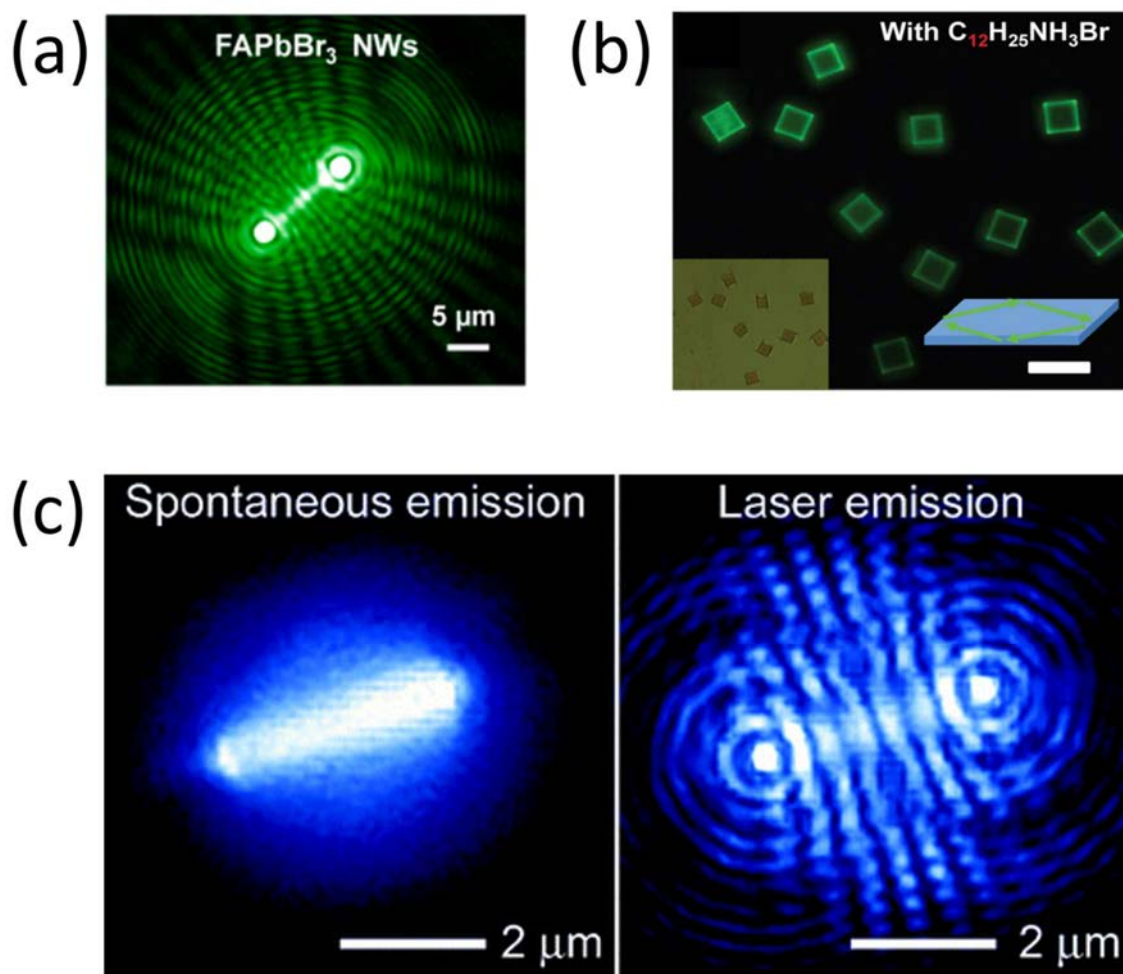


**Figure 3.8** Microscope images of (a) perovskite nanowire [34], (b) perovskite microplates [35] and (c) ZnO nanowire [36] under optical excitation.

is focused onto an optical fiber as the input to the monochromator. This system is especially advantageous for the spectral measurement of tiny samples. First, the objective lens focuses the pump pulses into a tiny spot, which is capable to excite a single small sample from a cluster without exciting any other nearby samples. Second, a camera can be installed on the microscope to finely tune the position of the spot of excitation on the sample stage, as well as taking photographs of the sample with and without excitation. See Figure 3.8 [34-36] for some examples of these photographs. It is noted that the pattern of the scattered light from a sample in the microscope images can be used to distinguish between PL and lasing emission (e.g. Figure 3.8c), as well as the





type of mode supported by the lasing cavity. (The coherent Airy pattern at both ends of a nanowire is a good indication of the Fabry-Pérot mode propagating along its length.) For measurements with controlled environmental conditions, the standard sample stage of the microscope can be replaced by the corresponding sample stage which serves the purpose, such as a vacuum-cooling stage for low-temperature measurement. A low-temperature condition helps to suppress the lasing threshold of lasing cavities [37], making it easier to achieve lasing in tiny laser cavities. More details regarding spectral analysis would be discussed in the next chapter.

### 3.2. Multiphoton Absorption and Z-scan Analysis

As mentioned in Section 1.5, a single energy transition involving an energy gap  $E$  in a gain material may be achieved by simultaneously absorbing multiple lower-energy photons with energy  $E / n$ , where  $n > 1$  is an integer (non-radiative loss is neglected). This happens when the excitation power density is sufficiently high. In lasers making use of this kind of upconversion mechanism, it is important to confirm the type of mechanism taking place, as well as to know how well the gain material absorbs the photons in order to carry out the multiphoton transition. In the following, more details on multiphoton absorption would be discussed.

Multiphoton absorption (MPA) is a nonlinear process. For example, the transition rate due to 2-photon absorption (2PA) is proportional to the square of pump intensity, instead of the pump intensity itself [38]. In other words, the absorption rate in MPA would change in a nonlinear manner as the pump intensity changes. In general, the MPA coefficients can be defined as [39]

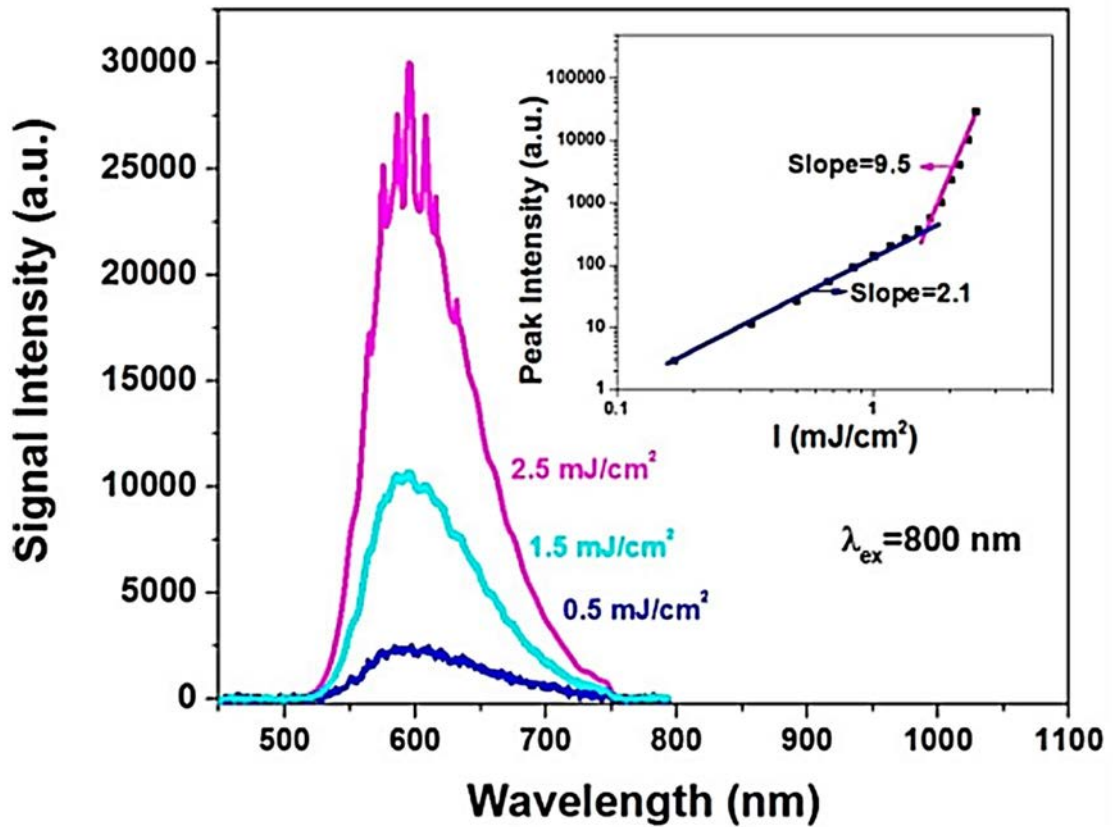


**Figure 3.9** Wavelength spectra of the emission from a crystalline polymer random laser excited at different pump powers. Inset: the corresponding light-light curve, showing that the PL regime has a slope close to 2, which confirms the spontaneous emission is induced by 2-photon absorption (2PA). (Figure from Ref. [40])

$$\frac{dI_0}{dz} = -\alpha_0 I_0 - \alpha_2 I_0^2 - \alpha_3 I_0^3 - \dots = -\alpha_0 I_0 - \sum_{n=2}^{\infty} \alpha_n I_0^n, \quad (3.3)$$

where  $\alpha_n$  ( $n = 2, 3, 4, \dots$ ) is the nonlinear  $n$ -photon absorption ( $n$ PA) coefficient, whereas  $\alpha_0$  and  $I_0$  are respectively the linear absorption coefficient corresponding to one-photon absorption and the irradiance (i.e. optical pump intensity).  $z$  is the propagation distance within the sample. In many cases, excitation with a virtually monochromatic light from a pulsed laser supports a single dominant mechanism  $n$ PA, while suppressing other absorption schemes. If we assume the upconversion type is pure, i.e. due to one mechanism  $n$ PA, Equation (3.3) can be simplified into [41]

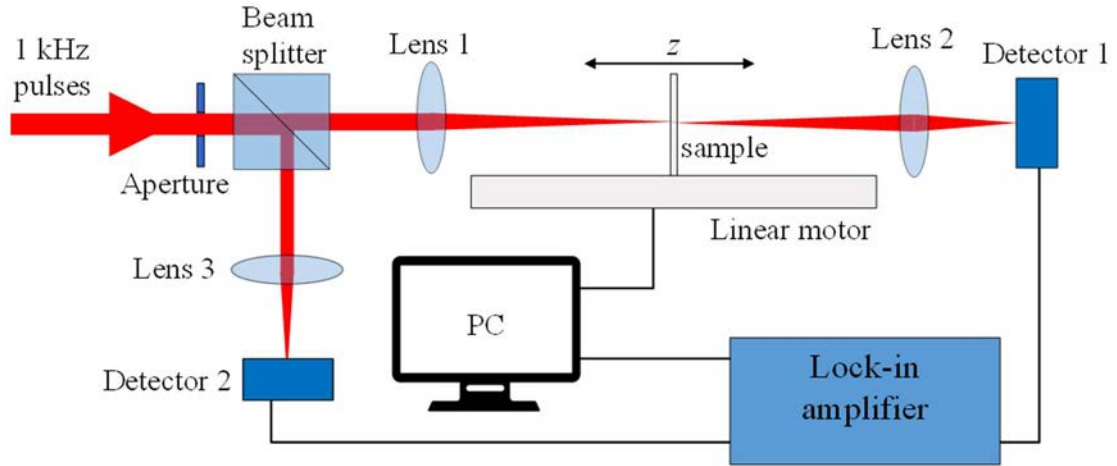


**Figure 3.10** Configuration of the open-aperture z-scan technique.

$$\frac{dI_0}{dz} = -\alpha_n I_0^n. \quad (3.4)$$

Therefore, an upconversion due to pure  $n$ PA can be confirmed experimentally by plotting the light-light curve (in log-log scale) in the PL regime and obtaining a slope close to  $n$ , because  $\log(I_0) = n \log(I_{\text{PL}}) + C$  according to Equation (3.4), where  $I_{\text{PL}}$  is the peak PL intensity and  $C$  is a constant. The inset of Figure 3.9 [40] shows an example of this technique, where a slope close to 2 is obtained from the light-light curve, suggesting that the emission of the material is 2PA-induced.

For the same material, MPA of higher orders requires much more pump intensity to obtain the same amount of PL emission. For this reason, it is very important to have a gain material with a high MPA coefficient at the pumping wavelength. Experimentally, it is possible to determine the MPA coefficient for a pure upconversion process by the open-aperture z-scan technique, in which the configuration is shown in Figure 3.10. As shown in the set-up, an aperture is used to produce a pumping beam with circular laser spot of known diameter, and is then split into two identical beams. One of the beams is focused onto the thin sample (e.g. 1 mm) placed on a linear

translation stage moving parallel to the pumping beam (i.e.  $z$ -direction), which is then focused onto Detector 1. Another beam is focused directly onto Detector 2 as the reference. By measuring the intensity ratio of the two split beams at the detectors, one may determine the normalized transmittance  $T_{nPA}$  of the sample. Under the set-up of this  $z$ -scan technique,  $T_{nPA}$  at position  $z$  can be theorized as [39]

$$T_{nPA}(z) = \frac{1}{\Lambda} \int_{-\infty}^{\infty} {}_2F_1 \left[ \frac{1}{n-1}, \frac{1}{n-1}, \frac{n}{n-1}, -\psi_n^{n-1} h^{n-1}(t) \right] \times h(t) dt, \quad (3.5)$$

where

$$\psi_n = \frac{\Psi_n}{1 + \left( \frac{z^2}{z_0^2} \right)}, \quad (3.6)$$

with

$$\Psi_n = \left[ (n-1) \alpha_n I_0^{n-1} L_{\text{eff}}^{(n)} \right]^{1/(n-1)} \quad (3.7)$$

being the on-axis peak phase shift of  $n$ -photon absorption, and

$$L_{\text{eff}}^{(n)} = \frac{1 - \exp[-(n-1) \alpha_0 L]}{(n-1) \alpha_0} \quad (3.8)$$

is the effective sample length corresponding to  $n$ PA. In the formulation,  $L$  is the sample length, and  $z_0 = \pi \omega_0^2 / \lambda_0$  is the diffraction length of the Gaussian beam, where  $\omega_0$  and  $\lambda_0$  is the beam waist radius and wavelength, respectively.  ${}_2F_1$  is the hypergeometric function,  $h(t) = \exp(-t^2)$  and  $\Lambda = \pi^{1/2}$  for Gaussian pulse profile. In our work,  $z$ -scan technique on pure 2PA and pure 3PA are involved, in which their transmittances can be deduced from Equation (3.5) as follows:

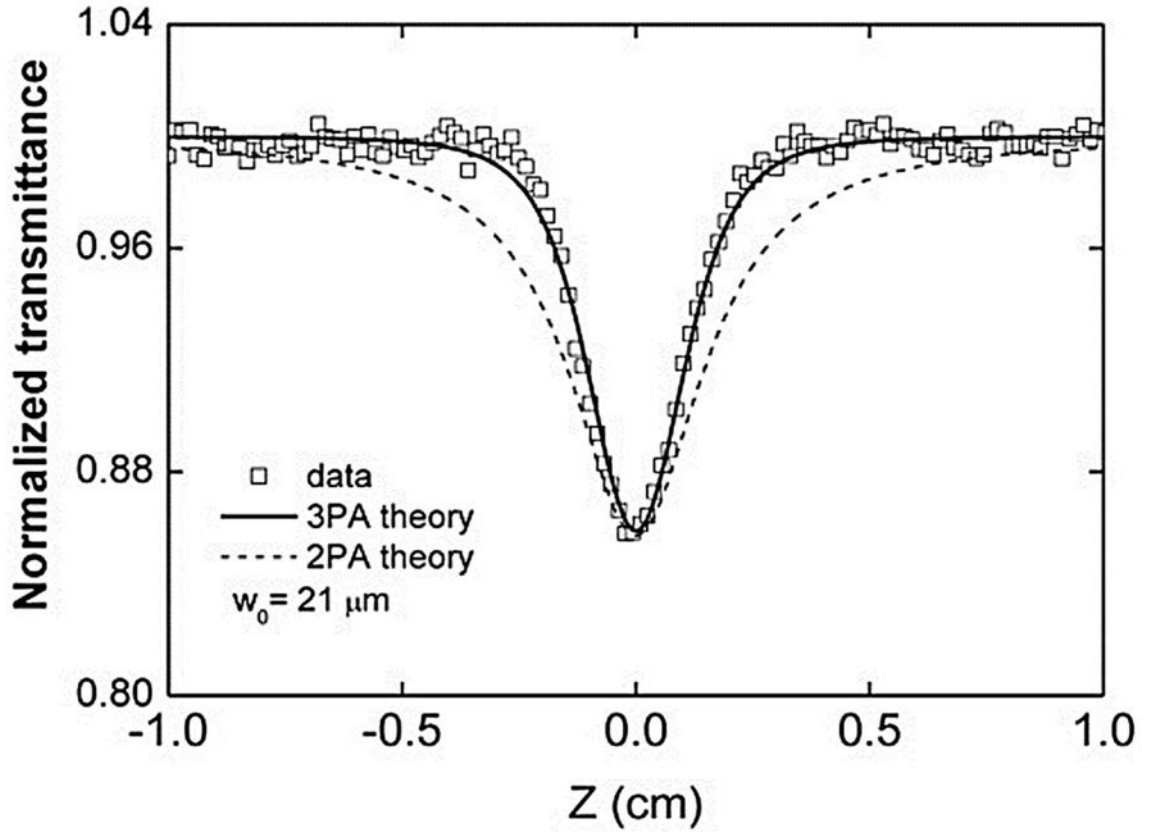


**Figure 3.11** Experimental open-aperture z-scan signature of a platinum acetylide complex, with the corresponding fitted curves for 2PA and 3PA. (Figure from Ref. [42])

$$T_{2PA} = \frac{1}{\Lambda \psi_2} \int_{-\infty}^{+\infty} \ln[1 + \psi_2 h(t)] dt, \quad (3.9)$$

$$T_{3PA} = \frac{1}{\Lambda \psi_3} \int_{-\infty}^{+\infty} \ln \left\{ \left[ 1 + \psi_3^2 h^2(t) \right]^{1/2} + \psi_3 h(t) \right\} dt. \quad (3.10)$$

By measuring  $T_{2PA}$  and  $T_{3PA}$  at different positions  $z$ , one may plot a  $T_{nPA}$ - $z$  curve, which can be fitted by Equations (3.9) and (3.10) to determine  $\alpha_2$  and  $\alpha_3$ . In our convention, we define the focal point at  $z = 0$ , where the excitation beam on the sample is the most focused. It is expected that  $T_{nPA}$  is the lowest at this position because the high beam intensity triggers large nonlinear absorption. On the other hand, positions further away from the central position should yield higher  $T_{nPA}$ . A typical z-scan result from Vivas et



al. [42] on a sample supporting 3PA is shown in Figure 3.11, which is theoretically a symmetric curve with the minimum value at  $z = 0$ . Furthermore, the corresponding curve fitting results show that the 3PA curve fits much better than the 2PA one, implying that 3PA is the dominant absorption mechanism in the sample. Therefore, other than finding the MPA coefficient, curve fitting can also be used to confirm the dominant absorption type.

### 3.3. Conclusion

Various types of emission can be collected when a laser cavity is excited. In particular, measurement of the lasing spectrum can be useful in extracting useful parameters corresponding to the performance of the laser, including quality factor and lasing threshold. The lasing mechanism can also be confirmed by matching the theoretical mode spacing with the measured lasing spectrum. For multiphoton excitation, the pumping mechanism can be verified either by the slope of light-light curve under log-log scale in the PL regime, or by z-scan analysis. In addition, z-scan analysis also helps to determine the multiphoton absorption coefficients through curve fitting.



## 4. Multiphoton Excitation of Single-crystalline CsPbCl<sub>3</sub> Micro-cavities

In the first experimental part of this work, single-crystalline CsPbCl<sub>3</sub> microplates were fabricated and studied as an example of upconversion plasmonic lasers in full detail. The experimental techniques mentioned in Chapter 3 would be applied to our work.

### 4.1. Background

Halide perovskites exist in the form of ABX<sub>3</sub> (Figure 4.1 [43]), which is a very popular fluorescent material for optical devices in the recent decade. In particular, researchers have been investigating solar cells based on hybrid organic-inorganic halide perovskite (e.g. CH<sub>3</sub>NH<sub>3</sub>PbX<sub>3</sub>, X = I, Br, Cl) extensively [44-46], since the semiconducting material has exceptional optical performance, including high optical absorption coefficient and long carrier diffusion length, while the solution-processed fabrication cost is low. Moreover, the organometal halides have low defect density and high optical gain ( $> 10^4 \text{ cm}^{-1}$ ) [47], making them potential candidates for applications in high-performance miniaturized optoelectronic devices, including low-threshold nanolasers and high-power microcavity lasers [28, 48, 49]. However, the downside of these materials is their relatively low stability in air, in which the material composition would be easily affected because of the degradable organic cations with the presence of air moisture [50]. To overcome this problem, recent researches have been focusing on the inorganic version of the halide perovskites, e.g. cubic lattice cesium lead halides (CsPbX<sub>3</sub>, X = I, Br, Cl) for optoelectronic device applications due to their higher

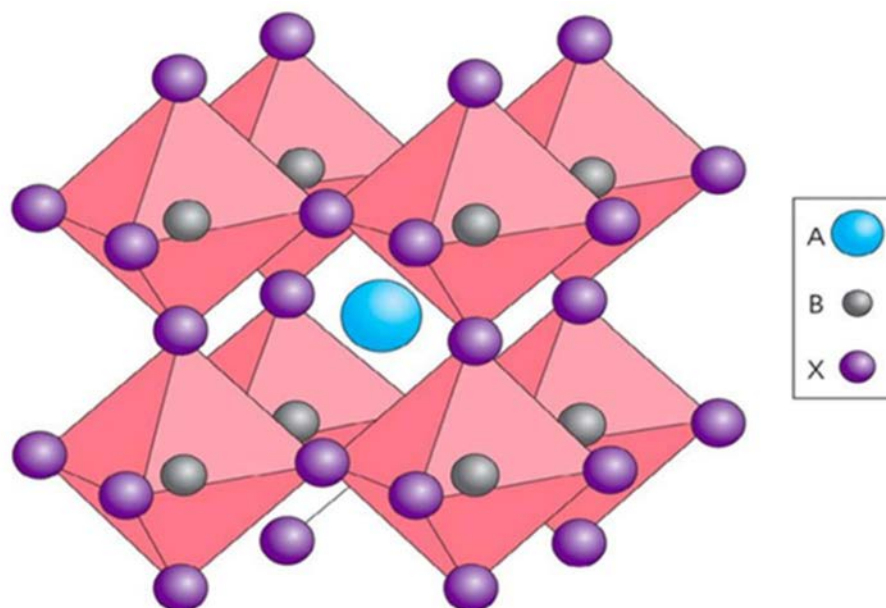


**Figure 4.1 Crystal structure of halide perovskite. (Figure from Ref. [43])**

stability in moisture compared to the hybrid halides [51]. It is found that CsPbX<sub>3</sub> supports tunable lasing emission at wavelengths ranging from ultraviolet to near-infrared regime through direct bandgap excitation (i.e. downconversion), in the form of nanocrystals, nanowires and nanoplates [52-56]. For nonlinear optical characteristics, 2- and 3-photon absorption (2PA and 3PA) [57], 3PA-induced amplified spontaneous emission (ASE) [57] and 2PA-induced lasing emission [58] have been realized. These results were mainly reported based on nano-scale structures with strong quantum confinement of carriers.

Since most of the reports on nonlinear optical characteristics of CsPbX<sub>3</sub> devices were based on nano-structures, it would be interesting to know whether it is possible to demonstrate these characteristics from micro-structures with weaker quantum confinement effect. Therefore, the experiment has been designed to study 2PA and 3PA of single-crystalline CsPbCl<sub>3</sub> square microplates, as well as the corresponding ASE and the lasing characteristics induced by these absorption schemes at low-temperature [10].





## 4.2. Synthesis and Characterization of CsPbCl<sub>3</sub> Microplates

The CsPbCl<sub>3</sub> microplates were obtained by the reaction between CsCl and PbCl<sub>2</sub> in  $\gamma$ -Butyrolactone (GBL) as the solvent. To synthesize the sample, 10 ml of GBL (99.9%) was first heated to 70 °C in nitrogen inside a 50-ml 3-neck flask. After reaching the target temperature, 1 mmol PbCl<sub>2</sub> (99.9%) and 1 mmol CsCl (99.9%) were added into the flask for reaction. It is noted that the reactants were added one before another in this step. PbCl<sub>2</sub> was first added into the heated GBL with magnetic stirring for 15 minutes, followed by CsCl with magnetic stirring for 1 hour. This helps to dissolve the reactants, as well as mixing them up more evenly. After the reaction, the resulting solution was dried at 70 °C in an electric oven with Ar gas flow as protection. The residue after drying contains clusters of single-crystalline CsPbCl<sub>3</sub> microplates, which should be washed in order to remove the extra CsCl in the solution and any surfactant on the microplates' surfaces. This is done by washing the residue in absolute ethanol for about 4 times. Each time after washing, the microplates were re-dispersed and shaken manually for 2 minutes, followed by centrifugation. Each time after centrifugation, the supernatant (i.e. the liquid above the sediment) was discarded. After washing, the microplates were separated from each other by ultrasonic treatment in cyclohexane.

Various kinds of characterization were performed regarding the synthesized CsPbCl<sub>3</sub> microplates. To start with, scanning electron microscope (SEM) images of the sample (dispersed on a quartz slide through drop casting with cyclohexane) were taken in different magnifications, as shown in Figure 4.2a. From the images, both microplate clusters and single microplates can be observed. The majority of the microplates were of

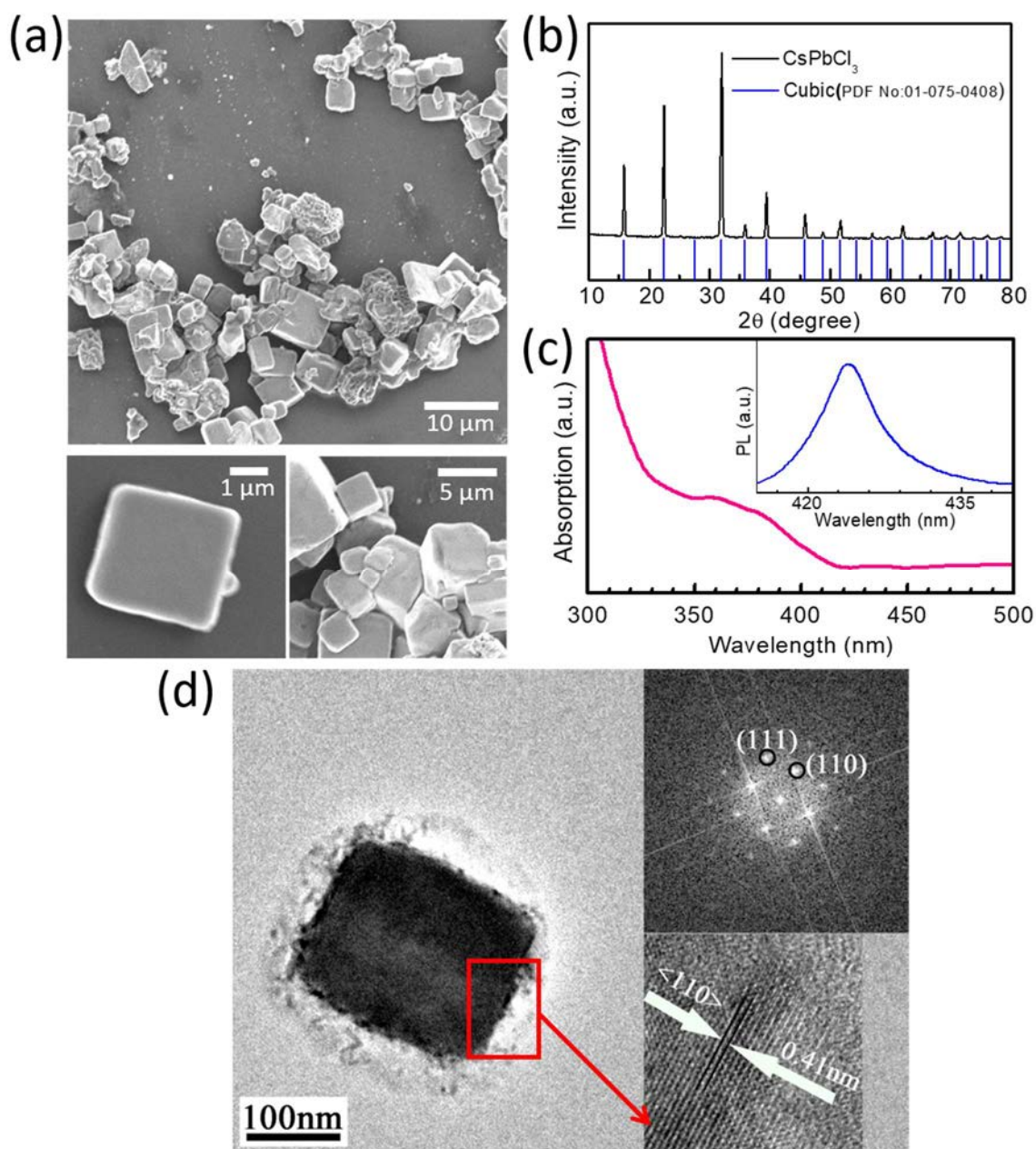


**Figure 4.2** (a) Scanning electron microscope (SEM) images, (b) X-ray diffraction (XRD) pattern, (c) photoluminescence (PL)/absorption spectra of the CsPbCl<sub>3</sub> microplates. The PL is obtained from linear excitation using 355-nm photons; (d) Tunneling electron microscope (TEM) images, and the corresponding selected area electron diffraction (SAED) pattern of a single CsPbCl<sub>3</sub> microplate.



square shapes with side lengths ( $W$ ) ranging from  $\sim 2$  to  $\sim 10$   $\mu\text{m}$ . The corresponding X-ray diffraction (XRD) pattern of the sample is shown in Figure 4.2b, which shows that the synthesized microplates were of cubic lattice structure. Furthermore, Figure 4.2c shows the absorption spectrum and the photoluminescence (PL) spectrum at 355-nm excitation (1-photon excitation). The peak PL wavelength was found to be  $\lambda \sim 425$  nm. To confirm that the microplates were single-crystalline, tunneling electron microscope (TEM) and selected area electron diffraction (SAED) images of a single microplate were taken, see Figure 4.2d. The single microplate was found to have an interplanar spacing of 0.41 nm, which corresponds to the characteristic spacing of CsPbCl<sub>3</sub> in the (110) planes (JCPDS:75-0408). In addition, well-defined spots can be observed from the corresponding SAED pattern. The two images provided strong evidence that the synthesized CsPbCl<sub>3</sub> microplates were single-crystalline.

### 4.3. Nonlinear Absorption, PL, and ASE of Multiphoton-excited CsPbCl<sub>3</sub> Microplate Clusters

To pump the sample optically, a Coherent Libra Ti-sapphire pulse laser and an optical parametric amplifier (OPA) were used to produce the femtosecond pump pulses (50 fs, 1 kHz). The pump pulses were directed into a microscope system (see Figure 3.7 in the previous chapter) and were focused onto the CsPbCl<sub>3</sub> microplates placed inside a vacuum-cooling stage by the 10 $\times$  objective lens of the microscope. The measured diameter of the circular pump spot under the microscope image was  $\sim 10$   $\mu\text{m}$ . Furthermore, the temperature ( $T$ ) of the sample was cooled down to 83 K during optical measurement, which was the lowest achievable temperature supported by the vacuum-



cooling stage used in the experiment. In this way, the non-radiative recombination rate of the microplates during optical excitation could be minimized. In addition, the pressure inside the vacuum-cooling stage was also lowered to  $10^{-3}$  mbar to prevent condensation of air moisture and ice formation around the sample at such a low temperature. The emission from the sample would be focused by the same  $10\times$  objective lens into a VIS-NIR optical fiber (QP1000-2-VIS-NIR from Ocean Optics with  $1000\ \mu\text{m}$  core diameter and 2 m length), in which the optical signal was coupled to a monochromator (Princeton SpectraPro 2750 integrated with a ProEM EMCCD camera with spectral resolution less than 0.1 nm) for spectral analysis.

800-nm and 1280-nm pump pulses were generated for 2-photon and 3-photon excitation of the CsPbCl<sub>3</sub> microplates at  $T = 83\ \text{K}$ . The 800-nm pulses were obtained directly from the Ti-sapphire pulsed laser, while the 1280-nm pulses were obtained by feeding the 800-nm pulses into the OPA. The pump wavelengths ( $\lambda_0$ ) were chosen such that optimal PL intensity from the sample was obtained in each of the pumping schemes. Figure 4.3a (Figure 4.3b) shows the emission spectra of the CsPbCl<sub>3</sub> microplate clusters induced by 2PA (3PA) at different pump densities, with the corresponding peak intensity and full-width at half-maximum (FWHM) plotted in Figure 4.3c (Figure 4.3d). As the pump density increases, the results show that the FWHM of the emission spectra undergoes a sudden drop from  $\sim 9\ \text{nm}$  to  $\sim 3\ \text{nm}$  at a pump density of  $\sim 25\ \text{mJ cm}^{-2}$  ( $\sim 96\ \text{mJ cm}^{-2}$ ), with a rapid increase in peak intensity. This phenomenon corresponds to the transformation from PL to ASE emission when the excitation power density is high enough to achieve population inversion.

To confirm pure 2PA (3PA) was supported by the microplate clusters at 800-nm (1280-nm) excitation, the light-light curve in the PL regime was plotted in log-log scale,

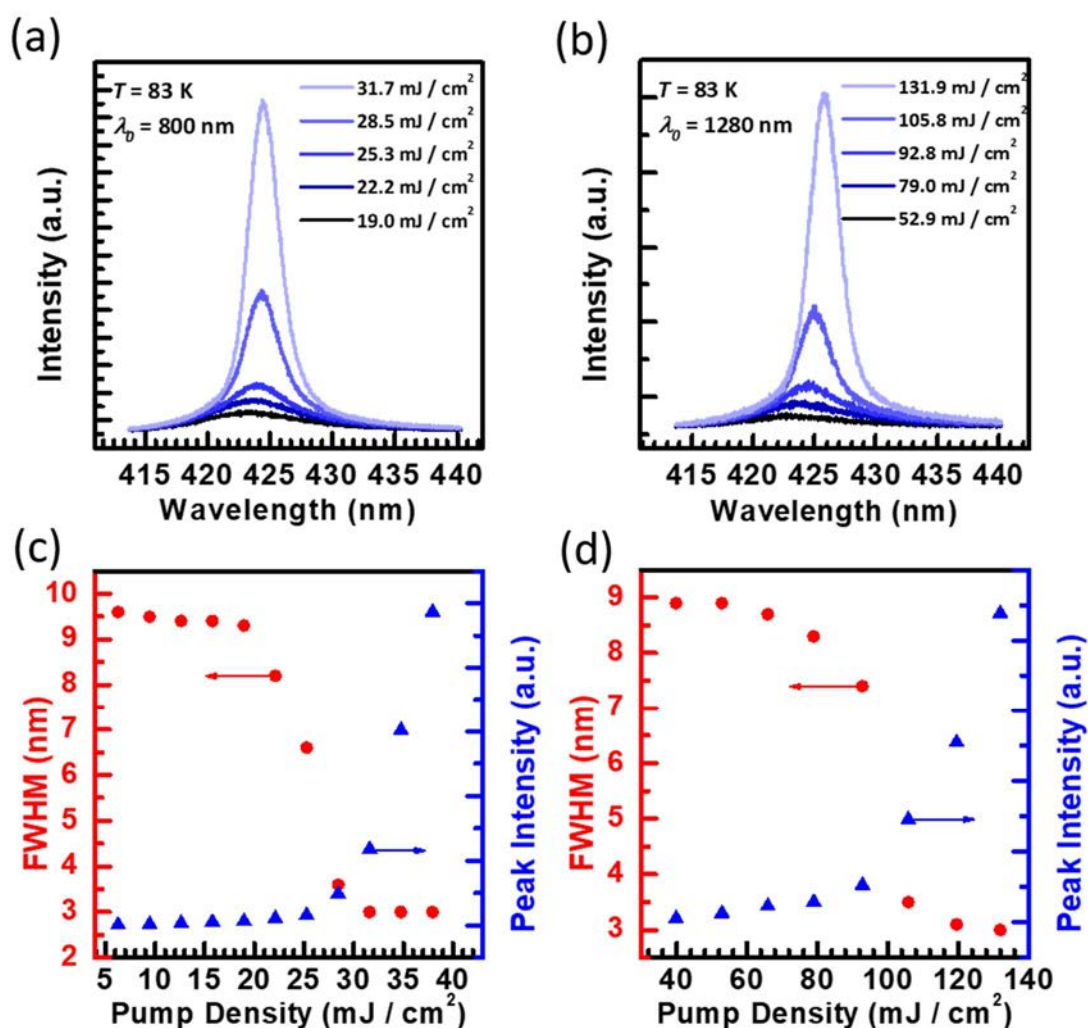


**Figure 4.3** (a) Emission spectra, (c) linewidth and light-light curve of the CsPbCl<sub>3</sub> microplate clusters under 800-nm excitation at different pump densities; (b) emission spectra, (d) linewidth and light-light curve of the CsPbCl<sub>3</sub> microplate clusters under 1280-nm excitation at different pump densities. All measurements are taken at temperature  $T = 83$  K.

as shown in Figure 4.4a (Figure 4.4b), in which a slope of  $\sim 2$  ( $\sim 3$ ) is obtained. Moreover, the room-temperature z-scan analysis was performed on the microplates. The configuration of the experiment can be found in Figure 3.10 of the previous chapter. As shown in Figure 4.4c (Figure 4.4d), a theoretical model of the normalized z-scan transmittance for pure 2PA (3PA) (See Equation (3.9) and (3.10) of the previous chapter) fitted well with the experimental z-scan data at 800-nm (1280-nm) excitation



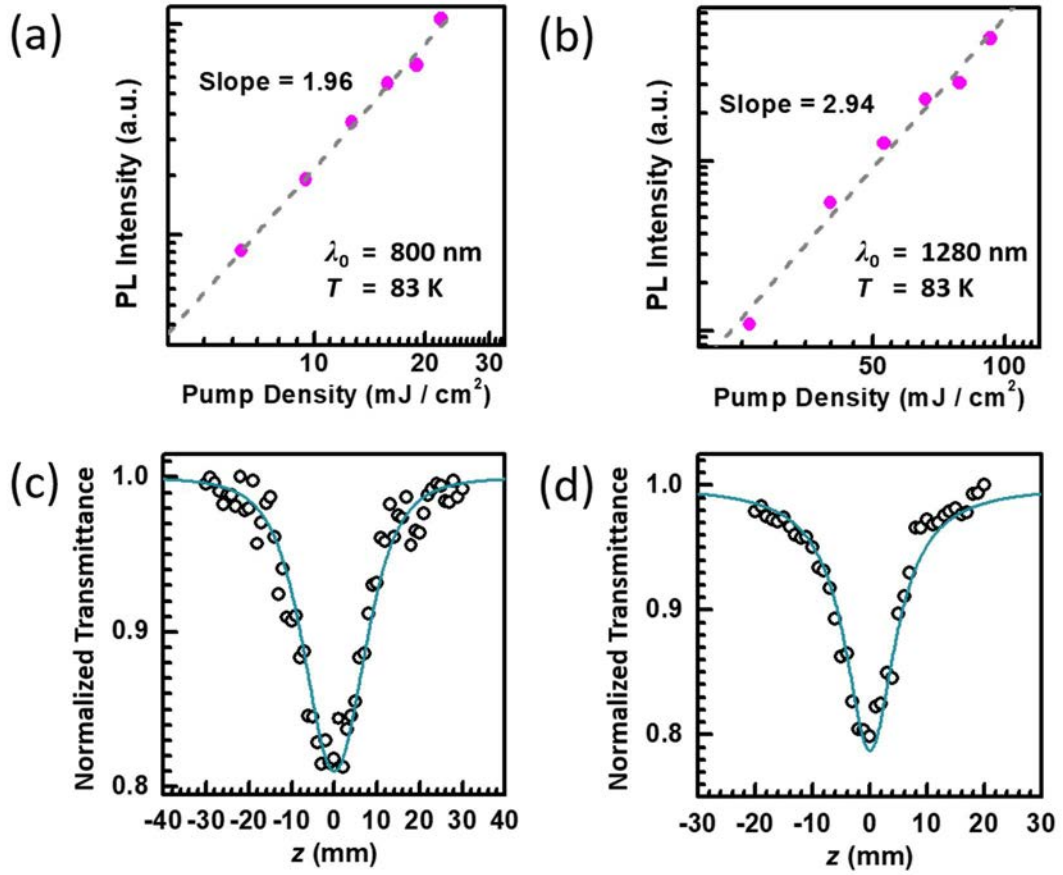


**Figure 4.4** (a) Light-light curve in the PL regime under log-log scale and (c) z-scan data of the CsPbCl<sub>3</sub> microplate clusters under 800-nm excitation; (b) light-light curve in the PL regime under log-log scale and (d) z-scan data of the CsPbCl<sub>3</sub> microplate clusters under 1280-nm excitation. The measurement of the light-light curves is taken at  $T = 83$  K, whereas that of the z-scan data is taken at room temperature  $T = 298$  K.

wavelength, confirming that light absorption by the microplates was mainly due to 2PA (3PA). The corresponding multiphoton absorption coefficient of the fitted curve is  $\alpha_2 = 8.0 \times 10^{-3} \text{ cm GW}^{-1}$  ( $\alpha_3 = 2.1 \times 10^{-5} \text{ cm}^3 \text{ GW}^{-2}$ ). The deduced multiphoton absorption coefficients are compatible with those of the materials used in optical imaging applications [59, 60].

#### 4.4. Lasing Characteristics of Multiphoton-excited CsPbCl<sub>3</sub> Microplates

In addition to the excitation of the CsPbCl<sub>3</sub> microplate clusters, single microplates were also optically excited at 800 and 1280 nm under 83 K in order to study their lasing characteristics induced by 2PA and 3PA, respectively. In this part, a 50× objective lens was used in the microscope system to focus the pump pulses into a spot of  $\sim 2 \mu\text{m}$  in diameter. Here, a single microplate with large side length ( $W \sim 8.9 \mu\text{m}$ ) was chosen for multi-mode lasing. Figure 4.5a and Figure 4.5c shows the emission spectra of this microplate under 800-nm and 1280-nm excitation, respectively. It was found that both excitation schemes supported multi-mode lasing of the microplate at emission wavelength  $\lambda \sim 425 \text{ nm}$  when the pump density exceeded the pump threshold (lasing threshold). From Figure 4.5b and Figure 4.5d, it was found that the pump threshold of 2PA- and 3PA-induced lasing in this particular microplate was  $\sim 25 \text{ mJ cm}^{-2}$  and  $\sim 123 \text{ mJ cm}^{-2}$ , respectively. Moreover, the result suggested that the FWHM of the lasing modes ( $\sim 0.41 \pm 0.02 \text{ nm}$ ), as well as the mode spacing  $\Delta\lambda$  between the lasing peaks, were the same for both excitation schemes, because these parameters were mainly dependent on the physical shape and properties of the CsPbCl<sub>3</sub> microplate, but not the pumping schemes.

The side length of a microplate  $W$  determines the roundtrip length  $L (= 2\sqrt{2} \times W)$  of the whispering-gallery modes (WGMs), which determines  $\Delta\lambda$ . If the quantum confinement effect is neglected, the relationship between these parameters can be expressed as [53, 61]

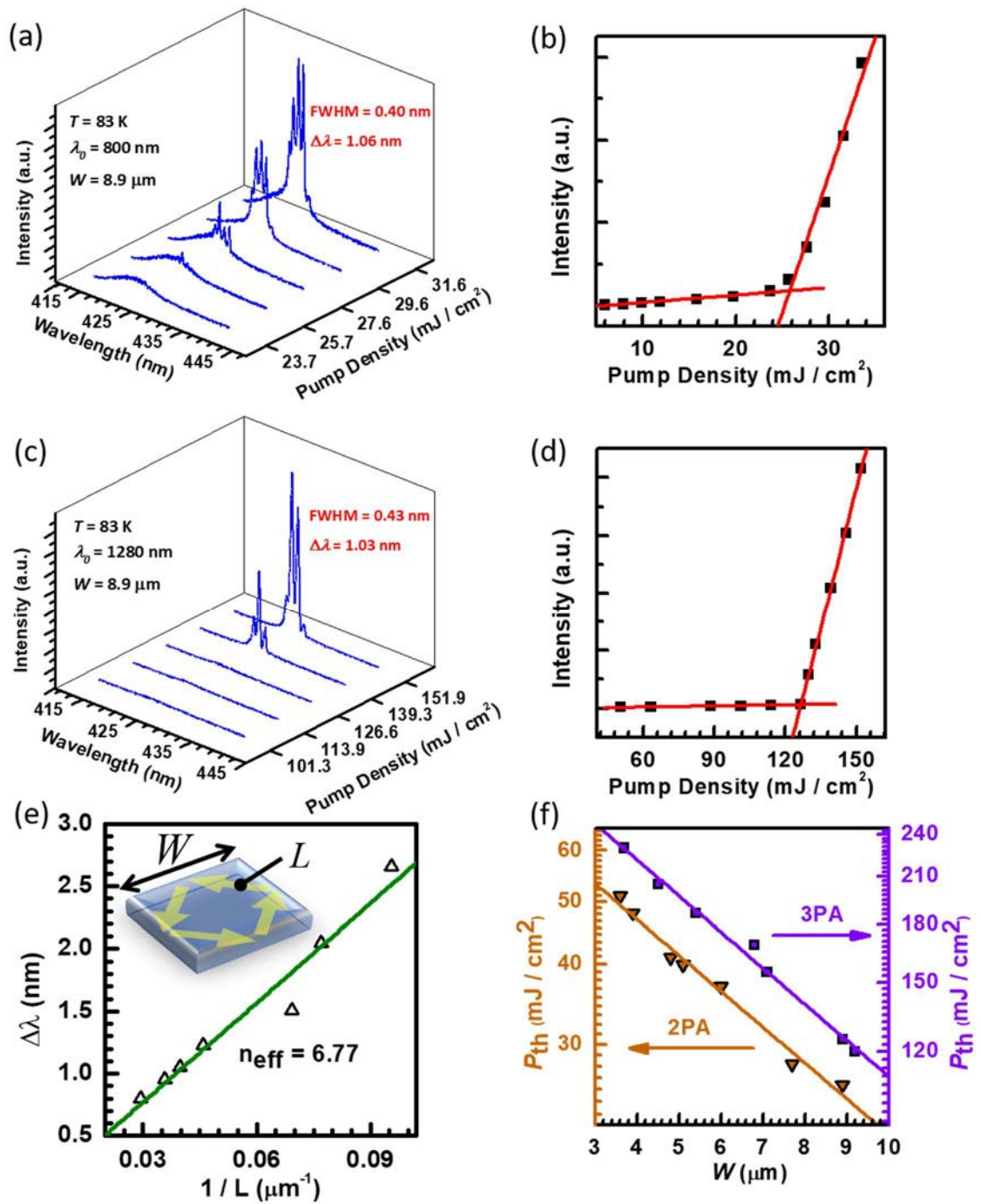


**Figure 4.5** (a) Emission spectra and (b) light-light curve of a CsPbCl<sub>3</sub> microplate ( $W = 8.9$   $\mu$ m) under 800-nm excitation at 83 K; (c) emission spectra and (d) light-light curve of a CsPbCl<sub>3</sub> microplate ( $W = 8.9$   $\mu$ m) under 1280-nm excitation at 83 K; (e) plot of  $\Delta\lambda$  versus  $1/L$  obtained from the CsPbCl<sub>3</sub> microplates with different  $W$ . (f) Semi-log plot of  $P_{\text{th}}$  versus  $W$  of the CsPbCl<sub>3</sub> microplates under 800-nm and 1280-nm excitation at 83 K.



$$\Delta\lambda = \frac{\lambda^2}{L} \left[ n - \lambda \left( \frac{\partial n}{\partial \lambda} \right) \right]^{-1} \equiv \frac{\lambda^2}{n_{\text{eff}} L} \quad (4.1)$$

where  $n$  ( $\sim 2.1$ ) is the real-part bulk refractive index of CsPbCl<sub>3</sub> [62] and  $n_{\text{eff}}$  is the effective refractive index (i.e. group refractive index) of the lasing mode. According to Equation (4.1), by exciting single microplates of different side lengths  $W$  (with any excitation scheme), one may plot  $\Delta\lambda$  against  $1/L$  to calculate  $n_{\text{eff}}$  from the slope of the curve ( $=1/n_{\text{eff}}$ ). This plot is shown in Figure 4.5e, in which the data were the mixed result from both 2PA- and 3PA-induced lasing. The results show that  $n_{\text{eff}} = 6.77$  was found to be independent of the excitation scheme, all of the data points were well fitted by a single straight line corresponding to the same slope, regardless of the type of absorption that induced the lasing. It is noted that the experimental value of  $n_{\text{eff}}$  was 3 to 4 times greater than the bulk refractive index of CsPbCl<sub>3</sub>. It is believed that the high group index was contributed by two parts. First, in Equation (4.1), the dispersive term  $-\lambda_0 \left( \frac{\partial n}{\partial \lambda_0} \right)$  was found to be  $\sim 1.0$  using the data provided in Ref. [62], which approximately gave an extra 50% increment in  $n_{\text{eff}}$  when compared to  $n$ . Second, the further increment in  $n_{\text{eff}}$  was possibly contributed by the quantum confinement effect, which was reported by other researchers on halide perovskites lasers of similar physical dimensions [35, 54]. The pump thresholds ( $P_{\text{th}}$ ) of the single microplates were also measured and plotted against their side lengths  $W$  in semi-log scale. The results can be found in Figure 4.5f. It can be seen that straight lines were obtained from the data for excitations via both 2PA and 3PA, confirming that  $P_{\text{th}} \propto \exp(-BW)$ , where  $B$  ( $\sim 1.266 \times 10^3 \text{ cm}^{-1}$ ) is a constant corresponding to scattering and absorption loss in the



microplates. It is noted that both lines in Figure 4.5f have the same slope, which is within our expectation that  $B$  is independent of the excitation scheme, because the optical loss of the lasing modes corresponds to the lasing wavelength  $\lambda$ , and is independent of the pump wavelength  $\lambda_0$ .

Another single CsPbCl<sub>3</sub> microplate of small side length ( $W \sim 3.7 \mu\text{m}$ ) was excited through 3-photon excitation at  $\lambda_0 = 1280 \text{ nm}$  and  $T = 83 \text{ K}$ , with the excitation spot illuminating the surface's center of the microplate. The corresponding wavelength spectra and light-light curve are respectively shown in Figure 4.6a and Figure 4.6b, which shows that the microplate supported stable single-mode lasing at 424 nm with  $P_{\text{th}} \sim 215 \text{ mJ cm}^{-2}$  and quality factor  $Q \sim 1400$ . To further investigate the lasing characteristics of this particular microplate, computer simulation was done with COMSOL Multiphysics 5.0. In the simulation, a square of side length  $3.7 \mu\text{m}$  was used to represent the CsPbCl<sub>3</sub> microplate, which is surrounded by air, with scattering boundary conditions applied to the edges of the whole system. 2-D finite-element method was used to calculate the electric field intensity ( $|E|$ ) distribution of the supported WGMs of the system at a frequency of  $7.0781 \times 10^{14} \text{ Hz}$  (corresponding to  $\lambda \sim 424 \text{ nm}$ ) and an initial value of  $n_{\text{eff}} = 6.77$ , in which the problem was solved at  $n_{\text{eff}} = 6.48$ . The corresponding  $|E|$  pattern of the solved WGM is shown in Figure 4.7a, which is formed by the resonance of plane waves internally reflected at the middle of the four edges of the microplate at an incident angle of  $45^\circ$ . Resonance is attained when the roundtrip length ( $L$ ) is a multiple of the effective wavelength ( $\lambda / n_{\text{eff}}$ ), in which the plane waves constructively interfere with each other after each roundtrip. In addition, Figure 4.7a indicates that  $|E|$  is maximized at the middle of each of the four sides of the microplate. This is due to the multiple local maxima formed as a result of the

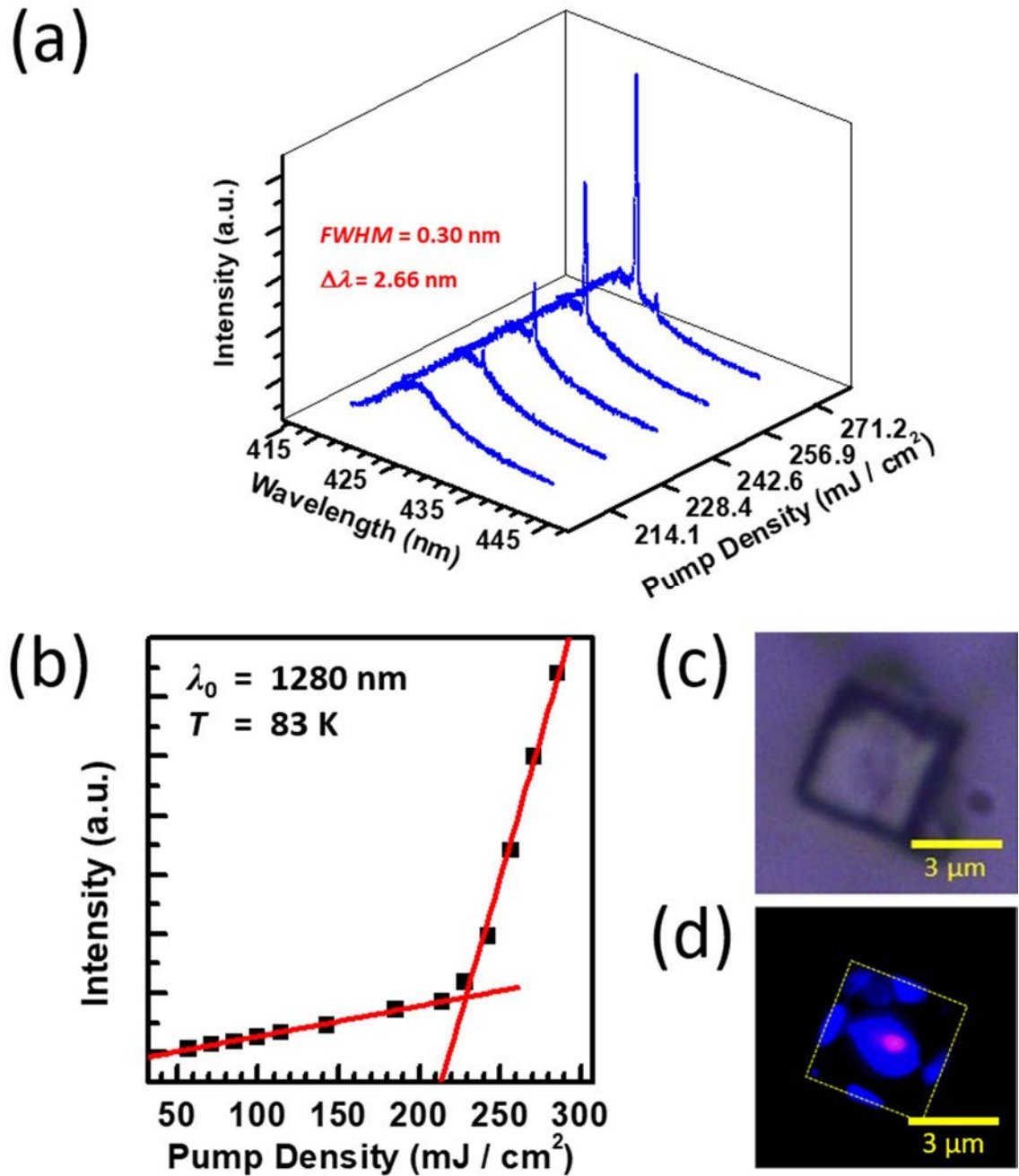
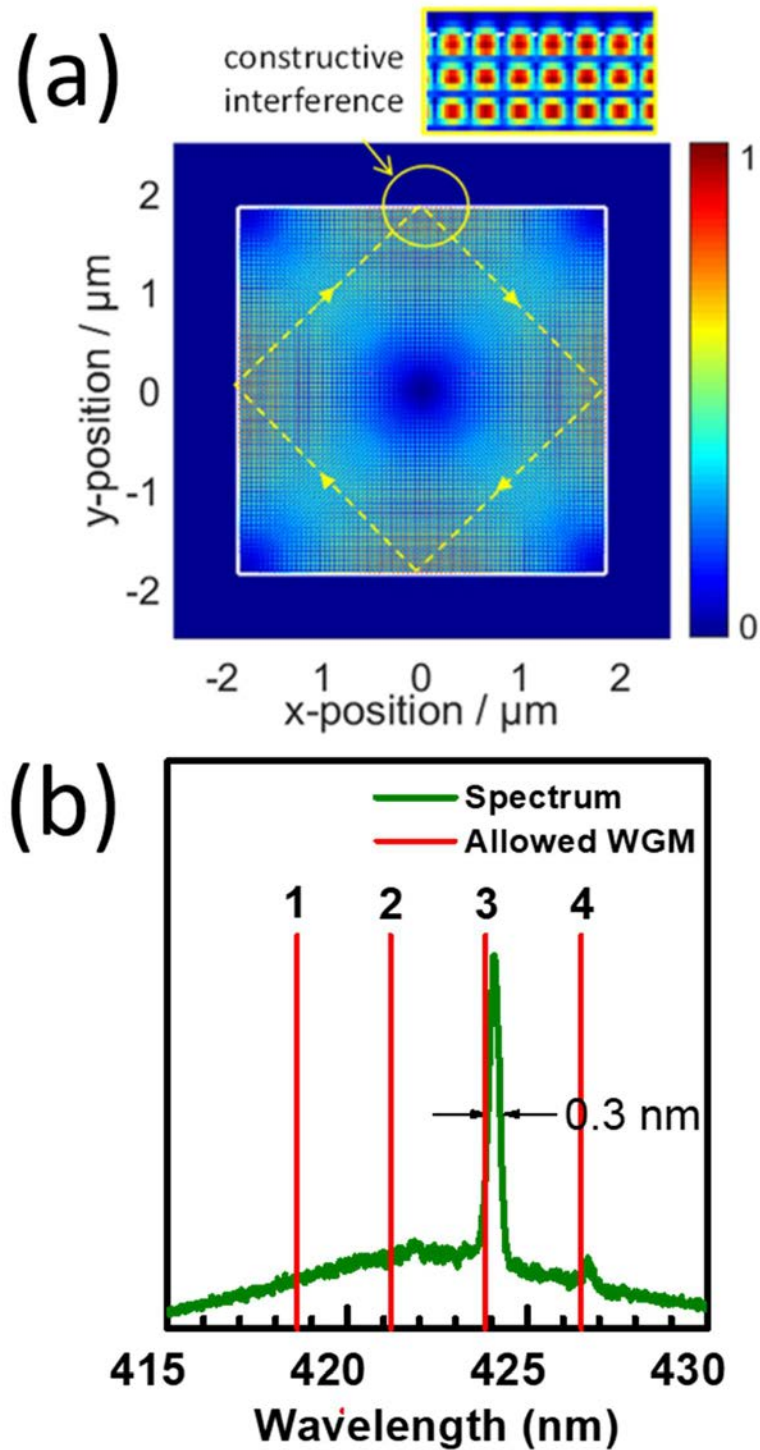


Figure 4.6 (a) Emission spectra and (b) light-light curve of a CsPbCl<sub>3</sub> microplate ( $W = 3.7$  μm) under 1280-nm excitation at 83 K. The optical microscope images of the same single microplate before and during excitation are shown in (c) and (d), respectively.



**Figure 4.7** (a) Theoretically calculated electric field strength  $|E|$  distribution of the lasing mode supported by the CsPbCl<sub>3</sub> microplate of side length  $W = 3.7 \mu\text{m}$  over the microplate's surface, and (b) the explanation of the support of single-WGM operation from the microplate.



constructive interference between the incident and reflected waves during the internal reflections inside the microplate (see the inset of Figure 4.7a). This simulation result agrees with the microscope image shown in Figure 4.6d, in which the middle of the four edges of the microplates were maximized during WGM laser emission. In the microscope image, the bright spot at the center of the microplate was the emission spot arisen from the pumping beam, which was not caused by the WGM. To further confirm that Figure 4.7a corresponds to the WGM shown in the emission spectrum (Figure 4.6a), the theoretically allowed fundamental WGMs of the 3.7- $\mu\text{m}$  microplate were calculated based on Equation (4.1) with  $n_{\text{eff}} = 6.48$ . The result was overlapped with the experimentally measured lasing spectrum as shown in Figure 4.7b. It is found that the wavelength of the simulated ‘Mode 3’ and ‘Mode 4’ matched with the lasing spectrum. The small amount of error in the peak positions could be attributed to the measurement errors in parameters such as  $W$  of the microplate. Therefore, it can be confirmed that the lasing mode excited in this microplate, as well as the simulation results in Figure 4.7a, correspond to ‘Mode 3’. In the lasing emission, ‘Mode 3’ was dominant because it was the only WGM with a wavelength close enough to the peak gain wavelength of the material ( $\sim 424$  nm), so as to receive sufficient optical gain that exceeded the lasing threshold during excitation. In this way, only ‘Mode 3’ was supported while other WGMs were suppressed, resulting in single-WGM.

## 4.5. Conclusion

To conclude, the nonlinear absorption and emission characteristics of single-crystalline CsPbCl<sub>3</sub> perovskite microplates were studied. From the microplate clusters, the room-temperature 2PA and 3PA coefficients were found to be  $8.0 \times 10^{-3} \text{ cm GW}^{-1}$  and  $2.1 \times 10^{-5} \text{ cm}^3 \text{ GW}^{-2}$  respectively, which were high enough to find optical device



applications. In addition, PL and ASE were also obtained from the microplate clusters under 2- and 3-photon excitation at 83 K. No lasing emission was obtained from the clusters because coherent optical feedback was not supported. Instead, lasing emission was realized from single CsPbCl<sub>3</sub> microplates with square shapes and smooth facets. Under 2- and 3-photon excitation at 83K, these single microplates supported both multi- and single-WGM lasing, depending on the size of the microplate. A sufficiently small microplate with side length  $W \sim 3.7 \mu\text{m}$ , was found to support stable single-WGM lasing with a high quality factor of  $\sim 1400$ . The investigation has demonstrated that micro-scale single-crystalline CsPbCl<sub>3</sub> perovskite is a superior nonlinear optical gain material for high-performance upconversion lasing devices.



## 5. Influence of Plasmonic Effect on WGM lasing of NaYF<sub>4</sub> Hexagonal Microrods

Other than halide perovskites, optical devices based on NaYF<sub>4</sub> is also very popular among researchers in the recent decade. In an attempt to enhance the lasing characteristics of the lasers made of this material, the plasmonic effect was introduced into the whispering-gallery modes in Yb<sup>3+</sup>–Er<sup>3+</sup>–Tm<sup>3+</sup> tri-doped  $\beta$ -NaYF<sub>4</sub> hexagonal microrod in this work. This was achieved by the addition of a metallic layer in the laser design. In this chapter, the major results of the investigation, especially the influence of the plasmonic effect on the WGM lasing characteristics of the hexagonal rod, would be discussed.

### 5.1. Background

For most gain materials, the optimal wavelengths of emission are only limited to a narrow range. To realize lasers with wide emission bandwidth from ultraviolet to infrared wavelength, foreign ions can be doped into an upconversion material to modify its emission characteristics. The type and concentration of the dopant can be controlled to realize broadband-tunable lasers. One of the most popular examples among researchers in recent years is the lanthanide ion (Ln<sup>3+</sup>) doped upconversion materials. However, the lasing thresholds attained by this kind of gain materials are relatively low [63] due to their low upconversion emission efficiencies [64, 65]. If one could further



reduce the lasing threshold of these wide bandwidth lasers, this would open up a wide range of applications, including all-optical on-chip information processing, biomedical imaging and optogenetics [66-69].

In an attempt to find such a solution, extensive investigations have been taken in the enhancement of upconversion emission from Ln<sup>3+</sup>-doped nanoparticles (NPs), which is found to be achieved by surface plasmon resonance (SPR) [70]. The enhancement can be attributed to the effective coupling between the excited fluorophores of the upconversion NPs and the SPR of the metallic NPs. When the SPR of the metal NPs matches with the emission wavelengths of the upconversion NPs, the spontaneous upconversion emission intensity, as reported from researchers, would be enhanced by at least 2 times, and up to >30 times [71-75]. In fact, lasing emission by plasmonic mode is also demonstrated by embedding a metal stripe in Er<sup>3+</sup>-doped phosphate glass [76]. However, from all of the above results, it is not proven directly that there is an association between the use of SPR and a reduced lasing threshold in the Ln<sup>3+</sup>-doped upconversion lasers [77, 78].

To find out the effect of SPR on the lasing threshold of Ln<sup>3+</sup>-doped upconversion lasers, an experiment is designed to study the blue, green and red lasing characteristics of Yb<sup>3+</sup>-Er<sup>3+</sup>-Tm<sup>3+</sup> tri-doped  $\beta$ -NaYF<sub>4</sub> hexagonal microrod with and without the use of SPR [11]. SPR is introduced into the optical modes of the laser by depositing the microrod onto a thin Ag-layer [79]. Hexagonal rods were chosen in this study in order to sustain lasing emission through whispering-gallery modes through its hexagonal cross-section, and the rods were chosen to be micro-sized to minimize optical loss from metallic absorption in the Ag layer.

In this experiment, it is noted that any interaction between the WGMs of the microrod and the surface plasmons aroused from the plasmonic effect was demonstrated





outside the laser cavity through the coupling at the Ag-layer. Therefore, it could be confirmed that any changes in lasing characteristics of the microrod upon the insertion of the Ag-layer, was attributed to the plasmonic effect.

## 5.2. Synthesis and Characterization of Yb<sup>3+</sup>–Er<sup>3+</sup>–Tm<sup>3+</sup> tri-doped $\beta$ -NaYF<sub>4</sub> Hexagonal Microrods

Hydrothermal method was used to prepare the NaYF<sub>4</sub>:Ln<sup>3+</sup> (Ln<sup>3+</sup> = Yb<sup>3+</sup>/Er<sup>3+</sup>/Tm<sup>3+</sup>) microrods. The reagents included rare-earth (Ln = Yb, Er, Tm) oxides (99.99%), ethylenediamine tetraacetic acid (EDTA, > 99.5%), sodium hydroxide (NaOH, > 96.0%), ammonium fluoride (NH<sub>4</sub>F, > 96.0%) and hydrochloric acid (HCl, 12M, diluted to 1M by deionized water). All of the chemicals were used directly without further purification, as they were purchased in analytical grade. To synthesize the Yb<sup>3+</sup>–Er<sup>3+</sup> doped  $\beta$ -NaYF<sub>4</sub> microrods, Y<sub>2</sub>O<sub>3</sub>, Yb<sub>2</sub>O<sub>3</sub> and Er<sub>2</sub>O<sub>3</sub> powder were dissolved in dilute nitrate solution. Any residual nitrate was removed by evaporation through heating. This results in a clear solution of Ln(NO<sub>3</sub>)<sub>3</sub> (Ln=Y, Yb, Er). After that, 0.4g of EDTA was dissolved in deionized water to obtain 12.5 ml of an aqueous solution, which was then mixed with NaOH aqueous solution (5.0 M) by stirring until the mixture was clear. Then, 5 ml of the Ln(NO<sub>3</sub>)<sub>3</sub> (Ln = Y, Yb, Er) aqueous solution (0.2 M), 8 mL of NH<sub>4</sub>F aqueous solution (2.0 M) and 7 ml of the diluted hydrochloric acid (1 M) were added into the mixture, and the resulting solution was stirred for 90 minutes with a magnetic stirrer. After stirring, the solution was transferred to a 50 mL autoclave maintained at 200 °C for 40 hours. When completed, the autoclave was cooled down to room temperature, followed by centrifugation of the solution to separate

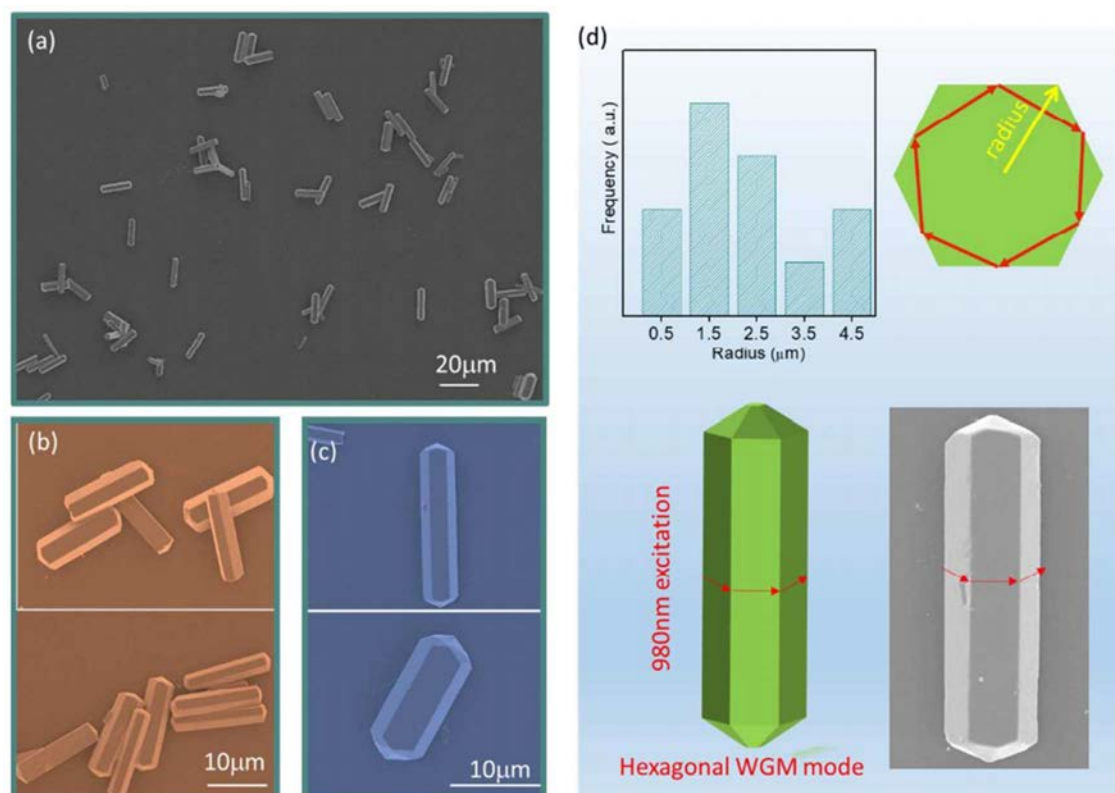


**Figure 5.1** (a) – (c) SEM images of the NaYF<sub>4</sub> microrods. (d) The size distribution of NaYF<sub>4</sub> microrods in (a), and the schematic diagram of a single NaYF<sub>4</sub> microrod. It is noted that the radius of the microrods varies from 0.5 to 4.5 μm. The microrods, in general, have six flat surfaces and two sharp ends. Under optical excitation, whispering-gallery modes (i.e. red arrows) are established on the hexagonal flat surfaces to support coherent optical feedback (i.e. lasing emission).

the precipitates. The precipitates were washed with deionized water and ethanol for three times, followed by drying in air at 80 °C for 8 hours. Similar process can be used to synthesize Yb<sup>3+</sup>–Tm<sup>3+</sup> doped and Yb<sup>3+</sup>–Er<sup>3+</sup>–Tm<sup>3+</sup> doped β-NaYF<sub>4</sub> microrods using different rare-earth oxides when preparing the Ln(NO<sub>3</sub>)<sub>3</sub> solution.

Figure 5.1a to Figure 5.1c show the scanning electron microscope (SEM) images, which shows that each of the synthesized microrods had six flat surfaces to support whispering-gallery modes (WGMs) (Figure 5.1d) with two pointed ends. The microrods had radii ranging from 0.5 to 4.5 μm, and the size distribution of the microrods corresponding to Figure 5.1a is presented in the histogram in Figure 5.1d. To confirm

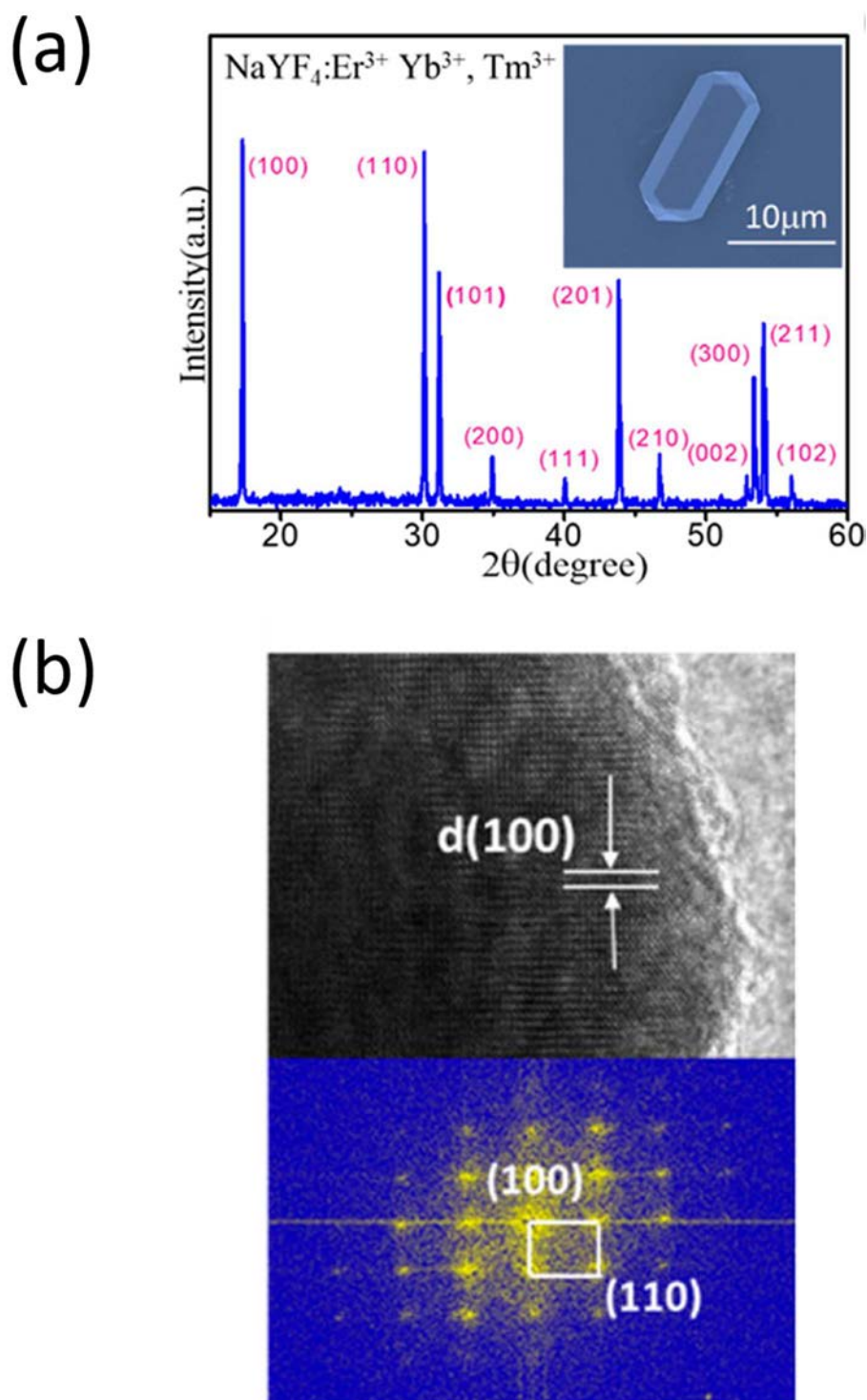


**Figure 5.2** (a) XRD pattern of the as-synthesized Yb<sup>3+</sup>–Er<sup>3+</sup>–Tm<sup>3+</sup> tri-doped  $\beta$ -NaYF<sub>4</sub> hexagonal microrods. The inset shows the corresponding SEM image. (b) HR-TEM and FFT image of the  $\beta$ -NaYF<sub>4</sub> hexagonal microrod.



the high purity and crystallinity of the microrods, X-ray diffraction (XRD) pattern of the microrods was measured (Figure 5.2a), in which the result matched with that of  $\beta$ -NaYF<sub>4</sub> crystal (JCPDS file number 16-0334) [80]. In addition, high-resolution tunneling electron microscope (HR-TEM) image of a microrod, which can be found in Figure 5.2b. The lattice structure of the  $\beta$ -NaYF<sub>4</sub> crystal can be indexed at the (100) plane, with a space group of  $P6_3/m$ . The corresponding fast Fourier transform (FFT) image is also shown in the same figure, which revealed the high crystallinity of the microrods.

### 5.3. Optical Measurement and Computer Simulation Method

To measure the emission spectrum from the optically pumped sample, a set-up similar to the one mentioned in the previous chapter was used, which is shown in Figure 5.3. In the configuration, the excitation beam was directed to a 50 $\times$  objective lens with the help of a dichroic mirror placed inside an optical microscope (Leica DM1000 LED). The excitation beam was either 980-nm continuous wave (CW) laser for photoluminescence (PL) excitation, or 980-nm pump pulses (0.8 cm in spot diameter) generated using a frequency-tripled 355 nm Q-switched Nd:YAG pulsed laser (6 ns, 10 Hz) and an optical parametric oscillator for lasing emission excitation. The objective lens focused the excitation beam onto the sample from the top, and the emission was collected by an optical fiber fed into a spectral analyzer. A charge-coupled device (CCD) camera was also installed on top of the microscope in order to observe the sample with and without excitation. The specific polarization of the pumping beam was selected with the help of a polarizer and a half-wave plate. All of the excitations and

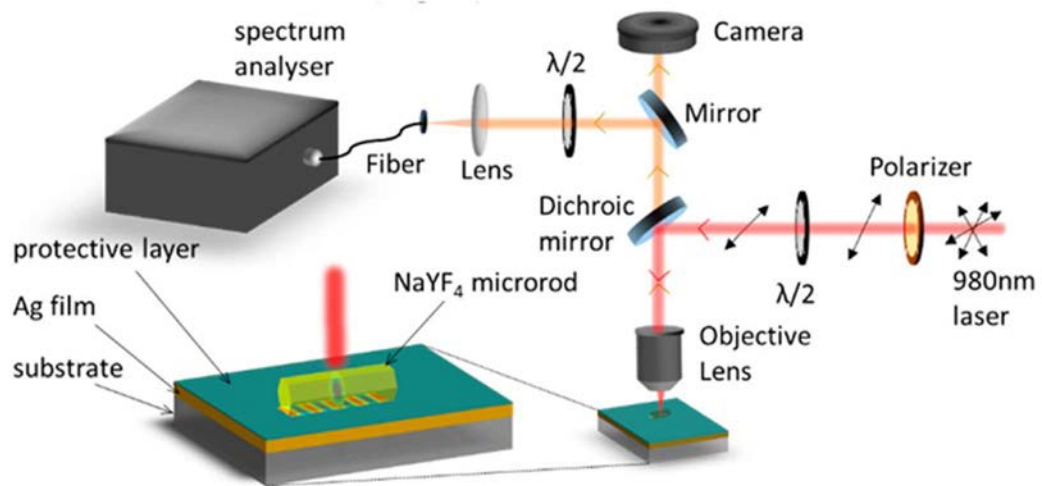


**Figure 5.3** Experimental setup for the PL and lasing spectra measurement of a NaYF<sub>4</sub> microrod

measurements were done under room conditions.

In this work, computer simulation was also involved to determine the field distribution and Q-factor ( $Q$ ) of the WGMs supported by the laser cavity using two-dimensional finite-element method (COMSOL Multiphysics 5.0). A regular hexagon was used to represent the cross-section of the NaYF<sub>4</sub> hexagonal rod. For plasmonic cavities formed by depositing the microrod onto an Ag-coated substrate, rectangles of length ( $x$ -dimension) 10  $\mu\text{m}$  were used to represent the MgF<sub>2</sub>, Ag, and substrate (SiO<sub>2</sub>) layers. The rectangles' widths ( $y$ -dimension) were equal to the thicknesses of each of the three layers. All systems were assumed to be surrounded by air with scattering boundary conditions. The eigenfrequency solver of the software was used to calculate the WGMs. Each WGM was associated to a complex eigenfrequency  $f (= f_r + jf_i)$ . The corresponding mode quality factor can be calculated by  $Q = f_r / (2f_i)$ . In all of the calculations in this work, the refractive index of NaYF<sub>4</sub> ( $= 1.623$ ) was assumed to be wavelength-independent, whereas those of MgF<sub>2</sub>, Ag, and SiO<sub>2</sub> are, respectively, 1.3815,



0.04– $j$ 2.6484, and 1.4656 at 450 nm; 1.3787, 0.056895– $j$ 3.5047, and 1.4603 at 540 nm; and 1.3767, 0.051288– $j$ 4.4404, and 1.4564 at 654 nm [15, 81, 82].

## 5.4. WGM Plasmonic Laser Design with $\beta$ -NaYF<sub>4</sub> Hexagonal Microrods

To introduce plasmonic effect into the WGM of the  $\beta$ -NaYF<sub>4</sub> hexagonal microrods, a microrod of radius  $r = 2 \mu\text{m}$  was deposited onto an Ag-coated SiO<sub>2</sub> substrate to form a plasmonic slot waveguide structure. The thickness of the Ag coating was chosen as 50 nm, which is expected to be sufficient to form surface plasmon without coupling into the Ag-substrate interface. Here, we assumed a MgF<sub>2</sub> layer of thickness  $h$  was inserted between the Ag coating and the microrod as the protection layer, which is a technique mentioned in Section 2.3 for the suppression of metallic absorption loss in the Fabry-Pérot modes of nano-lasers, see the inset of Figure 5.4a for the structure of the design. To see if the protection layer is necessary for the WGM of this micro-laser, the effect of  $h$  on the modal cavity loss was studied by plotting the calculated mode Q-factor ( $Q$ ) from computer simulation against  $h$ , at the three peak emission wavelengths of the NaYF<sub>4</sub>:Yb<sup>3+</sup>, Er<sup>3+</sup>, Tm<sup>3+</sup> hexagonal microrod ( $\lambda = 450, 540$  and 654 nm), as shown in Figure 5.4a. The results showed that an increase in  $h$  does not contribute to the enhancement of  $Q$  for all of the three emission wavelengths, which suggested that the protection layer is unnecessary in terms of the minimization of cavity loss. Unlike a nanostructure, a microrod is large enough such that profile of the plasmonic modes can be extended to the microrod without much metallic absorption by the Ag layer. Adding a protection layer in this case would only cause the light to escape from the microrod through surface plasmon propagation along the MgF<sub>2</sub>-Ag interface,



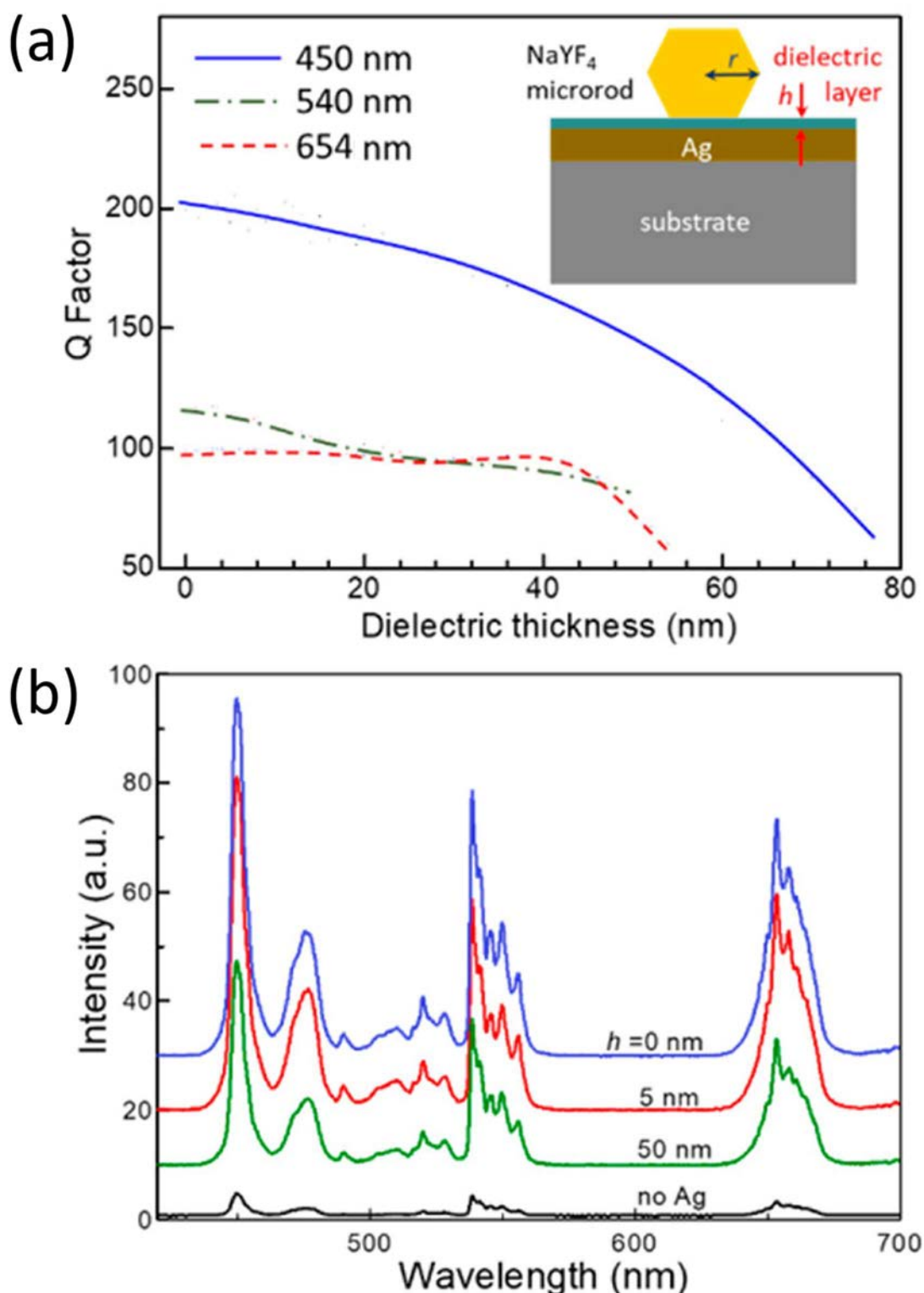


**Figure 5.4** (a) Plot of calculated Q-factor of a NaYF<sub>4</sub>:Yb<sup>3+</sup>, Er<sup>3+</sup>, Tm<sup>3+</sup> hexagonal microrod ( $r = 2 \mu\text{m}$ ) deposited on an Ag-coated (50 nm) substrate, which is also protected by a MgF<sub>2</sub> dielectric layer with different thickness. (b) Measured spontaneous emission spectra from a microrod ( $r = 2 \mu\text{m}$ ) deposited on an Ag-coated substrate with a different thickness of MgF<sub>2</sub> protection layer, as well as that from a bare microrod without Ag and MgF<sub>2</sub>.



resulting in a drop in  $Q$ .

The simulation result was verified by experimental work. Figure 5.4b shows the emission spectra of the photoluminescence (PL) of a NaYF<sub>4</sub>:Yb<sup>3+</sup>, Er<sup>3+</sup>, Tm<sup>3+</sup> hexagonal microrod ( $r = 2 \mu\text{m}$ ) with and without a 50-nm Ag coating for different values of  $h$  under unpolarized 980-nm excitation. Referring to the figure, by inserting the 50-nm Ag coating without the protection layer (i.e.  $h = 0$ ), the peak intensities of blue (450 nm), green (540 nm) and red (654 nm) PL of the bare microrod were enhanced by  $\sim 16$ ,  $\sim 13$  and  $\sim 13$  times respectively. This confirmed the insertion of the Ag coating contributed to a significant amount of emission enhancement. However, as shown in the emission spectra, adding a thin protection layer ( $h = 5 \text{ nm}$ ) in addition to the Ag layer did not lead to noticeable changes in the peak PL intensities for the three emission colours. When a thicker protection layer ( $h = 50 \text{ nm}$ ) is inserted instead, the PL intensities actually dropped compared to the case of  $h = 0 \text{ nm}$  or  $h = 5 \text{ nm}$ , which indicated that the protection layer actually weakened the emission enhancement. Thus, it can be seen that the experimental findings matched with the simulation results, so it can be concluded that the protection layer is not required in our design for suppressing the metallic absorption loss. However, a thin protection layer in the laser protects the Ag layer from oxidation in practice, hence  $h = 5 \text{ nm}$  was chosen in the following experiment.

## 5.5. Effect of Excitation Polarization on the Emission Intensity of the Plasmonic Laser Design

To further optimize the emission intensity, the effect of excitation polarization on the emission intensity of the microrod laser was also studied. Here, we polarized the





excitation beam generated from the 980-nm CW laser using a polarizer and a half-wave plate, with orthogonal polarizations parallel ( $\theta_{\text{in}} = 0^\circ$ ) and perpendicular ( $\theta_{\text{in}} = 90^\circ$ ) to the length of the microrod. The measured PL spectra from the cavity (with the Ag-coated substrate) at these two excitation polarization angles were shown in Figure 5.5a, which showed that the PL intensity excited at  $\theta_{\text{in}} = 90^\circ$  was 30% higher than that at  $\theta_{\text{in}} = 0^\circ$ . The photos of the microrod under the two excitation schemes were also presented in Figure 5.5b, which clearly showed that the scattered light from the microrod appeared to be brighter for  $\theta_{\text{in}} = 90^\circ$ . Moreover, when we plotted the emission spectra from  $\theta_{\text{in}} = 0^\circ$  to  $\theta_{\text{in}} = 360^\circ$  (Figure 5.5c), it was found that the emission intensity was maximized and minimized at  $\theta_{\text{in}} = 90^\circ$  and  $\theta_{\text{in}} = 0^\circ$ , respectively. It is noted that similar enhancement effect due to the excitation polarization was also observed in microrods using other dopants, see their emission spectra at  $\theta_{\text{in}} = 0^\circ$  and  $\theta_{\text{in}} = 90^\circ$  in Figure 5.6. This phenomenon was possibly due to the dependence of the propagating direction of the excited surface plasmon on the pump polarization, because surface plasmon can only propagate under transverse magnetic (TM modes). The propagating direction would impact how the surface plasmon interacted with the WGM of the microrod structure. As a result,  $\theta_{\text{in}} = 90^\circ$  would be selected in the following study regarding the influence of plasmonic effect on the emission of the microrod.

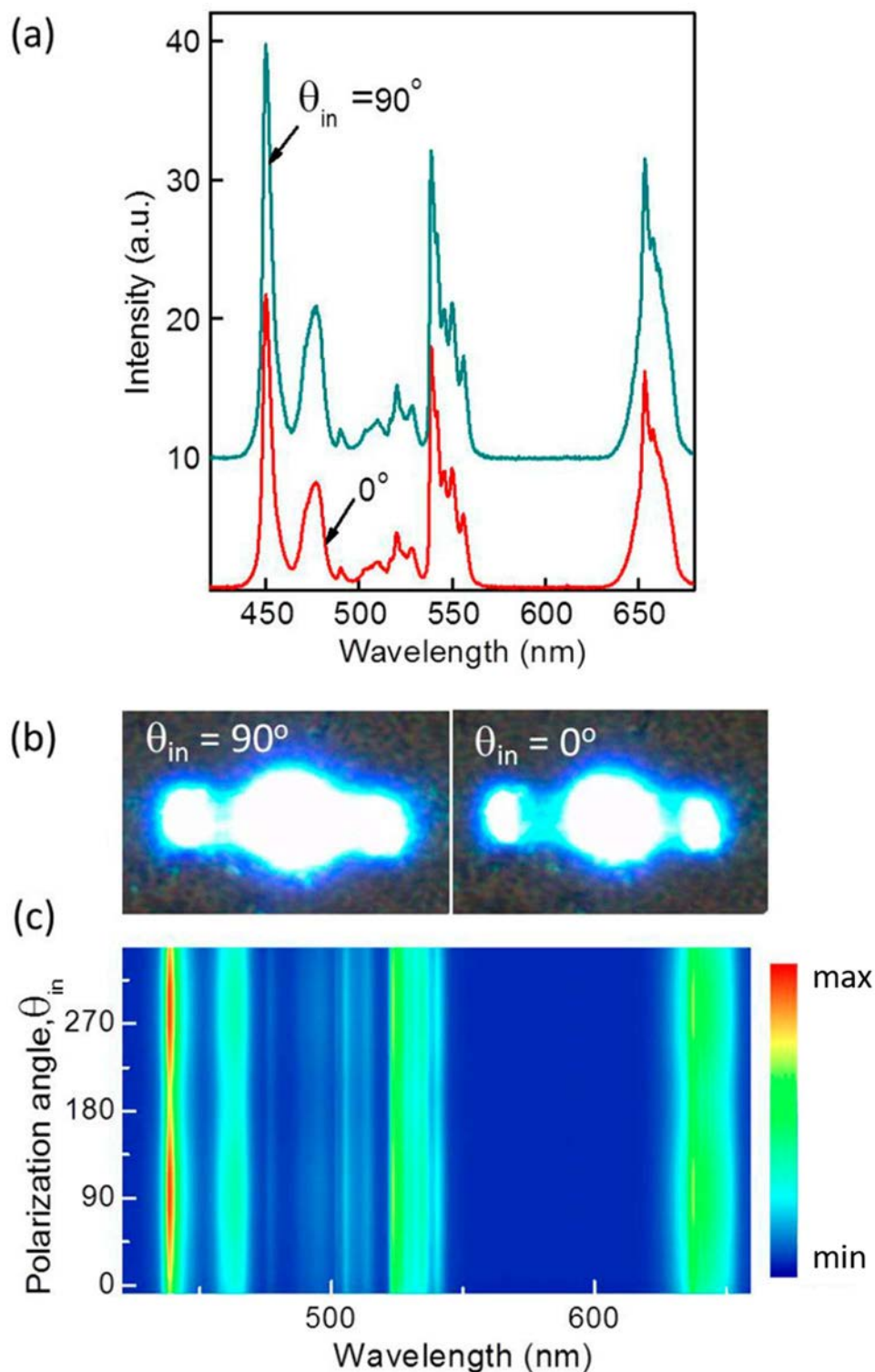


**Figure 5.5** (a) Emission spectra of a NaYF<sub>4</sub>:Yb<sup>3+</sup>, Er<sup>3+</sup>, Tm<sup>3+</sup> hexagonal microrod deposited on an Ag-coated substrate under 980-nm laser excitation with two orthogonal orientations  $\theta_{in} = 90^\circ$  (perpendicular to the length of the microrod) and  $\theta_{in} = 0^\circ$  (parallel to the length of the microrod); (b) the corresponding microscope images of the microrod at these two polarizations. (c) Two-dimensional plot of emission intensity versus  $\theta_{in}$  and emission wavelength.

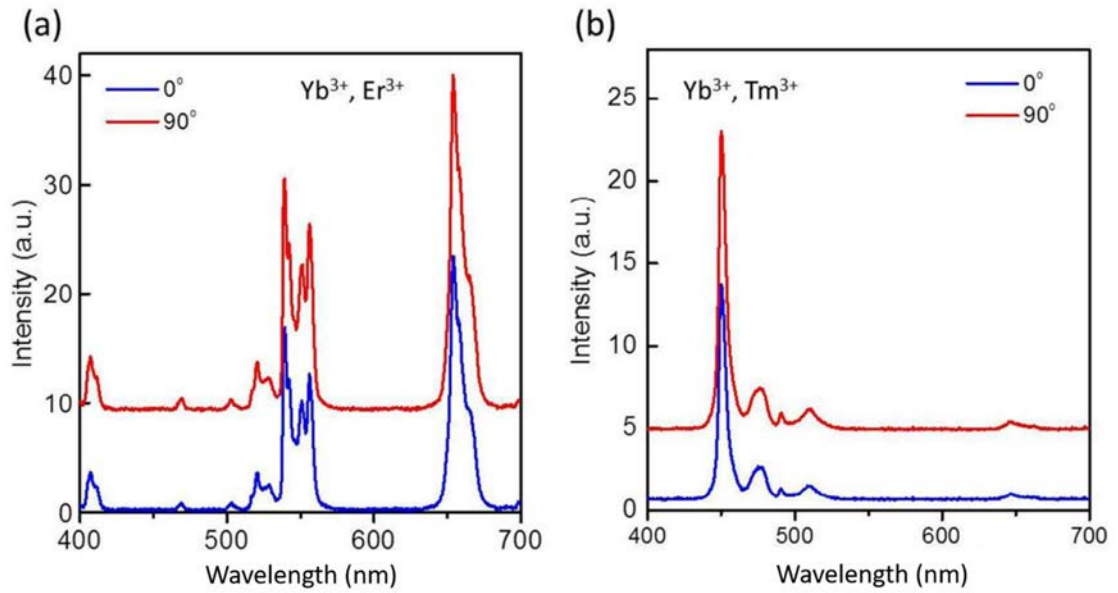


**Figure 5.6** PL characteristics of (a) NaYF<sub>4</sub>:Yb<sup>3+</sup>, Er<sup>3+</sup> and (b) NaYF<sub>4</sub>:Yb<sup>3+</sup>, Tm<sup>3+</sup> hexagonal microrods ( $r = 2 \mu\text{m}$ ) under excitation at polarizations (i.e.  $\theta_{\text{in}} = 0^\circ$  and  $90^\circ$ ). At  $\theta_{\text{in}} = 90^\circ$ , the emission intensity is enhanced by 30% compared to that using  $\theta_{\text{in}} = 0^\circ$ .

## 5.6. Influence of Plasmonic Effect on the Emission Characteristics of the Plasmonic Microrod WGM Laser.

In Figure 5.5b, it was also found that the emission was scattered from both ends of the microrod along its length, which revealed that light also propagated along the length of the microrod due to the SPR modes supported at the surface of the Ag layer, in addition to that in the perpendicular directions of the microrod's WGM. To confirm the scattered light was due to surface plasmon formation, excitation of the microrod was done by 980-nm CW laser at  $\theta_{\text{in}} = 90^\circ$  with and without the Ag-coated substrate, and the photos during excitation are shown in Figure 5.7. The photos indicated that the scattered light at the edges was exclusive to the microrod with the Ag layer excited either at the center position, or at one of the edges. As a result, it can be concluded that

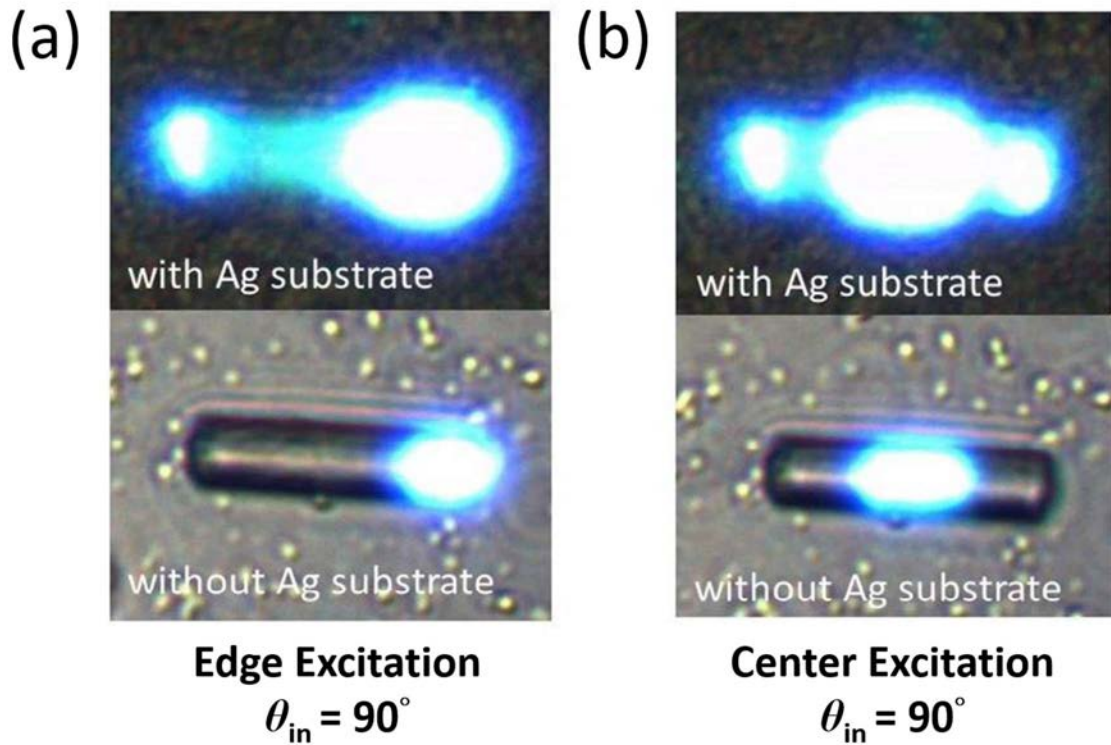


**Figure 5.7** Photos of a NaYF<sub>4</sub>:Yb<sup>3+</sup>, Er<sup>3+</sup>, Tm<sup>3+</sup> hexagonal microrod ( $r = 2 \mu\text{m}$ ) deposited on the Ag-coated substrate under (a) edge and (b) center excitation. The corresponding photos for the microrods deposited on a substrate without Ag coating are also shown for comparison.

the scattered light corresponded to the surface plasmon propagating along the microrod's length, which was only supported in the presence of the Ag layer. In addition, the contrast in the emission brightness observed from the photos also agreed with the PL enhancement measured in Figure 5.4b.

To study the effect of the introduced plasmonic effect on the microrod's lasing threshold, we excited the microrod using 980-nm pump pulses ( $\theta_{in} = 90^\circ$ ) of pump density  $\sim 3.5 \text{ mJ} / \text{cm}^2$ , with and without the Ag coating. Figure 5.8b plots the emission spectra around the three peak gain regions (i.e.,  $\sim 450$ ,  $\sim 540$  and  $\sim 654 \text{ nm}$ ) of the microrod ( $r = 2 \mu\text{m}$ ) during excitation, which shows that sharp peaks of linewidths less than  $0.4 \text{ nm}$  were obtained for all of the colours with and without the Ag layer,

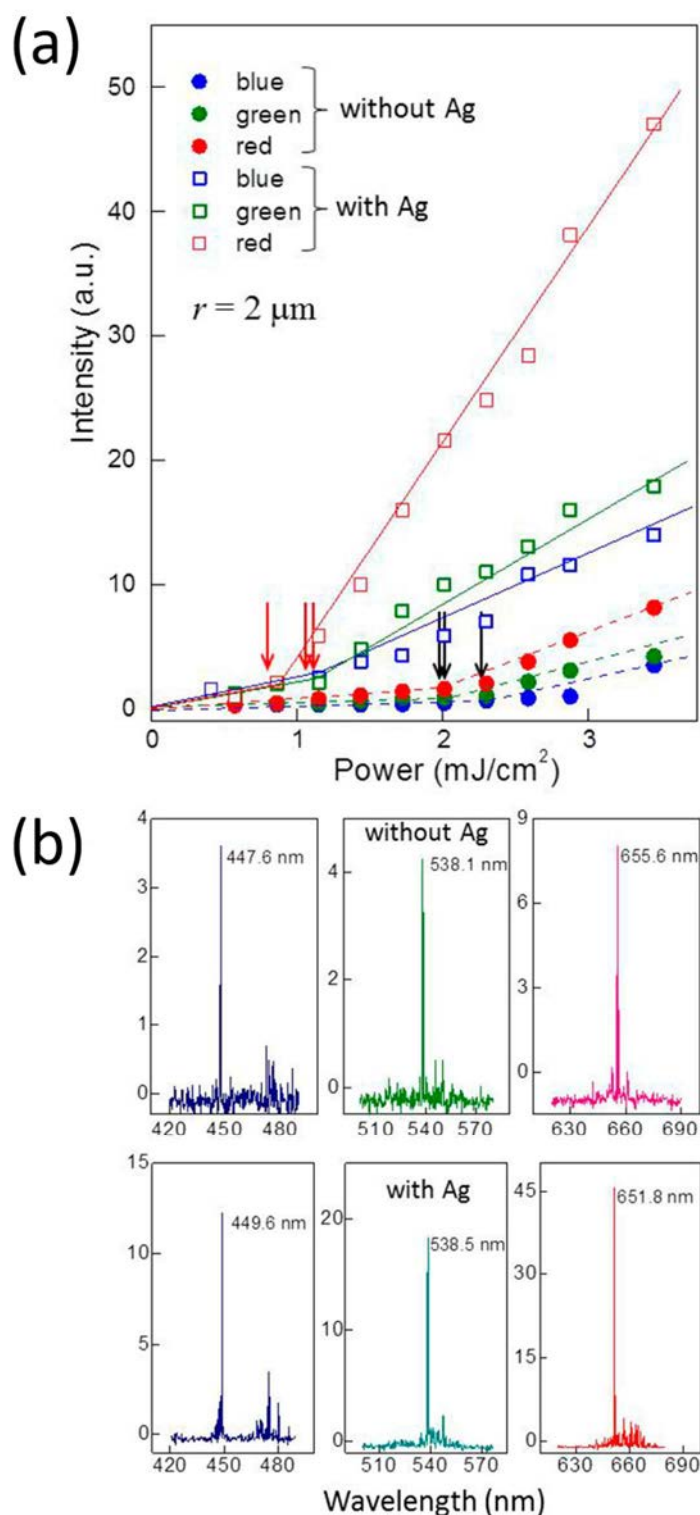


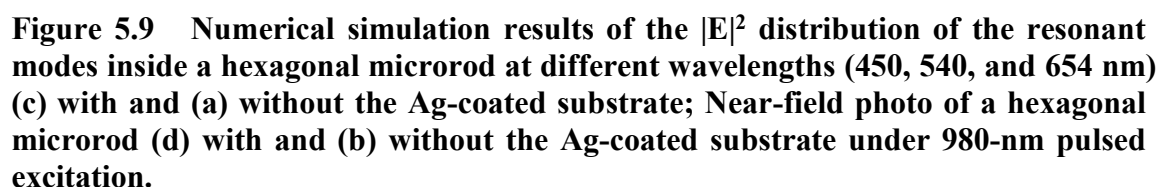
**Figure 5.8** (a) Light–light curves of the hexagonal microrods with and without deposition on a 50-nm Ag coat for the emission peaks of the three colors (i.e., ~450, ~540 and ~654 nm). (b) Corresponding emission spectra of the hexagonal microrods with and without deposition on the Ag-coated substrate at a pumped density of 3.5 mJ / cm<sup>2</sup>.



corresponding to lasing emissions. It is noted that the measured linewidths for both structures were similar, but the signal-to-noise ratio of the lasing peaks in the case with the Ag coating was significantly higher than the one without it. This finding may suggest that the use of Ag coating enhanced the emission intensity of the microrod through surface plasmon coupling without noticeable impact on the quality factor of the WGM itself caused by metallic absorption. When the corresponding light-light curves were plotted (Figure 5.8a), it was revealed that the lasing thresholds (denoted by the arrows on the figure) of the blue, green and red lasing emissions were respectively reduced from 2.0, 2.0, and 2.3 to 0.89, 1.16, and 1.16 mJ / cm<sup>2</sup>, which translates into a reduction of ~50%, through the introduction of plasmonic effect.

WGM lasing in the bare hexagonal microrods without the deposition onto a metallic layer was demonstrated by previous investigations [83]. This agreed with Figure 5.8b that lasing was supported even without the use of plasmonic effect. In order to confirm the lasing peaks obtained from the emission spectra originated from WGMs, we have calculated the squared intensity distribution of the modal electric field ( $|E|^2$ ) in the a bare microrod ( $r = 2 \mu\text{m}$ ) without an Ag coat by computer simulation (finite-element method), the results were plotted in Figure 5.9a. It can be seen from the simulation results that WGMs were established by internal reflections at the 6 flat surfaces of the microrod, with  $|E|^2$  maximized at the center of each surface due to the constructive interference between the incident and reflected wave at each reflection. This pattern agreed with the near-field image shown in Figure 5.9b, that, a single intense spot can be observed in the middle of the microrod's flat surface when there was no Ag-coating. For the case with the Ag-coated substrate, simulation results indicated that the modal  $|E|^2$  distribution of the bare microrod's WGM was modified by the Ag





## 5.7. Conclusion

The influence of plasmonic effect on the WGM lasing characteristics of the  $\text{Yb}^{3+}\text{-Er}^{3+}\text{-Tm}^{3+}$  tri-doped  $\beta\text{-NaYF}_4$  upconversion hexagonal microrods was studied. This was achieved by deposition of the microrod onto an Ag-coated substrate. An enhancement of more than 10 times in upconversion spontaneous emission intensity is measured with the introduction of SPR. For WGM lasing emission, the introduction of



plasmonic effect reduces the lasing threshold by 50%, which is due to the formation of low-loss modified WGM from the coupling between the WGM of the microrod and the SPR modes supported on the surface of the Ag layer.





# Final Conclusion

In this thesis, the plasmonic upconversion lasers are discussed from both the theoretical and experimental points of view, including performance analysis, optical excitation, and measurement techniques, as well as the fabrication of the devices.

Optical mode analysis utilizing Maxwell equations was done to study the performance, including the quality factor, threshold gain and optical confinement factor, of rectangular and cylindrical laser structures. The optical modes of a laser structure were either solved by dispersion relations (for simpler structures) or 2-dimension matrix method (for more complex structures). It is demonstrated that the mathematical models can be used to optimize the waveguiding performance by deducing the performance trends over a range of dimensions of the layers. In general, the theoretical analysis provided insights on laser designs.

Methods of experiment analysis on lasers, including spectral analysis and z-scan measurement, are also discussed. The techniques are applied to fabricated laser structures being studied. First, square-shaped  $\text{CsPbCl}_3$  microplates are synthesized as an example of upconversion lasing cavities supporting high-quality single-mode and multi-mode WGM lasing at cryogenic temperature. Second,  $\text{Yb}^{3+}\text{-Er}^{3+}\text{-Tm}^{3+}$  tri-doped  $\beta\text{-NaYF}_4$  hexagonal microrods were used to study the influence of plasmonic effect on hexagonal whispering-gallery modes. The plasmonic effect was introduced by deposition of the microrod onto an Ag-coated substrate. It is found that more than 10-fold enhancement in PL emission intensity, as well as 50% reduction in lasing threshold can be obtained due to the interaction between surface plasmon modes and the original



whispering-gallery modes. In both experiments, finite element method was applied to deduce the modal characteristics of the lasers with different structures.

Through the findings in this work, the plasmonic effect is shown to be an important aspect in laser designs, due to its capability of subwavelength optical confinement and enhancement of spontaneous and stimulated emission. Moreover, upconversion lasing with superior lasing characteristics are demonstrated in plasmonic lasers, which may open up a wide range of new optical device applications.



# Reference

- [1] M. J. Adams, *An Introduction to optical waveguides*. pp. xv, 401 pages.
- [2] *Introduction to Optical Waveguide Analysis*. S.I.: John Wiley & Sons, Inc. / Engineering, 2001.
- [3] N. Ishihara *et al.*, "Subwavelength metallic cavities with high-Q resonance modes," (in English), *Nanotechnology*, vol. 26, no. 8, Feb 27 2015.
- [4] Y. Ye *et al.*, "Monolayer excitonic laser," (in English), *Nature Photonics*, vol. 9, no. 11, pp. 733-737, Nov 2015.
- [5] Y. H. Chou *et al.*, "Ultrastrong Mode Confinement in ZnO Surface Plasmon Nanolasers," (in English), *Acs Nano*, vol. 9, no. 4, pp. 3978-3983, Apr 2015.
- [6] S. A. Maier, *Plasmonics : fundamentals and applications*. New York: Springer, 2007, pp. xxiv, 223 p.
- [7] K. F. Renk, *Basics of Laser Physics*, 2nd Ed. 2017 ed. S.I. : Springer International PU, 2017.
- [8] O. Svelto, *Principles of lasers*. pp. x, 376 pages.
- [9] Y. Yu, T. Huang, Y. Wu, X. Ma, G. Yu, and J. Qi, "In-Vitro and In-Vivo Imaging of Prostate Tumor Using NaYF<sub>4</sub>: Yb, Er Up-Converting Nanoparticles," *Pathology & Oncology Research*, vol. 20, no. 2, pp. 335-341, 2014.
- [10] C. K. Siu *et al.*, "Lasing characteristics of single-crystalline CsPbCl<sub>3</sub> perovskite microcavities under multiphoton excitation," *Journal of Physics D: Applied Physics*, vol. 50, no. 22, p. 225101, 2017.
- [11] T. Wang *et al.*, "Influence of Plasmonic Effect on the Upconversion Emission Characteristics of NaYF<sub>4</sub> Hexagonal Microrods," *Inorganic Chemistry*, vol. 57, no. 14, pp. 8200-8204, 2018.
- [12] J. P. Guo and R. Adato, "Extended long range plasmon waves in finite thickness metal film and layered dielectric materials," (in English), *Optics Express*, vol. 14, no. 25, pp. 12409-12418, Dec 2006.
- [13] Q. Zhang *et al.*, "A room temperature low-threshold ultraviolet plasmonic nanolaser," (in English), *Nature Communications*, vol. 5, Sep 2014.
- [14] A. S. Barker and M. Ilegems, "Infrared Lattice-Vibrations and Free-Electron Dispersion in GaN," (in English), *Physical Review B*, vol. 7, no. 2, pp. 743-750, 1973.
- [15] I. H. Malitson, "Interspecimen Comparison of the Refractive Index of Fused Silica," *Journal of the Optical Society of America*, vol. 55, no. 10, pp. 1205-1209, 1965.
- [16] A. D. Rakic, "Algorithm for the Determination of Intrinsic Optical-Constants of Metal-Films - Application to Aluminum," (in English), *Applied Optics*, vol. 34, no. 22, pp. 4755-4767, Aug 1995.
- [17] Y. S. Bian and Q. H. Gong, "Metallic Nanowire-Loaded Plasmonic Slot Waveguide for Highly Confined Light Transport at Telecom Wavelength," (in English), *Ieee Journal of Quantum Electronics*, vol. 49, no. 10, pp. 870-876, Oct 2013.



- [18] Y. J. Lu *et al.*, "All-Color Plasmonic Nanolasers with Ultralow Thresholds: Autotuning Mechanism for Single-Mode Lasing," (in English), *Nano Letters*, vol. 14, no. 8, pp. 4381-4388, Aug 2014.
- [19] M. M. Jiang, H. Y. Chen, C. X. Shan, and D. Z. Shen, "Tunability of hybridized plasmonic waveguide mediated by surface plasmon polaritons," (in English), *Physical Chemistry Chemical Physics*, vol. 16, no. 30, pp. 16233-16240, 2014.
- [20] M. Sun, J. P. Tian, and L. Li, "Mode properties of a coaxial multi-layer hybrid surface plasmon waveguide," (in English), *Physica Status Solidi B-Basic Solid State Physics*, vol. 252, no. 8, pp. 1884-1889, Aug 2015.
- [21] C. L. Guo, K. J. Che, G. Q. Gu, G. X. Cai, Z. P. Cai, and H. Y. Xu, "Tailoring the plasmonic whispering gallery modes of a metal-coated resonator for potential application as a refractometric sensor," (in English), *Applied Optics*, vol. 54, no. 6, pp. 1250-1256, Feb 2015.
- [22] F. Lou, M. Yan, L. Thylen, M. Qiu, and L. Wosinski, "Whispering gallery mode nanodisk resonator based on layered metal-dielectric waveguide," (in English), *Optics Express*, vol. 22, no. 7, pp. 8490-8502, Apr 2014.
- [23] Q. F. Yao, Y. Z. Huang, L. X. Zou, X. M. Lv, J. D. Lin, and Y. D. Yang, "Analysis of Mode Coupling and Threshold Gain Control for Nanocircular Resonators Confined by Isolation and Metallic Layers," (in English), *Journal of Lightwave Technology*, vol. 31, no. 5, pp. 786-792, Mar 2013.
- [24] J. L. Quan *et al.*, "Study on growth techniques and macro defects of large-size Nd: YAG laser crystal," (in English), *Journal of Crystal Growth*, vol. 483, pp. 200-205, Feb 2018.
- [25] G. Monastyrskiy *et al.*, "Impact of heat dissipation on quantum cascade laser performance," (in English), *Journal of Applied Physics*, vol. 113, no. 13, Apr 2013.
- [26] Y. Yang, G. A. Turnbull, and I. D. W. Samuel, "Hybrid optoelectronics: A polymer laser pumped by a nitride light-emitting diode," (in English), *Applied Physics Letters*, vol. 92, no. 16, Apr 2008.
- [27] J. Andreasen and H. Cao, "Numerical study of amplified spontaneous emission and lasing in random media," (in English), *Physical Review A*, vol. 82, no. 6, Dec 2010.
- [28] H. M. Zhu *et al.*, "Lead halide perovskite nanowire lasers with low lasing thresholds and high quality factors," (in English), *Nature Materials*, vol. 14, no. 6, pp. 636-U115, Jun 2015.
- [29] D. J. Gargas *et al.*, "Whispering Gallery Mode Lasing from Zinc Oxide Hexagonal Nanodisks," (in English), *Acs Nano*, vol. 4, no. 6, pp. 3270-3276, Jun 2010.
- [30] Newport Corporation. (2018, 1 Aug). *Cornerstone™ 260 1/4m High Resolution Monochromators*. Available: <https://www.newport.com/f/cs260-high-resolution-monochromators>
- [31] HORIBA. (2018, 1 Aug). *Monochromator and Spectrographs: Design & Configuration*. Available: <https://www.horiba.com/en/en/technology/measurement-and-control-techniques/spectroscopy/monochromator-and-spectrographs/monochromator-spectrograph/>
- [32] F. M. Zehentbauer *et al.*, "Fluorescence spectroscopy of Rhodamine 6G: Concentration and solvent effects," (in English), *Spectrochimica Acta Part a-Molecular and Biomolecular Spectroscopy*, vol. 121, pp. 147-151, Mar 2014.



- [33] Sea Urchin Embryology. (2018, 3 Aug). *Introduction to Microscopy*. Available: <https://web.stanford.edu/group/Urchin/introm.htm>
- [34] Y. P. Fu *et al.*, "Nanowire Lasers of Formamidinium Lead Halide Perovskites and Their Stabilized Alloys with Improved Stability," (in English), *Nano Letters*, vol. 16, no. 2, pp. 1000-1008, Feb 2016.
- [35] W. Zhang *et al.*, "Controlling the Cavity Structures of Two-Photon-Pumped Perovskite Microlasers," (in English), *Advanced Materials*, vol. 28, no. 21, pp. 4040-4046, Jun 2016.
- [36] L. K. Van Vugt, S. Ruhle, and D. Vanmaekelbergh, "Phase-correlated nondirectional laser emission from the end facets of a ZnO nanowire," (in English), *Nano Letters*, vol. 6, no. 12, pp. 2707-2711, Dec 2006.
- [37] D. Rand, D. Miller, D. J. Ripin, and T. Y. Fan, "Cryogenic Yb<sup>3+</sup>-doped materials for pulsed solid-state laser applications," (in English), *Optical Materials Express*, vol. 1, no. 3, pp. 434-450, Jul 2011.
- [38] J. A. N. Fisher, K. Susumu, M. J. Therien, and A. G. Yodh, "One- and two-photon absorption of highly conjugated multiporphyrin systems in the two-photon Soret transition region," (in English), *Journal of Chemical Physics*, vol. 130, no. 13, Apr 2009.
- [39] B. Gu, X. Q. Huang, S. Q. Tan, M. Wang, and W. Ji, "Z-scan analytical theories for characterizing multiphoton absorbers," *Appl. Phys. B*, vol. 95, no. 2, pp. 375-381, 2009.
- [40] M. Liu, H. S. Quah, S. Wen, Y. Li, J. J. Vittal, and W. Ji, "Multiphoton Absorption and Two-Photon-Pumped Random Lasing in Crystallites of a Coordination Polymer," *The Journal of Physical Chemistry C*, vol. 122, no. 1, pp. 777-781, 2018.
- [41] D. S. Corrêa, L. De Boni, L. Misoguti, I. Cohanoschi, F. E. Hernandez, and C. R. Mendonça, "Z-scan theoretical analysis for three-, four- and five-photon absorption," *Optics Communications*, vol. 277, no. 2, pp. 440-445, Sep 2007.
- [42] M. G. Vivas, E. Piovesan, D. L. Silva, T. M. Cooper, L. De Boni, and C. R. Mendonça, "Broadband three-photon absorption spectra of platinum acetylide complexes," *Optical Materials Express*, vol. 1, no. 4, pp. 700-710, 2011.
- [43] S. Faruk, S. Suhaidi, L. Hong Ngee, and M. Abubakar Ohinoyi, "Advancement on Lead-Free Organic-Inorganic Halide Perovskite Solar Cells: A Review," *Materials*, vol. 11, no. 6, p. 1008, 2018.
- [44] T. M. Brenner, D. A. Egger, L. Kronik, G. Hodes, and D. Cahen, "Hybrid organic-inorganic perovskites: low-cost semiconductors with intriguing charge-transport properties," *Nature Reviews Materials*, Review Article vol. 1, p. 15007, 2016.
- [45] Y. Zhao and K. Zhu, "Organic-inorganic hybrid lead halide perovskites for optoelectronic and electronic applications," *Chem. Soc. Rev.*, vol. 45, no. 3, pp. 655-689, 2016.
- [46] G. E. Eperon *et al.*, "Inorganic caesium lead iodide perovskite solar cells," *J. Mater. Chem. A*, vol. 3, no. 39, pp. 19688-19695, 2015.
- [47] B. R. Sutherland and E. H. Sargent, "Perovskite photonic sources," *Nature Photonics*, Review Article vol. 10, p. 295, 2016.
- [48] G. Xing *et al.*, "Low-temperature solution-processed wavelength-tunable perovskites for lasing," *Nature Materials*, vol. 13, p. 476, 2014.



- [49] Q. Zhang, S. T. Ha, X. Liu, T. C. Sum, and Q. Xiong, "Room-Temperature Near-Infrared High-Q Perovskite Whispering-Gallery Planar Nanolasers," *Nano Letters*, vol. 14, no. 10, pp. 5995-6001, 2014.
- [50] H.-S. Kim, J.-Y. Seo, and N.-G. Park, "Material and Device Stability in Perovskite Solar Cells," *ChemSusChem*, vol. 9, no. 18, pp. 2528-2540, 2016.
- [51] S. D. Stranks and H. J. Snaith, "Metal-halide perovskites for photovoltaic and light-emitting devices," *Nature Nanotechnology*, Review Article vol. 10, p. 391, 2015.
- [52] S. W. Eaton *et al.*, "Lasing in robust cesium lead halide perovskite nanowires," *Proceedings of the National Academy of Sciences*, 10.1073/pnas.1600789113 vol. 113, no. 8, p. 1993, 2016.
- [53] Q. Zhang, R. Su, X. Liu, J. Xing, T. C. Sum, and Q. Xiong, "High-Quality Whispering-Gallery-Mode Lasing from Cesium Lead Halide Perovskite Nanoplatelets," *Advanced Functional Materials*, vol. 26, no. 34, pp. 6238-6245, 2016.
- [54] K. Park *et al.*, "Light-Matter Interactions in Cesium Lead Halide Perovskite Nanowire Lasers," *The Journal of Physical Chemistry Letters*, vol. 7, no. 18, pp. 3703-3710, 2016.
- [55] Y. Fu *et al.*, "Broad Wavelength Tunable Robust Lasing from Single-Crystal Nanowires of Cesium Lead Halide Perovskites (CsPbX<sub>3</sub>, X = Cl, Br, I)," *ACS Nano*, vol. 10, no. 8, pp. 7963-7972, 2016.
- [56] S. Yakunin *et al.*, "Low-threshold amplified spontaneous emission and lasing from colloidal nanocrystals of caesium lead halide perovskites," *Nature Communications*, Article vol. 6, p. 8056, 2015.
- [57] Y. Wang, X. Li, X. Zhao, L. Xiao, H. Zeng, and H. Sun, "Nonlinear Absorption and Low-Threshold Multiphoton Pumped Stimulated Emission from All-Inorganic Perovskite Nanocrystals," *Nano Letters*, vol. 16, no. 1, pp. 448-453, 2016.
- [58] Y. Xu *et al.*, "Two-Photon-Pumped Perovskite Semiconductor Nanocrystal Lasers," *Journal of the American Chemical Society*, vol. 138, no. 11, pp. 3761-3768, 2016.
- [59] T.-C. Lin, G. S. He, Q. Zheng, and P. N. Prasad, "Degenerate two-/three-photon absorption and optical power-limiting properties in femtosecond regime of a multi-branched chromophore," *Journal of Materials Chemistry*, vol. 16, no. 25, pp. 2490-2498, 2006.
- [60] B. S. Kalanoor *et al.*, "Third-Order Optical Nonlinearities in Organometallic Methylammonium Lead Iodide Perovskite Thin Films," *ACS Photonics*, vol. 3, no. 3, pp. 361-370, 2016.
- [61] J. C. Johnson, H. Yan, P. Yang, and R. J. Saykally, "Optical Cavity Effects in ZnO Nanowire Lasers and Waveguides," *The Journal of Physical Chemistry B*, vol. 107, no. 34, pp. 8816-8828, 2003.
- [62] M. A. Ghebouli, B. Ghebouli, and M. Fatmi, "First-principles calculations on structural, elastic, electronic, optical and thermal properties of CsPbCl<sub>3</sub> perovskite," *Physica B: Condensed Matter*, vol. 406, no. 9, pp. 1837-1843, 2011.
- [63] G. Shangjr and S. Chih-Kang, "Semiconductor plasmonic nanolasers: current status and perspectives," *Reports on Progress in Physics*, vol. 79, no. 8, p. 086501, 2016.
- [64] D. Wei *et al.*, "Upconversion in NaYF<sub>4</sub>:Yb, Er nanoparticles amplified by metal nanostructures," *Nanotechnology*, vol. 22, no. 32, p. 325604, 2011.





- [65] S. Han, R. Deng, X. Xie, and X. Liu, "Enhancing Luminescence in Lanthanide-Doped Upconversion Nanoparticles," *Angewandte Chemie International Edition*, vol. 53, no. 44, pp. 11702-11715, 2014.
- [66] R. Deng, F. Qin, R. Chen, W. Huang, M. Hong, and X. Liu, "Temporal full-colour tuning through non-steady-state upconversion," *Nature Nanotechnology*, vol. 10, p. 237, 2015.
- [67] Q. Zhan *et al.*, "Using 915 nm Laser Excited Tm<sup>3+</sup>/Er<sup>3+</sup>/Ho<sup>3+</sup>-Doped NaYbF<sub>4</sub> Upconversion Nanoparticles for in Vitro and Deeper in Vivo Bioimaging without Overheating Irradiation," *ACS Nano*, vol. 5, no. 5, pp. 3744-3757, 2011.
- [68] J. Pichaandi, J.-C. Boyer, K. R. Delaney, and F. C. J. M. van Veggel, "Two-Photon Upconversion Laser (Scanning and Wide-Field) Microscopy Using Ln<sup>3+</sup>-Doped NaYF<sub>4</sub> Upconverting Nanocrystals: A Critical Evaluation of their Performance and Potential in Bioimaging," *The Journal of Physical Chemistry C*, vol. 115, no. 39, pp. 19054-19064, 2011.
- [69] Y. Zhu *et al.*, "Fine-tuning of multiple upconversion emissions by controlling the crystal phase and morphology between GdF<sub>3</sub>:Yb<sup>3+</sup>,Tm<sup>3+</sup> and GdOF:Yb<sup>3+</sup>,Tm<sup>3+</sup> nanocrystals," *RSC Advances*, vol. 7, no. 5, pp. 2426-2434, 2017.
- [70] W. Park, D. Lu, and S. Ahn, "Plasmon enhancement of luminescence upconversion," *Chemical Society Reviews*, vol. 44, no. 10, pp. 2940-2962, 2015.
- [71] Y. Wang, Z. Yang, Y. Ma, Z. Chai, J. Qiu, and Z. Song, "Upconversion emission enhancement mechanisms of Nd<sup>3+</sup>-sensitized NaYF<sub>4</sub>:Yb<sup>3+</sup>,Er<sup>3+</sup> nanoparticles using tunable plasmonic Au films: plasmonic-induced excitation, radiative decay rate and energy-transfer enhancement," *Journal of Materials Chemistry C*, vol. 5, no. 33, pp. 8535-8544, 2017.
- [72] Y. Xue *et al.*, "Tuning Plasmonic Enhancement of Single Nanocrystal Upconversion Luminescence by Varying Gold Nanorod Diameter," *Small*, vol. 13, no. 36, p. 1701155, 2017.
- [73] Z. Yin *et al.*, "Plasmon-Enhanced Upconversion Luminescence on Vertically Aligned Gold Nanorod Monolayer Supercrystals," *ACS Applied Materials & Interfaces*, vol. 8, no. 18, pp. 11667-11674, 2016.
- [74] A. El Halawany *et al.*, "Enhanced UV upconversion emission using plasmonic nanocavities," *Optics Express*, vol. 24, no. 13, pp. 13999-14009, 2016.
- [75] Q. Tian *et al.*, "Efficient UV-Vis-NIR Responsive Upconversion and Plasmonic-Enhanced Photocatalyst Based on Lanthanide-Doped NaYF<sub>4</sub>/SnO<sub>2</sub>/Ag," *ACS Sustainable Chemistry & Engineering*, vol. 5, no. 11, pp. 10889-10899, 2017.
- [76] M. Ambati, S. H. Nam, E. Ulin-Avila, D. A. Genov, G. Bartal, and X. Zhang, "Observation of Stimulated Emission of Surface Plasmon Polaritons," *Nano Letters*, vol. 8, no. 11, pp. 3998-4001, 2008.
- [77] S. Li *et al.*, "Surface Plasmon Resonance Enhanced Spontaneous Upconversion and Stimulated Emissions in Glass Ceramics Containing BaLaF Nanocrystals," *Advances in Condensed Matter Physics*, vol. 2017, 2017.
- [78] C. Shi, S. Soltani, and A. M. Armani, "Gold Nanorod Plasmonic Upconversion Microlaser," *Nano Letters*, vol. 13, no. 12, pp. 5827-5831, 2013.
- [79] R. Bedford and M. Fallahi, "Analysis of high-reflectivity metal-dielectric mirrors for edge-emitting lasers," *Optics Letters*, vol. 29, no. 9, pp. 1010-1012, 2004.



- [80] B. Chen, T. Sun, X. Qiao, X. Fan, and F. Wang, "Directional Light Emission in a Single NaYF<sub>4</sub> Microcrystal via Photon Upconversion," *Advanced Optical Materials*, vol. 3, no. 11, pp. 1577-1581, 2015.
- [81] M. J. Dodge, "Refractive properties of magnesium fluoride," *Applied Optics*, vol. 23, no. 12, pp. 1980-1985, 1984.
- [82] P. B. Johnson and R. W. Christy, "Optical Constants of the Noble Metals," *Physical Review B*, vol. 6, no. 12, pp. 4370-4379, 1972.
- [83] T. Wang, H. Yu, C. K. Siu, J. Qiu, X. Xu, and S. F. Yu, "White-Light Whispering-Gallery-Mode Lasing from Lanthanide-Doped Upconversion NaYF<sub>4</sub> Hexagonal Microrods," *ACS Photonics*, vol. 4, no. 6, pp. 1539-1543, 2017.